MASTERARBEIT | MASTER'S THESIS

Titel | Title

Modelling of Atmospheric Transport of Microplastics

verfasst von | submitted by

Alina Reininger BSc MSc

angestrebter akademischer Grad | in partial fulfilment of the requirements for the degree of

Master of Science (MSc)

Wien | Vienna, 2024

Studienkennzahl lt. Studienblatt | Degree programme code as it appears on the student record sheet:	UA 066 299
Studienrichtung lt. Studienblatt | Degree programme as it appears on the student record sheet:	Masterstudium Environmental Science
Betreut von | Supervisor:	Univ.-Prof. Mag. Dr. Andreas Stohl

Acknowledgements

First, I would like to thank Prof. Andreas Stohl for giving me the opportunity to work in his research group and for supervising this second Master's thesis of mine. Thank you for your constant support and advice.

Thank you very much, Daria Tatsii, for giving me an introduction to FLEXPART and for helping me improve my Python skills. Thank you for supervising my work in general and for taking the time to meet to answer all of my questions, even though you were busy yourself, which I cannot appreciate enough.

I also want to thank the members of the Department of Meteorology and Geophysics at the University of Vienna for helping me with my work, especially when I encountered technical problems.

I want to thank my friends, family, and especially my parents for supporting me through my studies and while writing two Master's theses. Thank you for everything you did for me.

Abstract

Microplastics have become a key environmental challenge, and the atmosphere plays a major role in their distribution. Atmospheric transport depends on the settling behavior of particles, which in turn depends strongly on their shape and size. Atmospheric transport models often consider particles as perfect spheres. Due to their often complex shapes (fibers, films, fragments, etc.), however, airborne microplastics can experience lower settling velocities than volume-equivalent spheres, leading to longer atmospheric transport and the deposition in remote, thinly populated areas. The atmospheric transport of microplastic fibers has been investigated; nevertheless, information on flat, film-like particles is still lacking. Here, the atmospheric transport distances, residence times, and deposition patterns of microplastic films, particularly glitter particles and thin square films, and their volume-equivalent spheres are presented, resulting from global atmospheric transport simulations using FLEXPART with the scheme of Bagheri and Bonadonna [2016], constrained by laboratory experiments done by Reininger [2024]. The results show that glitter particles are not transported substantially further than spheres of the same volume; the mean atmospheric transport distances of glitters are around 21 % greater than those for spheres at the maximum. This is not the case for thin, square films, which are much thinner than commercially available glitter particles, which travel up to 123 % further than spheres. Glitter particles may be deposited up to 53 km away from their source and remain airborne for more than 4 h. Square films can even travel up to 245 km in the atmosphere, with average residence times of nearly 14 h. These results indicate that glitter, when released into the air, can be transported on an urban and regional scale. This is particularly relevant for glitter released during parades or carnivals in cities, since pollution may spread to areas surrounding the city, including agricultural land or conservation areas. Furthermore, these particles might fragment and be transported even further, even across country boundaries. In this context, further regulations and bans for the use of plastics and glitters in particular are recommended. For now, awareness must be raised in order for consumers to change their habits regarding (micro)plastic, for example, a transition to biodegradable alternatives to glitter.

Kurzfassung

Mikroplastik ist zu einer entscheidenden Umweltherausforderung geworden. Die Atmosphäre stellt dabei ein wichtiges Transportmedium für Mikroplastik dar. Der atmosphärische Transport hängt stark von der Sedimentation der Teilchen ab, welche wiederum von Größe und Form der Teilchen bestimmt wird. In atmosphärischen Transportmodellen werden Partikel jedoch oft als sphärisch beschrieben. Aufgrund ihrer oft komplexen Formen (Fasern, Folien, Fragmente usw.) weisen Mikroplastikpartikel aber geringere Fallgeschwindigkeiten als sphärische Partikel mit gleichem Volumen auf. Dies führt zu längerem atmosphärischem Transport und der Ablagerung in selbst abgelegenen und dünn besiedelten Gebieten. Der atmosphärische Transport von Mikroplastik-Fasern wurde bereits untersucht; dies ist jedoch nicht der Fall für flache, folienartige Partikel. In dieser Arbeit werden daher die aus globalen Simulationen mit FLEXPART resultierenden Transportdistanzen, Aufenthaltszeiten und die Sedimentation von atmosphärischen Mikroplastikfolien, insbesondere Glitzerpartikeln und dünnen Folien, und sphärischen Partikeln mit gleichem Volumen präsentiert. Die Ergebnisse zeigen, dass Glitzerpartikel nicht wesentlich weiter transportiert werden als sphärische Partikel; die durchschnittlichen atmosphärischen Transportdistanzen unterscheiden sich um maximal 21 %. Dies gilt jedoch nicht für quadratische Folien, welche viel dünner sind als kommerziell verfügbarer Glitzer; sie werden bis zu 123 % weiter transportiert als sphärische Partikel. Glitzerpartikel können bis zu 53 km von der Quelle entfernt abgelagert werden und länger als 4 Stunden in der Luft verbleiben. Quadratische, dünne Folien können sogar bis zu 245 km transportiert werden, wobei sie durchschnittlich bis zu knapp 14 h in der Luft bleiben. Diese Ergebnisse deuten darauf hin, dass Glitzer, wenn dieser in der Luft freigesetzt wird, auf städtischer und regionaler Ebene transportiert werden kann. Dies gilt insbesondere für Glitzer, der während Paraden oder Karnevals in Städten freigesetzt wird und die Umgebung der Stadt, einschließlich landwirtschaftlicher Flächen oder Naturschutzgebiete, verschmutzen kann. Darüber hinaus könnten diese Partikel zerfallen und sogar über Landesgrenzen hinweg und noch weiter transportiert werden. In diesem Zusammenhang werden weitere Vorschriften und Verbote für die Verwendung von Kunststoffen und Glitzer benötigt. Einstweilen muss das Bewusstsein erhöht werden, damit Verbraucher ihre Gewohnheiten in Bezug auf (Mikro)Plastik ändern, und zum Beispiel zu biologisch abbaubaren Alternativen wechseln.

Contents

List of Tables

List of Figures

1. Introduction

1.1. Microplastics

Microplastics are small-sized synthetic polymers that are hazardous to the environment and a serious global pollutant problem. The terminology is still ambiguous, as no internationally agreed definition of the size of microplastics exists [Hartmann et al., 2019, Petersen and Hubbart, 2021]. The term "all plastic particles < 5 mm in diameter" is most commonly used to define microplastics [Hartmann et al., 2019], however Hartmann et al. [2019] propose the following categories for plastic litter as a pragmatic compromise: nanoplastics: 1 to $<$ 1000 nm; microplastics: 1 to $<$ 1000 µm; mesoplastics: 1 to $<$ 10 mm; macroplastics: 1 cm and larger.

Besides size, plastics can be grouped according to their shapes. Hartmann et al. [2019] suggest distinguishing between spheres (microplastic particles with every point on their surface having equivalent distance to the center), spheroids (approximate spheres), cylindrical pellets, irregular particles, films (planar objects that are much smaller in one dimension than in the other two), and fibers (thread-like structures being significantly longer in one than wide in two dimensions).

According to Hartmann et al. [2019], some disagreement exists on which polymers can be considered plastics. The authors suggest that polymers that are petroleum-based (polyethylene (PE), polypropylene (PP), polyvinyl chloride (PVC), polystyrene (PS), polyethylene terephthalate (PET), biobased (bio-PET, bio-PE), and biodegradable, as well as inorganic/hybrid polymers, should be included in the definition of plastic debris. Furthermore, they recommend including composites, copolymers, and surface coatings containing synthetic polymers.

In terms of sources, microplastics can be divided into primary and secondary microplastics [Auta et al., 2017, Xiang. et al., 2022]. Primary microplastics are specifically produced for a number of products, including personal care products, cosmetics, cleaning agents, and craft materials [Auta et al., 2017, Xiang. et al., 2022, Yurtsever, 2019b]. Secondary microplastics stem from larger plastics that are broken up and degraded due to UV radiation, chemical degradation (e.g., by reaction with ozone), physical abrasion, wind, temperature, wave action, anthropogenic effects, or microbial-mediated processes [Auta et al., 2017, Xiang. et al., 2022, Yurtsever, 2019b, Kim et al., 2022, Zhang et al., 2022].

Microplastics can cause mechanical injury, low growth rate, morbidity, mortality, oxidative stress, cellular and DNA damage, and inflammatory and immunological reactions in organisms [Petersen and Hubbart, 2021, Xiang. et al., 2022]. Furthermore, microplastic particles have the potential to enter the food chain and may compromise human food security [Xiang. et al., 2022, Yurtsever, 2019b]. Microplastics may also act as vectors for pollutants; they are capable of adsorbing organic pollutants and metals [Yurtsever, 2019b, Petersen and Hubbart, 2021, Brennecke et al., 2016]. In combination with microplastics' ingredients themselves, the pollutants adsorbed pose a novel threat to organisms that are exposed to them [Yurtsever, 2019b, Brennecke et al.,

2016]. Therefore, it is essential to establish a good understanding of the sources, sinks, and pathways of these particles in the environment. The atmosphere, for example, acts as a major transport mechanism for microplastics [Petersen and Hubbart, 2021], carrying them to even remote locations, as shown by Evangeliou et al. [2020] and Tatsii et al. [2024]. The lithosphere, on the other hand, acts mainly as a sink for microplastics since they break down slowly in soils and successively build up in these environments [Petersen and Hubbart, 2021, Bläsing and Amelung, 2018]. Freshwater conveyance systems eventually carry microplastics into the oceans, where particles less dense than seawater concentrate on shorelines and the water surface, and denser particles sink to deeper water or the seabed [Petersen and Hubbart, 2021, Duis and Coors, 2016, Cole et al., 2011].

1.1.1. Glitter

One type of primary microplastic that has mostly been overlooked so far is glitter. Glitter refers to small, flat, and reflective particles that are usually made of metallized PET [Yurtsever, 2019b,a]. Commercially sold glitter ranges between 50 µm and 6 mm, with 200 µm being the most popular size [Yurtsever, 2019a, Blackledge and Jones Jr, 2007]. Glitter is often made of meallized (aluminum, titanium, iron, or bismuth) PET [Yurtsever, 2019a], where polymer surrounds a metallized film [Tagg and Ivar do Sul, 2019], with densities between $1.32\,\mathrm{g/cm^3}$ and $1.41\,\mathrm{g/cm^3}$ [Tagg and Ivar do Sul, 2019, Yurtsever, 2019a]. The number and thickness of these layers are unique for each particle [Tagg and Ivar do Sul, 2019]. Glitter can also be made of acrylic, Poly(methyl methacrylate) (PMMA), Polyvinyl Chloride (PVC), plastic epoxy resin mixture, or melamine and phenolic resin mixture [Yurtsever, 2019b]. Some glitter products may contain dyes or pigments, while others don't [Blackledge and Jones Jr, 2007]. As an alternative, renewable plant-based raw materials such as soluble seaweed, regenerated cellulose, and glycerin are also produced [Yurtsever, 2019b].

Glitters are mostly of variant colors and are often cut into hexagonal, though non-homogeneous, pieces during manufacturing [Yurtsever, 2019a, Blackledge and Jones Jr, 2007]. Square or rectangular shapes are also quite common [Blackledge and Jones Jr, 2007]. Glitter can also be obtained in specialized shapes such as circles, stars, and crescent moons, according to Blackledge and Jones Jr [2007]. The authors state that these particles are usually larger since it is intended that a viewer can see and recognize these shapes. Some companies offer glitters that fluoresce under ultraviolet light or have holographic properties [Blackledge and Jones Jr, 2007], containing fine patterns on the particles [Weaver].

The use of glitter and its way into the environment

Glitter is an undeniable element of pop culture. It appears within a wide range of products, including nail polish, cosmetics, textiles, body paint, or decorations [Tagg and Ivar do Sul, 2019, Yurtsever, 2019a,b]. Furthermore, it is used for crafting and artwork, where it is sold loose, in pencil sticks, or in glues [Blackledge and Jones Jr, 2007], to be added to glass decoration, gift cards, or tumblers, for example. Glitter is extensively used for entertainment events, carnivals, and shows around the globe [Yurtsever, 2019a], where it is applied to skin, hair, nails, or clothes. In 2011, for instance, almost 70 kg have been used in the Toronto Santa Claus Parade [Yurtsever,

2019b]. More than 4.5 million kg of glitter were purchased between 1989 and 2009 in the US [Yurtsever, 2019b]. This corresponds to roughly 100 Trillion glitter particles of the most commonly sold size (200 µm). Glitter, therefore, has the potential to contaminate virtually everywhere, spilling on the ground and entering the sewage system through washing activities [Tagg and Ivar do Sul, 2019, Yurtsever, 2019a]. Tagg and Ivar do Sul [2019] and Yurtsever [2019b] for example suggest a direct pathway of glitters used in cosmetics and body paint to wastewater treatment plants and, therefore, a release into natural aquatic systems with treated effluent water or sewage sludge or during overflow events. Tagg and Ivar do Sul [2019] state that, even if not used regularly, glitter used in body paints can constitute a considerable source of microplastics for aquatic systems. Glitter-based nail polish is usually removed with cotton wool soaked in acetone, which makes landfills a potential temporary sink [Tagg and Ivar do Sul, 2019] but also a potential source of emissions to the atmosphere. These nail polish can be applied multiple times per week over extended periods [Tagg and Ivar do Sul, 2019], and could therefore lead to considerable amounts of released microplastics. Glitter particles are also prone to shedding away from where (or whom) they are attached to [Yurtsever, 2019b], possibly being released into the air. However, more research is required on the possible sources and pathways of glitter particles in the environment.

Glitter in scientific literature

Microbeads, manufactured small plastic spheres, deliberately included in personal care products, have been banned in several countries worldwide due to increasing public pressure supported by scientific evidence of microplastic pollution, including the US, UK, Canada, and the EU, [Guerranti et al., 2019, Regulation 2023/2055.]. However, glitter particles have been widely overlooked by the field of environmental science [Tagg and Ivar do Sul, 2019]. Yurtsever [2019a] argue that glitters as a source of microplastics have yet to be understood since in some studies, glitters that were found are referred to as microplastic film, fragment, shiny film, or hexagonal film. A comprehensive IUCN (International Union for the Conservation of Nature) report on the current state of primary microplastics entering the marine environment discusses multiple microplastic sources, including microbeads from cosmetics, but omits glitters [Tagg and Ivar do Sul, 2019, Boucher and Friot, 2017]. However, a number of studies detected glitter particles in the environment: Lusher et al. [2017] found PET glitters in 5 out of 10 Norwegian domestic wastewater treatment plants. The authors found that PET glitters account for 1.7% in weight of all plastics in their samples. Hurley et al. [2018] noted the existence of glitter in riverbed sediments, and Raju et al. [2020] found that glitter can account for up to 24% of microplastics in wastewater treatment plants. Abbasi et al. [2017] detected silver/gray, orange, and red hexagonal glitter particles, referred to as 'different color of shiny film (probably create primary resource)' in street dust in Bushehr city, Iran.

One reason glitter has been mainly overlooked so far is the fact that glitter can avoid detection when microplastics are extracted from water, soil, sediment, or sludge samples [Yurtsever, 2019a]. The addition of an acidic solution or heating during extraction processes may dissolve the coating on the surface of glitters, making them transparent and colorless [Yurtsever, 2019a]. Glitters that possess a high density (PET, PVC) are more likely to settle at the bottom during density separation when low-density solutions are used [Yurtsever, 2019a, Sun et al., 2019]. This might

be the reason for the low number of glitters observed in aquatic environments, since most samples are taken from the water surface [Yurtsever, 2019a].

Adverse effects of glitter

Glitters, in particular, can pose a threat to organisms. Due to their small size, they can easily access a wide range of aquatic organisms and become part of the food chain [Yurtsever, 2019a, Petersen and Hubbart, 2021]. Machado et al. [2023] found that glitter in high concentrations caused biovolume increment and growth rate reduction in cyanobacterial strains. The authors conclude that glitter particles may negatively influence susceptible organisms in aquatic ecosystems. The pointy-sharp edges of glitters are especially hazardous for biota [Yurtsever, 2019a]. Provenza et al. [2022] found that the digestive tract of Mediterranean mussels retains small glitter particles in particular, and noted increase in antioxidant defense that was induced by these glitter particles. Yurtsever [2019a] found that glitters treated with an acidic solution (HCl, HNO_3, H_2SO_4) tended to dissolve their metal and polymer color-coating, whereas the PET-film remained intact at low pH. The authors concluded that, if swallowed, the metals on the glitters could be dissolved in the gastric acid. However, when used in makeup products, glitter may also be hazardous for humans. When used in eye makeup, glitter may cause corneal irritation and eye redness when entering the eye and the tear film [Becker et al., 2014]. If glitter particles get between the contact lens and the corneal surface, they could scratch the cornea and lead to corneal infection [Becker et al., 2014].

1.2. Microplastics in the Atmosphere

Several studies have found giant (>75 µm in diameter) wind-blown mineral dust particles at large distances from their sources [Van Der Does et al., 2018, Varga et al., 2021, Middleton et al., 2001]. Microplastics too can stay airborne for extended periods and have been detected in the atmospheres of urban, suburban, and remote locations, suggesting long-distance atmospheric transport for microplastics. Registered atmospheric microplastic concentrations varied: Liu et al. [2019] reported 1.37 particles/m^3/day for the western Pacific Ocean. Dris et al. [2016] found an average atmospheric fiber fallout of 110 ± 96 particles/m^2/day in a dense urban environment and 53 ± 38 particles/m^2/day in a less dense sub-urban environment. They estimate that at least 29 % of these fibers contain petrochemicals. According to the authors, these microplastic fibers stem from clothes and houses, the degradation of macroplastics, landfills, or waste incineration. Allen et al. [2020] reported an average atmospheric microplastics deposition of 365 particles/m^2/day in a remote, pristine mountain catchment of the French Pyrenees Mountains. Bergmann et al. [2019] also highlight that atmospheric transport and deposition can be notable pathways for microplastics. The authors analyzed snow samples from ice floes in Fram Strait and compared them to snow samples from remote (Swiss Alps) and populated (Bremen, Bavaria) European sites. They found that the concentration of microplastics ranges from 0 to $14.4 \cdot 10^3$ particles per liter in Arctic snow, which is still substantial compared to $0.19 \cdot 10^3$ to $154 \cdot 10^3$ particles per liter in European snow.

The sizes of atmospheric microplastics found range from 11 µm [Bergmann et al., 2019] to 5000 µm [Dris et al., 2016]. Fibers were to most registered shapes by Liu et al. [2019], while Allen et al.

[2020] found fragments as the most prevalent shape. These differences could be explained by different sources [Alfonso et al., 2021]. A comparison done by Alfonso et al. [2021] of experimental studies on atmospheric microplastics results in the following most frequent polymer types: PP, PS, and PE.

Using global atmospheric transport simulations, Evangeliou et al. [2020] showed that microplastics produced by road traffic (i.e., tire wear particles and brake wear particles) are efficiently transported to even remote locations on Earth. They calculated that approximately 34% (100 kt/yr) of these particles are deposited in the World Ocean via atmospheric transport, which is comparable to estimated direct and riverine transport (64 kt/yr). Furthermore, the authors suggest that the Arctic is a particularly sensitive receptor region, since the light-absorbing properties of these particles may accelerate the warming and melting of the cryosphere. Tatsii et al. [2024] demonstrate in their simulations that microplastic fibers can be transported in the atmosphere to almost any point on the globe. The authors also highlight the impact of the particle's shape on its atmospheric transport: fibers settle up to 76 % slower than spheres of the same volume. According to them, fibers with lengths up to 100 µm have the potential to reach the stratosphere. There, these particles could be degraded by UV radiation, releasing chlorine and bromine and damaging the stratospheric ozone layer.

Rain and snow are considered important deposition mechanisms of atmospheric microplastics [Brahney et al., 2020, Allen et al., 2020, Liu et al., 2019, Alfonso et al., 2021], while several mechanisms have been suggested that can facilitate long-range transport of giant particles, such as strong winds, turbulence, electrical forces, thunderstorms, tropical cyclones, the particle's shape, and a combination of several of these factors. Brahney et al. [2020] report differences for the dry and wet deposition of atmospheric microplastics in protected areas of the US: Short distance sources such as urban centers and resuspension from soils or water dominated for wet deposition events, while plastics deposited under dry conditions were smaller in size, with probable long-range or even global transport. Moreover, Liu et al. [2019] registered differences between day and night in the open ocean deposition of atmospheric microplastics from the continent. On average, the amount of suspended atmospheric microplastics collected during the day was twice the amount collected at night. The authors attribute this difference to changes in relative humidity conditions. Evangeliou et al. [2020] state that climatic events such as the North Atlantic Oscillation can enhance pollution transportation to remote locations such as the Arctic, mainly in winter and spring. According to them, strong winds may remobilize deposited microplastics, elevating their transport. Strong winds may also cause fast horizontal transport and therefore may greatly enhance the particles' transport distances [Van Der Does et al., 2018, Garcia-Carreras et al., 2015]. Turbulence may keep individual large particles aloft for a longer time [Van Der Does et al., 2018, Garcia-Carreras et al., 2015]. Electrical forces might counteract gravitational settling of coarse particles, keeping them aloft for longer [Van Der Does et al., 2018, Renard et al., 2018]. Thunderstorms or tropical cyclones may lift particles up to great heights, increasing their horizontal transport distance if the particles can leave the storm through the anvil or upper-level outflow region without being rained out [Van Der Does et al., 2018]. Last, the particle's shape can increase its drag force and therefore reduce its terminal settling velocity [Hinds and Zhu, 2022, Brasseur and Jacob, 2017, Tatsii et al., 2024].

1.2.1. Gravitational Settling of Microplastics

The transport distance of an airborne particle is influenced by its terminal settling velocity v_t [Hinds and Zhu, 2022, Saxby et al., 2018]. A particle reaches its terminal settling velocity when the force of gravity is balanced by the drag force of the air on the particle so that it no longer accelerates [Hinds and Zhu, 2022, Saxby et al., 2018, Brasseur and Jacob, 2017]. The terminal settling velocity is defined by Newton's drag force with an additional parameter, the Cunningham slip-correction factor C_c:

$$v_t = \left[\frac{4\rho_p g C_c D_p}{3 C_D \rho_a}\right]^{1/2} \tag{1.1}$$

[Hinds and Zhu, 2022, Brasseur and Jacob, 2017]. The Cunningham slip-correction factor reduces the drag force for very small particles and, therefore, increases their terminal settling velocities [Hinds and Zhu, 2022]. It is important for particles smaller than 1 µm [Hinds and Zhu, 2022]. ρ_p is the mass density of the particle, D_p is the particle diameter, g is the gravitational acceleration, and ρ_a is the air density. C_D is the coefficient of drag, which depends on the particle's shape and its Reynolds number Re:

$$Re = \frac{\rho_a v_t D_p}{\eta} \tag{1.2}$$

[Hinds and Zhu, 2022, Brasseur and Jacob, 2017, Seinfeld and Pandis, 2016], with η being the dynamic viscosity. Therefore, the terminal settling velocity depends on the particle's size, shape, and density, as well as the atmosphere's density and viscosity.

Drag coefficient of spherical particles

For spheres with $1000 \leq Re < 3 \cdot 10^5$, the drag coefficient is almost constant [Hinds and Zhu, 2022, Bagheri and Bonadonna, 2016]. For very small Reynolds numbers, Hinds and Zhu [2022] suggest the following equations for the drag coefficient of spheres:

$$C_D = \frac{24}{Re} \tag{1.3}$$

For Reynolds numbers that are between 0.1 and 500, Brasseur and Jacob [2017] provide the following equations:

$$C_D = \frac{24}{Re}\left[1 + \frac{3}{16}Re + \frac{9}{160}Re^2 \ln(2Re)\right] \qquad \text{for} \quad 0.1 < Re < 2 \tag{1.4}$$

$$C_D = \frac{24}{Re}\left[1 + 0.15 Re^{0.687}\right] \qquad \text{for} \quad 2 < Re < 500 \tag{1.5}$$

Clift and Gauvin [1971] proposed one of the most accurate expressions for the drag coefficient of spheres with $Re < 3 \cdot 10^5$ [Bagheri and Bonadonna, 2016, Tatsii et al., 2024]:

$$C_D = \frac{24}{Re}(1 + 0.15 Re^{0.687}) + \frac{0.42}{1 + \frac{42500}{Re^{1.16}}} \qquad \text{for} \quad Re < 3 \cdot 10^5 \tag{1.6}$$

Drag coefficient of non-spherical particles

For describing the drag coefficient of non-spherical particles as a function of shape, no general solution exists, but several empirical and semiempirical parametrization schemes have been developed [Bagheri and Bonadonna, 2016]. The empirical model of Bagheri and Bonadonna [2016] provides excellent results for predicting the drag coefficient of freely falling non-spherical, regular, and irregular particles in liquids or gases for $Re < 3 \cdot 10^5$ [Saxby et al., 2018, Coyle et al., 2023]. Two novel shape descriptors are considered by the scheme: The Stokes and Newton shape descriptors, F_S and F_N respectively, which are based on particle flatness fl, elongation el, and the diameter of a sphere which has the same volume as the nonspherical particle, called the volume-equivalent diameter d_{eq}. fl is defined as the ratio of the particle's shortest length S to its intermediate length I. el is defined as the ratio of I/L, where L is the particle's longest length. The scheme of Bagheri and Bonadonna [2016] distinguishes between random, minimum (i.e., particles settling with their smallest projection area downward), and maximum drag orientation (i.e., particles falling with their maximum projection area normal to gravity). Tatsii et al. [2024] introduced an average between the predictions for random and maximum drag orientation. This average orientation allows for some oscillations around maximum drag orientation. The following expression for the drag coefficient of non-spherical particles is proposed by Bagheri and Bonadonna [2016, 2019]:

$$C_D = \frac{24\ k_S}{Re}(1 + 0.125(Re\ k_N/k_S)^{2/3}) + \frac{0.46\ k_N}{1 + 5330/(Re\ k_N/k_S)} \tag{1.7}$$

k_S and k_N are the Stokes' and Newton's drag corrections:

$$k_S = (F_S^{1/3} + F_S^{-1/3})/2 \tag{1.8}$$

$$k_N = 10^{\alpha_2(-\log(F_N))\beta_2} \tag{1.9}$$

α_2 and β_2 are empirical expressions defined as:

$$\alpha_2 = 0.45 + \frac{10}{\exp(2.5 \log \rho') + 30} \tag{1.10}$$

$$\beta_2 = 1 - \frac{37}{\exp(3 \log \rho') + 100} \tag{1.11}$$

ρ' is the particle-to-fluid density ratio. For elongated particles, a simple version of the model is used, which neglects the term $\frac{d_{eq}^3}{L\ I\ S}$ in the Stokes' form factor F_S and in Newton's form factor F_N:

$$F_S = fl\ el^{1.3}\ (\frac{d_{eq}^3}{L\ I\ S}) \tag{1.12}$$

$$F_N = fl^2\ el\ (\frac{d_{eq}^3}{L\ I\ S}) \tag{1.13}$$

1.3. Atmospheric Transport Models

Non-spherical particles experience greater drag than volume-equivalent spheres [Bagheri and Bonadonna, 2016]. This, in turn, reduces their terminal settling velocities and allows for longer atmospheric residence times and, thus, larger transport distances [Tatsii et al., 2024, Bagheri and Bonadonna, 2016, Saxby et al., 2018]. If atmospheric transport models assume airborne particles as perfect spheres, which is often the case, their atmospheric transport distances are greatly underestimated. This was demonstrated by Tatsii et al. [2024] for microplastic fibers. The authors implemented the empirical gravitational settling scheme of Bagheri and Bonadonna [2016] into their atmospheric transport model and showed that the settling velocities of uniform fibers are reduced by up to 76% compared to those of spheres of the same volume. Moreover, average atmospheric transport distances of fibers with aspect ratios of 20, 50, and 100 are 157 $\pm$ 26, 272 $\pm$ 50, and 394 $\pm$ 79% greater than those for spheres, respectively. The authors showed that fibers are more likely to reach remote locations on Earth compared to volume-equivalent spheres and that microplastics can be transported in the atmosphere to nearly any point on the globe. Reininger [2024] showed that the model of Bagheri and Bonadonna [2016] can realistically predict the settling velocities of microplastic films (glitter particles) and industrially manufactured microplastic fibers as well, with differences between modeled and experimental values of less than 10 % for individual particles. Similar to the fibers of Tatsii et al. [2024], the settling velocities of the industrially made fibers are reduced up to 79 % and those of the glitter particles up to 74 % compared to those of spheres of the same volume [Reininger, 2024].

Here, the results of global simulations of the atmospheric transport of glitter particles are presented when the scheme of Bagheri and Bonadonna [2016] is implemented into FLEXPART. Glitter particles of seven different commercially available sizes are released in five cities representing different climatic regions to evaluate their mean transport distances and atmospheric residence times. Global deposition patterns are examined as well. The results are then compared to those of spheres of equivalent volume. This is done to investigate how far glitter released during carnivals and festivals, for example, can be transported in the atmosphere and pollute ecosystems. Furthermore, a better understanding of the impact of shape on the particle's transport in the atmosphere should be established. Tatsii et al. [2024] demonstrate that the atmospheric transport distances of microplastic fibers are greatly enhanced compared to volume-equivalent spheres; this work aims to investigate whether the same applies to microplastic films.

2. Material and Methods

2.1. Global Atmospheric Transport of Glitter Particles

2.1.1. FLEXPART

To simulate the atmospheric transport of microplastic films, a modified version of the Lagrangian transport and dispersion model FLEXPART version 11 [Bakels et al., 2024] was used. FLEXPART simulates the transport, turbulent diffusion, dry and wet deposition, decay, and first-order chemical reactions of tracers from local to global scales released from point, line, area, or volume sources [Pisso et al., 2019]. Developed for calculating the long-range and mesoscale transport of hazardous substances from point sources, the application of FLEXPART now encompasses a large range of atmospheric gases and aerosols, e.g., greenhouse gases, black carbon, and volcanic ash, and it has also been used to study the atmospheric branch of the water cycle [Pisso et al., 2019]. It is an offline model that calculates particle trajectories using interpolated meteorological fields (i.e., grid-scale three-dimensional fields of wind velocities, density, temperature, specific humidity, cloud liquid and ice water content, and surface characteristics) [Garcia-Carreras et al., 2015]. FLEXPART works with meteorological input data from the European Centre for Medium-Range Weather Forecasts (ECMWF) and data from the National Center for Atmospheric Predictions (NCEP) forecast systems: Integrated Forecasting System (IFS) and Global Forecast System (GFS) Bakels et al. [2024]. Important for this study is the improved gravitational settling scheme of FLEXPART version 11 that is called at each time step and added to the vertical motion of aerosols. While previous versions of FLEXPART only considered spherical particles, FLEXPART 11 contains improvements for calculating the drag coefficient and calculates the settling and dry deposition velocity also for non-spherical particles [Bakels et al., 2024]. This was done by implementing the scheme of Bagheri and Bonadonna [2016] that provides the drag coefficient for the orientations described in Section 1.2.1 (maximum, random, and an average between those two that has been introduced by Tatsii et al. [2024]).

2.1.2. FLEXPART simulations

The atmospheric transport of seven common sizes of commercially sold glitter and their volume-equivalent spheres was simulated. Properties of the glitter particles used for the simulations are given by Table 2.1. Since these glitter particles are still considerably thick, the atmospheric transport of square films with thicknesses of 10 µm (a common thickness for cling wrap) and 1 µm was simulated as well. The glitter particles were assumed to be hydrophobic and, therefore, inefficient cloud condensation nuclei [Evangeliou et al., 2020]. The particles' efficiency as cloud condensation nuclei and ice nuclei was chosen as 0.001 and 0.01, respectively, leading to relatively inefficient wet deposition. The trajectories of the particles were terminated after two months.

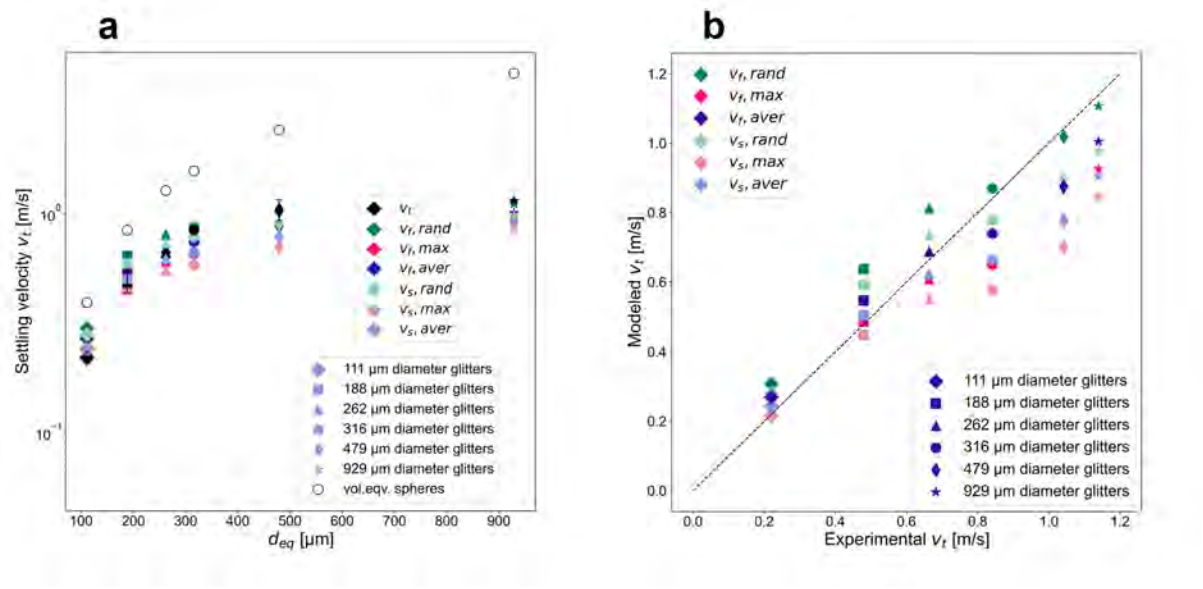

Figure 2.1.: Settling velocities as a function of particle size, expressed as the diameter of a sphere of equivalent volume (a) Reininger [2024]. Modeled values using the shape correction scheme are shown as black circles for spheres and as colored symbols for glitters. Different marker shapes represent the different glitter sizes. Experimental settling velocities v_t are represented by black symbols. Black error bars show the standard deviation of the experimental velocities. Scatter plot of measured and modeled settling velocities of the glitter particles (b) Reininger [2024]. Modeled values are coded by shape for the size of the glitter particle and by color for the type of shape correction scheme (random $v_{t,rand}$, maximum $v_{t,max}$, and average $v_{t,aver}$) and model (full (f) or simple (s)).

The experiments of Reininger [2024] show that, on average, the Bagheri and Bonadonna [2016] scheme with maximum drag orientation configuration predicts the settling velocities of 0.1 mm, 0.2 mm, 0.4 mm, 0.6 mm, 1 mm, and 3 mm diameter glitters best (Figure 2.1). Therefore, the model of Bagheri and Bonadonna [2016] with maximum drag orientation configuration was chosen for the FLEXPART simulations.

For the year 2020, 2500 glitters, films, and their respective volume-equivalent spheres were released instantly at a height of 10-100 m above ground level once per day at 15:00 local time in five different cities. These cities are located in different climatic regions and should give a representative range of meteorological conditions controlling wet and dry deposition: London (51°30'N 0°7'W), Shanghai (31°13'N 121°28'E), Brasília (15°47'S 47°52'W), Cairo (30°1'N 31°14'W), and Reykjavìk (64°7'N 21°49'W). As input for the simulations, ECMWF ERA5 global meteorological fields at 0.50.5 horizontal and 1-hour temporal resolution were used [Hersbach et al., 2020]. The output consisted of two-dimensional wet and dry deposition fields with a grid resolution of 0.5 ° x 0.5 ° and

a nested grid around the release point with a resolution of 0.005 °. Based on the output, average atmospheric residence times and transport distances were determined. The mean atmospheric transport distance is calculated from the distance of grid cell ij from the release point and the total mass deposited in grid cell ij:

$$\bar{D} = \frac{\sum_{ij} D_{ij} \cdot M_{ij}}{\sum_{ij} M_{ij}} \tag{2.1}$$

The relative decrease in total atmospheric particle mass as a function of time was averaged over the number of releases and fitted to $y = e^{-\frac{1}{t_e}t}$. Residence times were then determined as e-folding times t_e.

d_{eq} (µm)		L (µm)	I (µm)	S (µm)	ρ (g/cm^3)	fl	el	Ψ
27	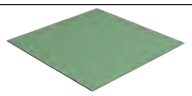	100.0	100.0	1.0	1.4	0.01	1.00	0.11
43		50.0	43.3	25.0	1.4	0.58	0.87	0.83
58		100.0	100.0	10.0	1.4	0.10	1.00	0.44
111		175.8	132.3	26.7	1.4	0.20	0.75	0.71
188	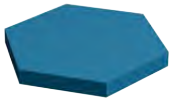	305.9	247.5	56.8	1.4	0.23	0.81	0.64
262		496.5	405.4	58.6	1.4	0.14	0.82	0.53
316	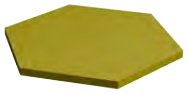	672.2	538.9	56.5	1.4	0.10	0.80	0.45
479		1270.7	996.4	57.5	1.4	0.06	0.78	0.31
929	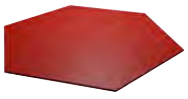	3287.1	2683.1	59.8	1.4	0.02	0.82	0.19

Table 2.1.: Properties of the glitter particles and square films used for the FLEXPART simulations. d_{eq} is the diameter of the volume-equivalent sphere. L is the longest length of the glitter particle, I the intermediate, and S the shortest length. fl is the particle's flatness S/I and el is its elongation I/L. Ψ is the sphericity $\pi d_{eq}^2/SA$, with SA being the surface area of the particle. For 0.05 mm diameter glitters, typical commercially sold dimensions are used as input values for FLEXPART. For all other sizes, the mean values for L, I, and S were determined with a laser microscope by Reininger [2024].

3. Results

3.1. Atmospheric Transport Distances

The mean horizontal atmospheric transport distances of the glitter particles, films, and their volume-equivalent spheres are reported in Table 3.1. The bar charts in Figure 3.1 compare the average atmospheric transport distances and their standard deviations for each release point.

3.1.1. Differences between sizes

In general, the mean atmospheric transport distance decreases with increasing particle size. The smallest particles, square films with $d_{eq} = 27$ µm, travel furthest with (245.33 ± 73.90) km. The smallest glitters ($d_{eq} = 43$ µm) are transported for (52.37 ± 9.88) km. The mean travel distance of square films with $d_{eq} = 58$ µm is (42.94 ± 7.51) km. Interestingly, the mean atmospheric transport distances of 188–929 µm diameter particles are almost the same, and the differences lie within the respective standard deviations: 111 µm diameter glitters travel (18.08 ± 3.47) km, 188 µm diameter glitters (13.99 ± 3.83) km, and 262 µm diameter glitters (13.48 ± 3.92) km. 316, 479, and 929 µm diameter glitters are transported for (13.33 ± 3.95) km, (13.10 ± 4.03) km, and (12.93 ± 4.09) km, respectively. It is particularly surprising since 929 µm diameter glitters settle 2.4 times faster than 188 µm diameter glitters according to the measurements of Reininger [2024]; nevertheless, their mean travel distances are with (13.99 ± 3.83) km and (12.93 ± 4.09) km almost the same.
For the simulations, the maximum drag orientation configuration of the Bagheri and Bonadonna [2016] scheme is used. This configuration agrees particularly well with the measurements for small particles; however, for 316–929 µm diameter particles, it might underestimate the settling velocities. Random orientation fits better for these particles, as can be seen in Figure 2.1. Nevertheless, 929 µm diameter glitters settle still 1.9 times faster than 188 µm diameter glitters according to the model of Bagheri and Bonadonna [2016] when maximum drag orientation configuration is used and can therefore not explain this.
However, convection could explain this phenomenon, as particles were released in the afternoon, when convective conditions prevail. If particles of these sizes get into a convective updraft, they are carried up to much greater heights than they would reach otherwise. Particle settling velocities are far slower than convective velocities, which are several meters per second. Therefore, regardless of their settling velocities, the particles might reach the top of the boundary layer, which leads to much longer transport distances. Downdrafts might at least be of the same order of magnitude as the settling velocities of the particles - therefore, settling velocities are not controlling the time scales.

3.1.2. Differences between shapes

Across all release points, the mean atmospheric transport distances of glitters are between 2.5 % and 20.5 % greater than those of volume-equivalent spheres, while the average travel distances of square films are 44.6 % and 122.7 % larger than those of spheres. For both glitters and films, the differences are within their respective standard deviations. The largest differences occur for the smallest particle sizes, even though the measurements of Reininger [2024] show that the opposite is the case for the settling velocities. The differences between the mean atmospheric transport distances of glitters with d_{eq} = 188, 262, 316, 479, and 929 µm and those of their volume equivalent spheres are only minor.
The differences between films and spheres are much larger than for glitters and spheres, even though the differences between nonspherical and spherical particle are similar. The model of Bagheri and Bonadonna [2016] suggests that the settling velocities of spheres are 1.8 and 3.2 times higher than those of films. For glitters, the measurements of Reininger [2024] show similar results: the settling velocities of spheres are between 1.7 and 3.8 times larger than those of glitters. The scheme of Bagheri and Bonadonna [2016] with horizontal orientation configuration even suggests that spheres settle between 1.2 and 5.2 times faster than glitters.
43 µm diameter glitters and spheres both have low settling velocities (63 mm/s and 73 mm/s) and are transported far in the atmosphere, which could be a reason for the small differences between spheres and nonspherical particles. However, these glitter sizes have a high sphericity, which could explain the similar settling velocities and travel distances. 111 mm diameter glitters display the largest differences among the glitters, which could be due to a combination of a lower sphericity than 43 µm diameter glitters and low terminal settling velocities. 188-929 µm diameter glitters and spheres have settling velocities larger than 400 mm/s and would probably settle fast without convection. The settling might again be determined by the time scales of turbulence rather than their settling velocities, which could explain the small differences. All in all, the transport of giant particles is simulated here and smaller, thinner glitters with low sphericity might show larger differences between glitters and spheres in the horizontal displacement.

3.1.3. Differences between release points

There is not much difference between the mean transport distances of particles released at different locations. Particles released in Cairo experience the largest transport distances, which might be a consequence of the dry climate. 43 µm diameter particles released there have the potential to pollute not only soils and ecosystems in the city but also surrounding agricultural areas and the Nile Delta, since, according to the simulations, glitters and spheres travel 67 and 62 km on average, respectively, when released in Cairo. All other glitter sizes travel between 23 and 17 km on average when released in that city. Their volume equivalent spheres travel between 19 and 17 km. 58 µm diameter films can even reach the Mediterranean Sea and the Red Sea, as they travel 55 km on when released there. Their volume-equivalent spheres are transported for only 38 km. 27 µm diameter films travel 350 km when released in Cairo and might even be transported across country boundaries. Their volume-equivalent spheres travel only 146 km on average.

Particles with $d_{eq} = 43$ µm display with 59 km the second largest transport distances when released in London. Volume-equivalent spheres are also transported far with 46 km. Glitters of that size don't only have the potential to pollute the city of London but also cities and villages close by, fields, and water bodies, including the Thames and the North Sea. However, the transport distances of particles that are larger than 43 µm are significantly smaller compared to the other locations, lying only between 12 and 5 km. For spheres, the average travel distances lie between 8 and 5 km. Therefore, the atmospheric transport distances of particles with $d_{eq} \geq$ 188 µm released in London are not even half of the distances of equally sized particles released in the other locations. These particles may be distributed over London, however, if the reach the the Thames, they too might be transported to the North Sea. The smallest films travel 273 km on average and have the potential to pollute large parts of the United Kingdom and even reach Belgium, the Netherlands, and France. Volume-equivalent spheres are transported for 127 km and may therefore pollute ecosystem in the United Kingdom, the North Sea and the English Channel. 58 µm diameter films and spheres are transported on local scales, with 47 and 28 km, respectively.

43 µm diameter particles released in Brasília can be subject to urban-scale and suburban transport and may lead to the pollution of soils and ecosystems within the city and its periphery, and even national parks close to the city within a distance of 49 km. Spheres of that volume can pollute the surroundings within a distance of 45 km. Larger glitter sizes pollute the city and nearby villages and fields, with mean travel distances lying between 18 and 13 km. For spheres, the mean travel distances lie between 15 and 14 km. 27 µm and 58 µm diameter films are transported over 280 and 39 km, respectively. Spheres travel 119 and 27 km. The smaller glitters and spheres may therefore affect even ecosystems and cities quite far from Brasiília.

Glitters and spheres released in Reykjavík may be deposited in the city, its surroundings, including villages and fields, and the North Atlantic Ocean. 43 µm diameter particles may also be deposited in national parks, as their average travel distances are 48 km, while their volume-equivalent spheres travel 45 km on average. Larger glitters may pollute the city and its surroundings, including coast and ocean within distances between 19 and 14 km; spheres pollute the periphery within a distance of 16 and 13 km. Films and spheres with $d_{eq} = 27$ µm travel 172 and 90 km on average when released in this city. Glitters therefore may pollute large parts of Iceland, including protected areas, and be deposited in the Atlantic Ocean. 58 µm diameter glitters and spheres are only transported over 41 and 30 km on average.

When released in Shanghai, glitters and spheres have the potential to pollute not only the city of Shanghai, but surrounding cities, the Yangtze River, and Hangzhou Bay as well. 43 µm diameter glitters and spheres travel 38 and 33 km on average. Larger glitters travel between 18 and 15 km, spheres between 16 and 15 km. 27 and 58 µm diameter films travel 151 km and 33 km, respectively, spheres 70 and 25 km. Small films in particular may be deposited in the East China Sea and local ecosystems.

d_{eq} (µm)		Mean travel dist. glitters (km)		Mean travel dist. spheres (km)	Rel. difference (%)
27	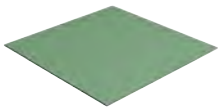	245.33 ± 73.90		110.41 ± 27.07	122.7 ± 37.1
43		52.37 ± 9.88		46.15 ± 9.46	13.3 ± 3.4
58		42.94 ± 7.51		29.58 ± 4.61	44.6 ± 6.5
111	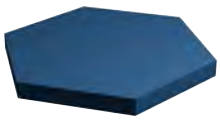	18.08 ± 3.47		14.94 ± 3.72	20.5 ± 5.7
188	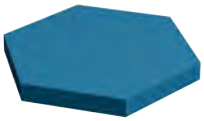	13.99 ± 3.83		13.03 ± 4.03	7.2 ± 3.2
262		13.48 ± 3.92		12.77 ± 4.14	5.4 ± 3.0
316	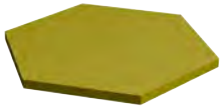	13.33 ± 3.95		12.70 ± 4.19	4.8± 2.8
479		13.10 ± 4.03		12.63 ± 4.21	3.6 ± 2.4
929		12.93 ± 4.09		12.61 ± 4.21	2.5 ± 1.9

Table 3.1.: Mean travel distances of glitters and their volume equivalent spheres. d_{eq} is the diameter of the volume-equivalent sphere.

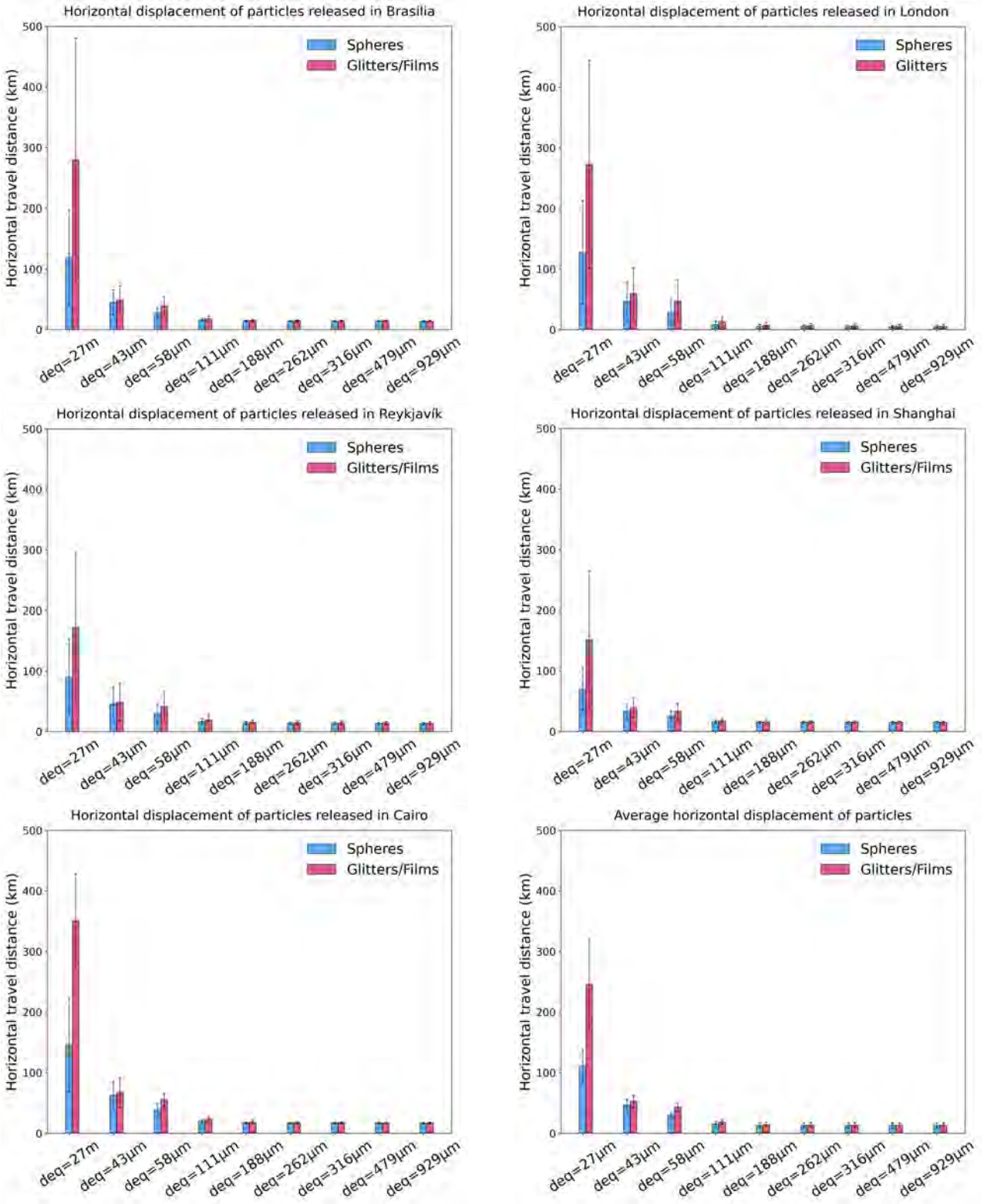

Figure 3.1.: Average horizontal transport distances (colored bars) and their standard deviations (whiskers) for glitters and films (pink) and their volume-equivalent spheres (blue).

3.2. Atmospheric Residence Times

The atmospheric residence times, determined as e-folding times t_e from the relative decrease in atmospheric particle mass, have been averaged over all release points and are listed in Table 3.2. Figures 3.2 - 3.10 depict the mass fraction frequency distribution over time and the e-folding times of glitters/films and spheres.

3.2.1. Differences between sizes

In general, just like the atmospheric transport distances, the mean atmospheric residence times of the particles tend to decrease with increasing particle size. Square films with d_{eq} = 27 µm settle after 13.76 h if averaged over all release points. The atmospheric residence times of glitters with d_{eq} = 43 µm are longer (4.18 h) than those of square films with d_{eq} = 58 µm (3.68 h). While the mean atmospheric transport distances of 188-929 µm diameter particles are surprisingly similar, here, this applies even to the mean e-folding times of 111-316 µm diameter glitters. The mean atmospheric residence times of 111, 188, 262, and 316 µm diameter glitters are 1.65 h, 1.60 h, 1.57 h, and 1.66 h, respectively. Glitters with d_{eq} = 316 µm have high average e-folding times, even higher than glitters with d_{eq} = 111 µm, which can be attributed to high e-folding times of those glitters that were released in London. This is surprising, since the measured and modeled settling velocities of 316 µm diameter glitters are 3.8 and 2.7 times higher than those of 111 µm diameter glitters. Moreover, the atmospheric transport distances of 316 µm diameter particles released in London are much smaller compared to the other release points. Again, the reason for this could be the convective conditions when the particles were released. 479 and 929 µm diameter glitters have similar and the shortest e-folding times, namely 1.41 h and 1.38 h, which is in agreement with their atmospheric transport distances.
For spheres, the mean e-folding times drop with particle size from 7.12 h to 1.57 h for 27-111 µm diameter spheres, then they increase again to 1.61 h, 1.81 h, and 1.89 h for 188 µm, 262 µm, and 316 µm diameter spheres. 316 µm diameter spheres also have surprisingly high e-folding times, higher than 111 - 262 µm diameter spheres. 479 µm diameter spheres show the lowest e-folding times with 1.44 h, while the e-folding time increases again for 929 µm diameter spheres to 1.48 h. However, the differences between the atmospheric residence times of 111-929 µm diameter particles are still smaller than expected, similar to the atmospheric transport distances. These particle sizes have similar mass fraction frequency distributions, with only 316 µm diameter spheres being an exceptions; for these particles, the frequency distribution is shifted to the left, indicating that most particles could be deposited earlier.

3.2.2. Differences between shapes

The residence times of the glitters are similar to those of their volume-equivalent spheres. The residence times of square films, on the other hand, differ more strongly from those of their volume-equivalent spheres. Average e-folding times of square films and spheres with d_{eq} = 27 µm over all release points are 13.76 h and 7.12 h, respectively. The decrease of the median mass fraction of the spheres is much steeper than that of films, which also hints at longer residence times compared to spheres. The spread in the mass fraction frequency distribution is broader for

films than for spheres, also showing that occasionally, films can remain airborne substantially longer than spheres of equivalent volume. The mean e-folding times of films and spheres with d_{eq} = 58 µm are 3.68 h and 2.88 h, respectively. Films and spheres show similar mass frequency distributions in Cairo, underlining that both shapes remain aloft for similar time spans. In all other cities, the decrease in median mass fraction of spheres is steeper than for glitters, and also the spread is larger for glitters. For particles with equivalent diameters of 43 µm, a major fraction of them is deposited a few hours after being released. Average e-folding times over all release points of glitters and spheres with d_{eq} = 43 µm are 4.18 h and 4.01 h, respectively. The median mass fraction of glitters with d_{eq} = 43 µm shows a slightly slower decrease compared to spheres, indicating longer residence times. The spread in the mass fraction frequency distribution is broader than that of spheres for these sizes of glitters, suggesting that occasionally, these glitters can remain airborne longer than spheres. For particles with d_{eq} = 111 µm, the difference in residence times becomes less pronounced. The average e-folding times of glitters and spheres with equivalent diameters of 111 µm are 1.65 h and 1.57 h, respectively. The mass frequency distributions of both spheres and glitters are similar. Surprisingly, the mean e-folding times of glitters with equivalent diameters of 188 µm are 1.60 h, while those of spheres with the same volume are 1.61 h. The mass frequency distributions of spheres and glitters are similar, however. Remarkably, glitters released in Shanghai even show a steeper decrease in median mass fraction than the spheres, which is also the case for the average medians. The average e-folding times of glitters with d_{eq} = 262 µm (1.57 h) are shorter than those of volume-equivalent spheres (1.81 h). However, for these particles, the median mass fraction of glitters displays a less steep decrease than that of spheres, hinting at longer residence times of glitters. The mean e-folding times of glitters and spheres with equivalent diameters of 316 µm are 1.66 h and 1.89 h, respectively. For these particle-size, the decrease in median mass fraction of the spheres is steeper than that of the glitters and the mass frequency distribution of the spheres shows a larger spread than those of the glitters. Therefore, glitters may tend to travel further than spheres, despite shorter e-folding times. Additionally, the mass frequency distribution of the spheres is shifted to left compared to glitters. The mean e-folding times of glitters with d_{eq} = 479 µm are with 1.41 h smaller than those of spheres (1.44 h). The spread in the mass frequency distributions is also smaller for spheres, except for the release points Brasília and Shanghai. The slopes of the median mass fractions are similar, only in Brasília, the median mass fraction of the glitters shows a deeper decrease. On average, the median mass fraction of spheres shows a slower decrease. For particles with d_{eq} = 929 µm, spheres show larger e-folding times too, with 1.48 h compared to glitters, with 1.38 h. The median atmospheric mass fraction of the spheres shows a slower decrease compared to glitters too, with Cairo being an exception; for that release point, the median atmospheric mass fractions are similar. Glitters of that size also have a broader spread in the mass fraction frequency distribution.

3.2.3. Differences between release points

Interestingly, the atmospheric residence times of 479 and 929 µm diameter particles are almost the same across all release points. For Cairo and Reykjavík, the atmospheric residence times of 111-929 µm diameter glitters are nearly the same and smaller than the mean values. However, this does not apply to their volume-equivalent spheres. For Brasília, the e-folding times of 188-929 µm

diameter glitters are nearly the same, while those of 111 µm diameter glitters are substantially higher. Again, this cannot be applied to spheres. 43 µm particles released in Brasília have the longest e-folding times. For these three release points, the residence times of the glitters decrease with increasing particle size, with one exception in each case. For the spheres, this trend applies too, but with two exceptions. For Shanghai, the atmospheric residence times of the glitters decrease with increasing size as well. The only exception are 262 µm diameter glitters with high residence times. For this size, the volume equivalent spheres, on the other hand, show relatively small e-folding times, while for 316 µm diameter spheres, the e-folding times are surprisingly high when compared to the mean value. The residence times of the glitters released in London are decreasing with particle size as well, only with two exceptions (188 and 316 µm diameter glitters). Their volume-equivalent spheres have particularly long residence times compared to their mean residence times.

d_{eq} (µm)		Mean res. time glitters (h)		Mean res. time spheres (h)	Rel. difference (%)
27	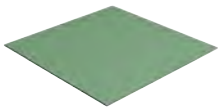	13.76		7.12	93.3
43		4.18		4.01	4.2
58		3.68		2.88	27.8
111		1.65		1.57	5.1
188	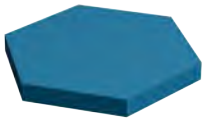	1.60		1.61	0.6
262		1.57		1.81	13.3
316	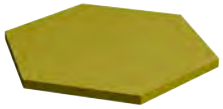	1.66		1.89	12.4
479		1.41		1.44	2.1
929		1.38		1.48	6.8

Table 3.2.: Mean residence times of glitters and their volume equivalent spheres. d_{eq} is the diameter of the volume-equivalent sphere.

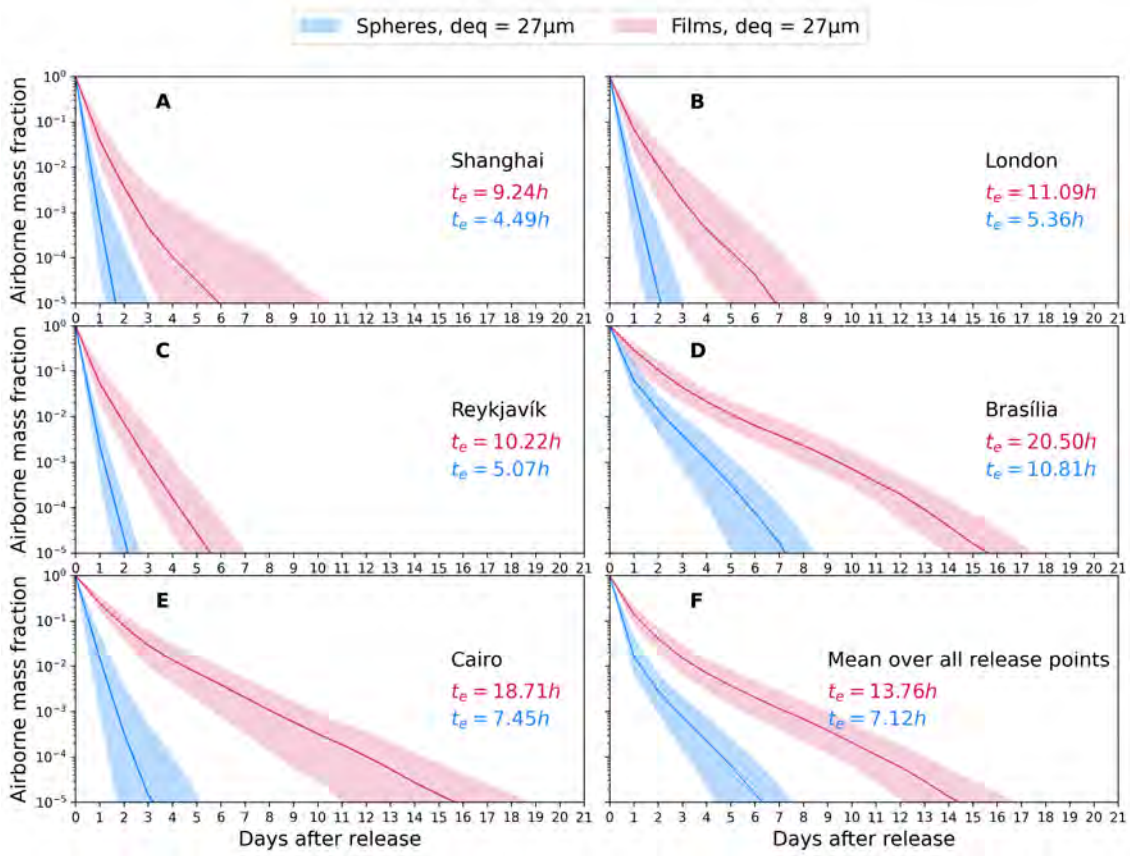

Figure 3.2.: Decrease of the atmospheric concentrations of microplastic films and spheres with d_{eq} = 27 µm as a function of time after released in Shanghai (A), London (B), Reykjavík (C), Brasília (D), and Cairo (E) and averaged over all release points (F). Solid lines depict the median values, and the shading displays the range between the 25th and 75th percentile. E-folding times t_e are reported in each panel.

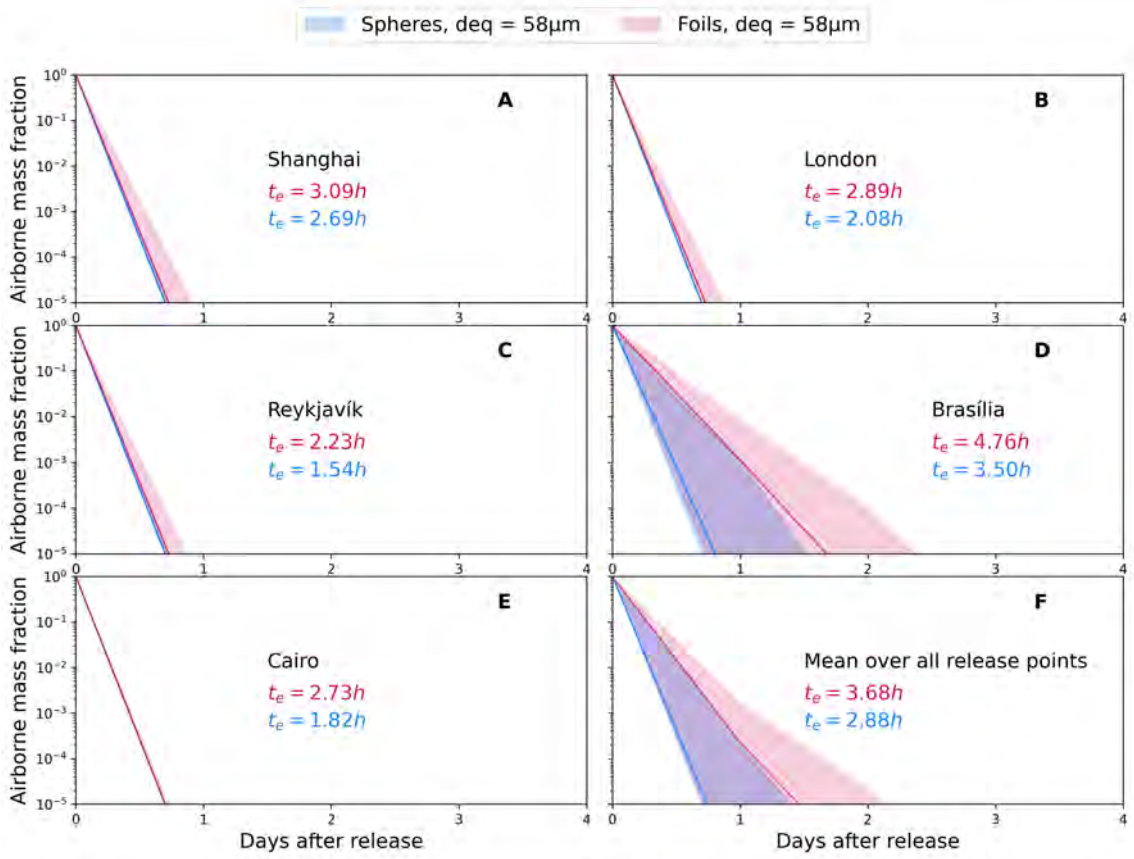

Figure 3.3.: Decrease of the atmospheric concentrations of microplastic films and spheres with $d_{eq} = 58$ µm as a function of time after released in Shanghai (A), London (B), Reykjavík (C), Brasília (D), and Cairo (E) and averaged over all release points (F). Solid lines depict the median values, and the shading displays the range between the 25th and 75th percentile. E-folding times t_e are reported in each panel.

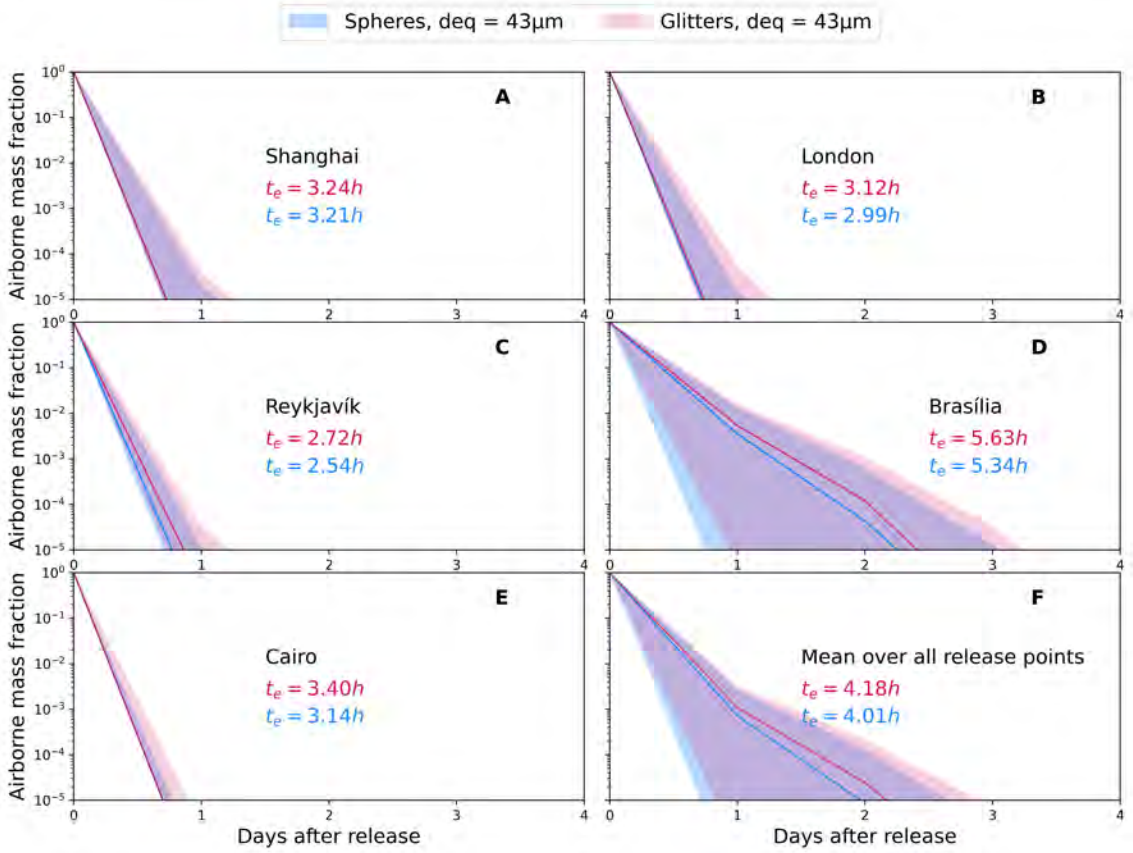

Figure 3.4.: Decrease of the atmospheric concentrations of glitters with $d_{eq} = 56$ µm and their volume-equivalent spheres as a function of time after released in Shanghai (A), London (B), Reykjavík (C), Brasília (D), and Cairo (E) and averaged over all release points (F). Solid lines depict the median values, and the shading displays the range between the 25th and 75th percentile. E-folding times t_e are reported in each panel.

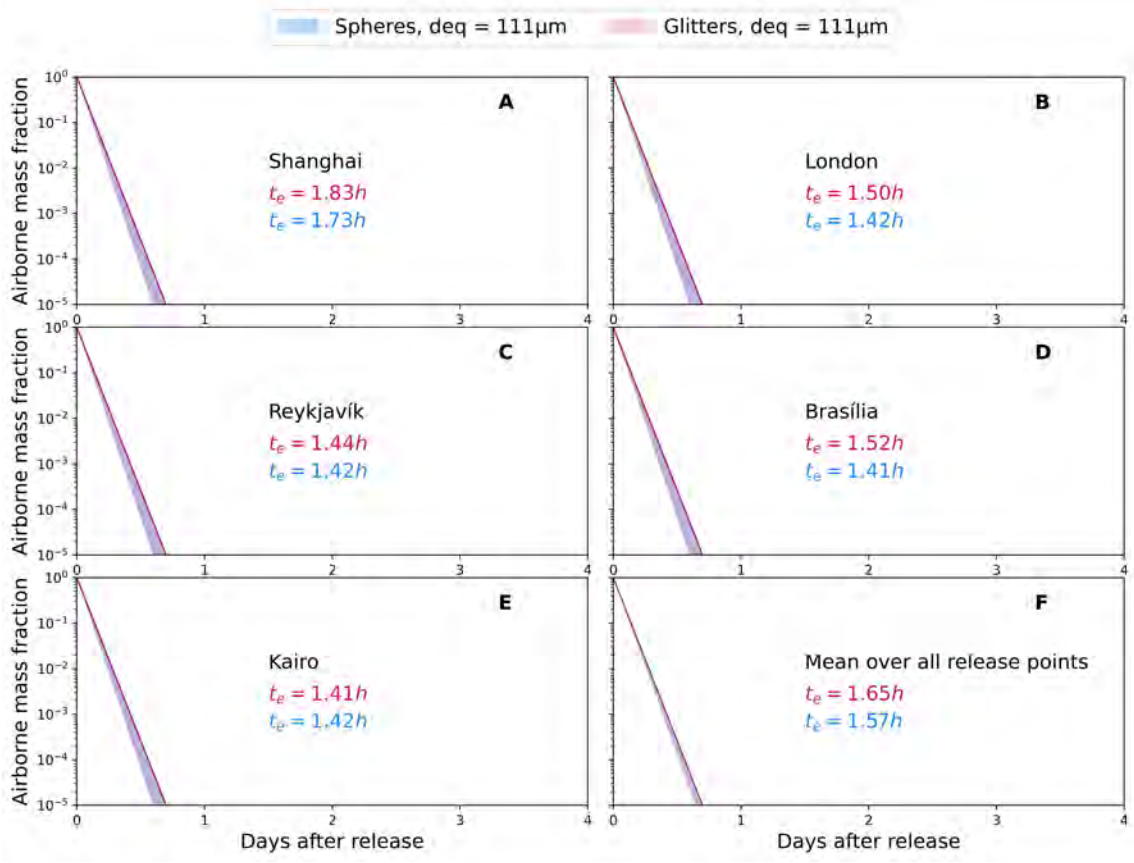

Figure 3.5.: Decrease of the atmospheric concentrations of glitters with $d_{eq} = 111$ µm and their volume-equivalent spheres as a function of time after released in Shanghai (A), London (B), Reykjavík (C), Brasília (D), and Cairo (E) and averaged over all release points (F). Solid lines depict the median values, and the shading displays the range between the 25th and 75th percentile. E-folding times t_e are reported in each panel.

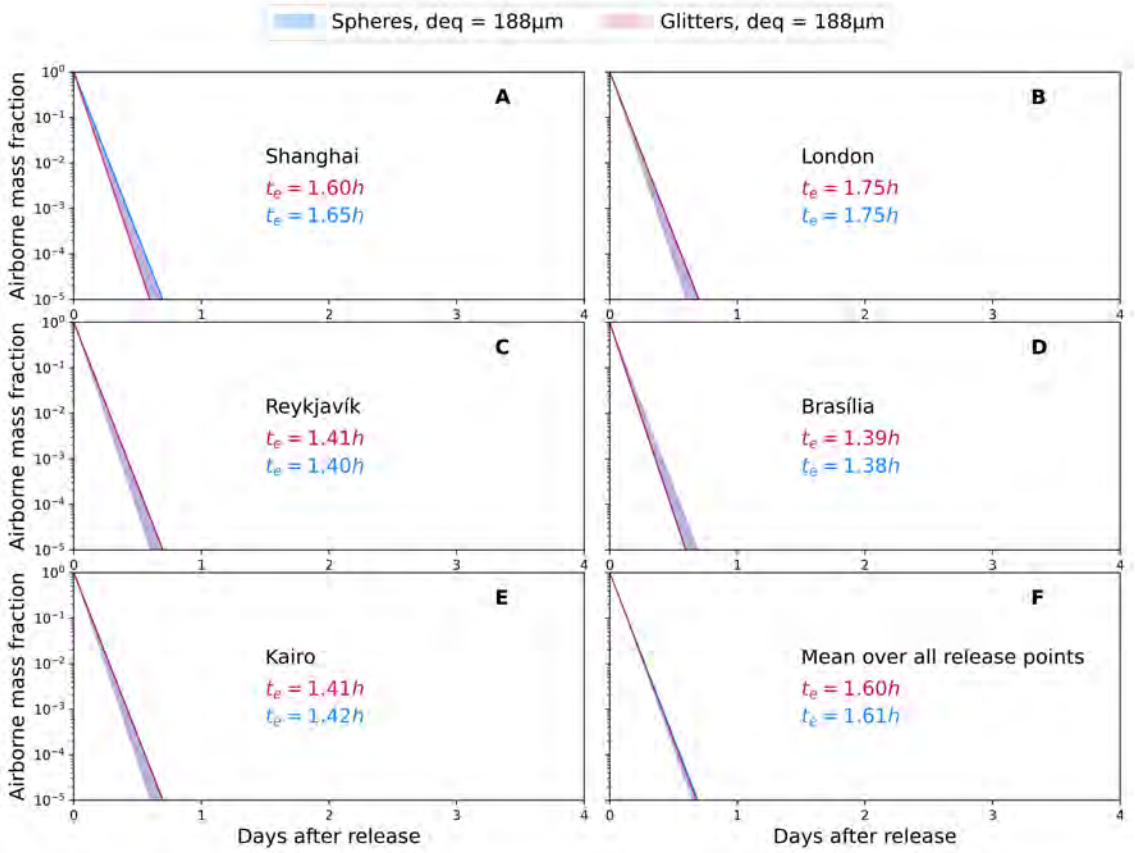

Figure 3.6.: Decrease of the atmospheric concentrations of glitters with $d_{eq} = 188$ µm and their volume-equivalent spheres as a function of time after released in Shanghai (A), London (B), Reykjavík (C), Brasília (D), and Cairo (E) and averaged over all release points (F). Solid lines depict the median values, and the shading displays the range between the 25th and 75th percentile. E-folding times t_e are reported in each panel.

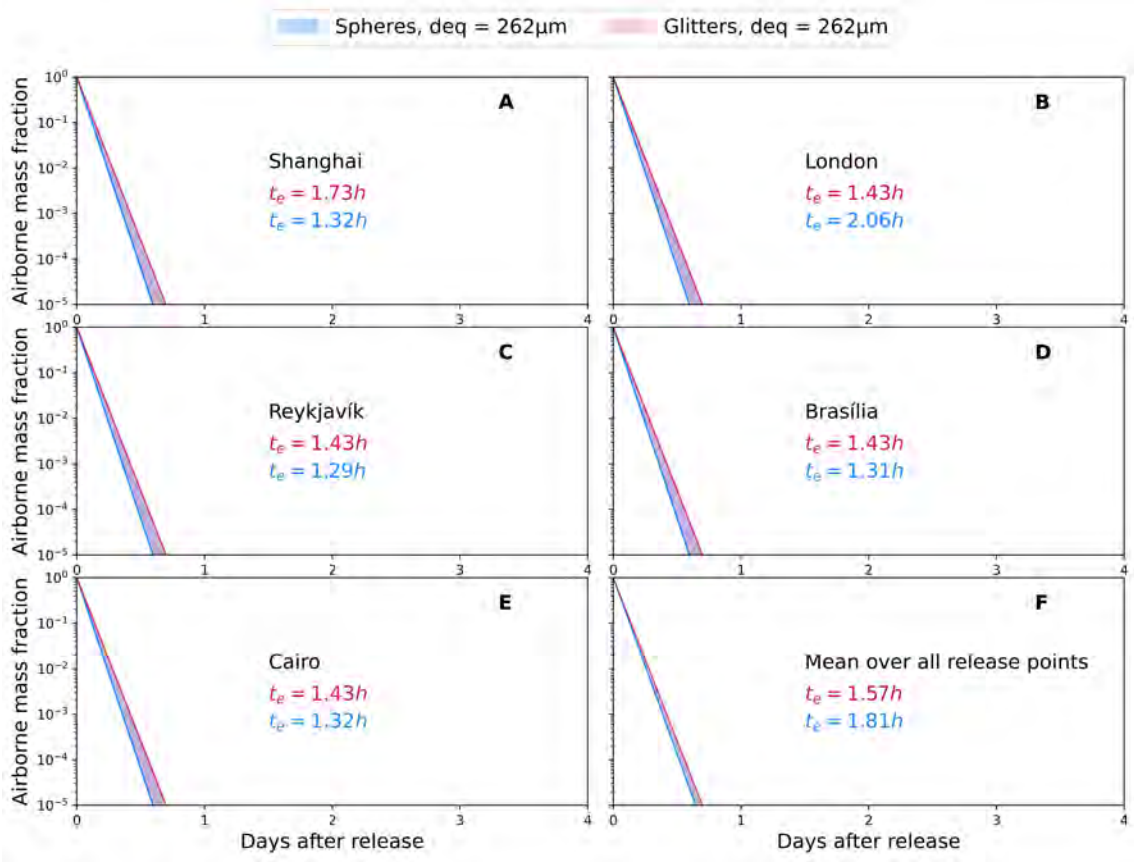

Figure 3.7.: Decrease of the atmospheric concentrations of glitters with $d_{eq} = 262$ µm and their volume-equivalent spheres as a function of time after released in Shanghai (A), London (B), Reykjavík (C), Brasília (D), and Cairo (E) and averaged over all release points (F). Solid lines depict the median values, and the shading displays the range between the 25th and 75th percentile. E-folding times t_e are reported in each panel.

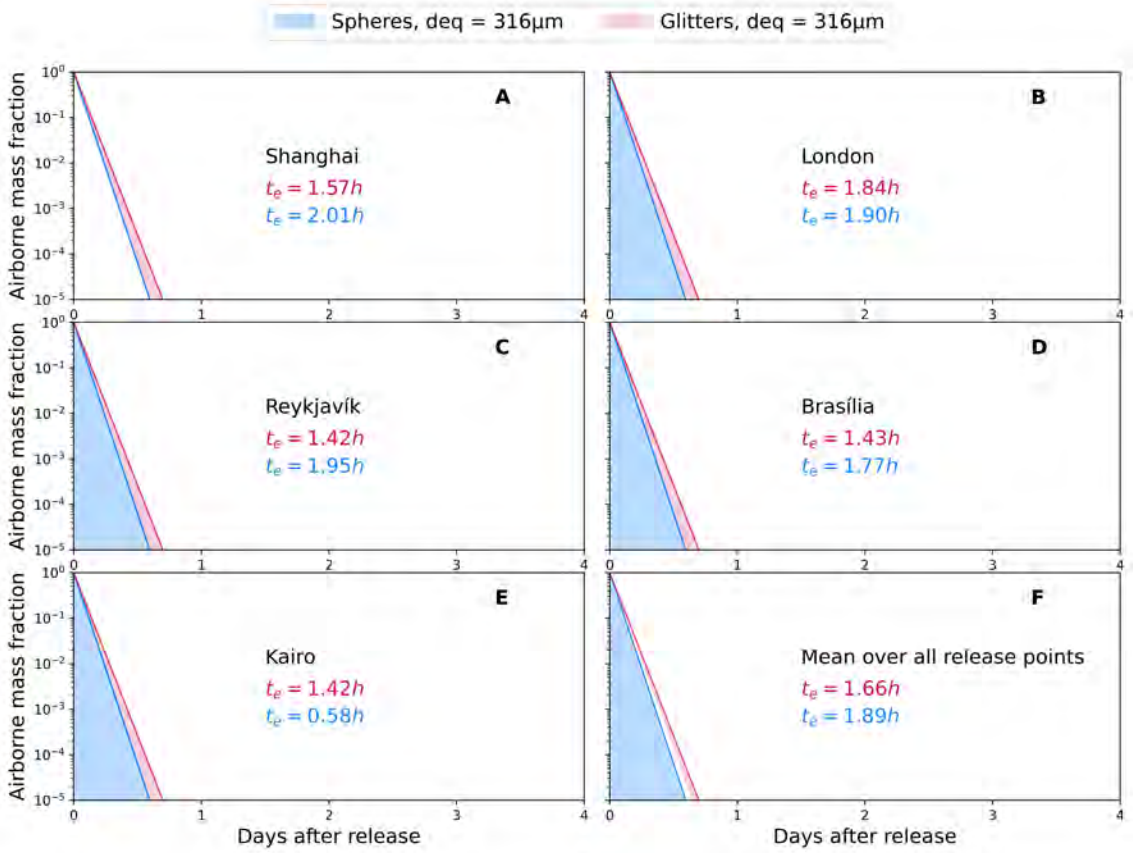

Figure 3.8.: Decrease of the atmospheric concentrations of glitters with $d_{eq} = 316$ µm and their volume-equivalent spheres as a function of time after released in Shanghai (A), London (B), Reykjavík (C), Brasília (D), and Cairo (E) and averaged over all release points (F). Solid lines depict the median values, and the shading displays the range between the 25th and 75th percentile. E-folding times t_e are reported in each panel.

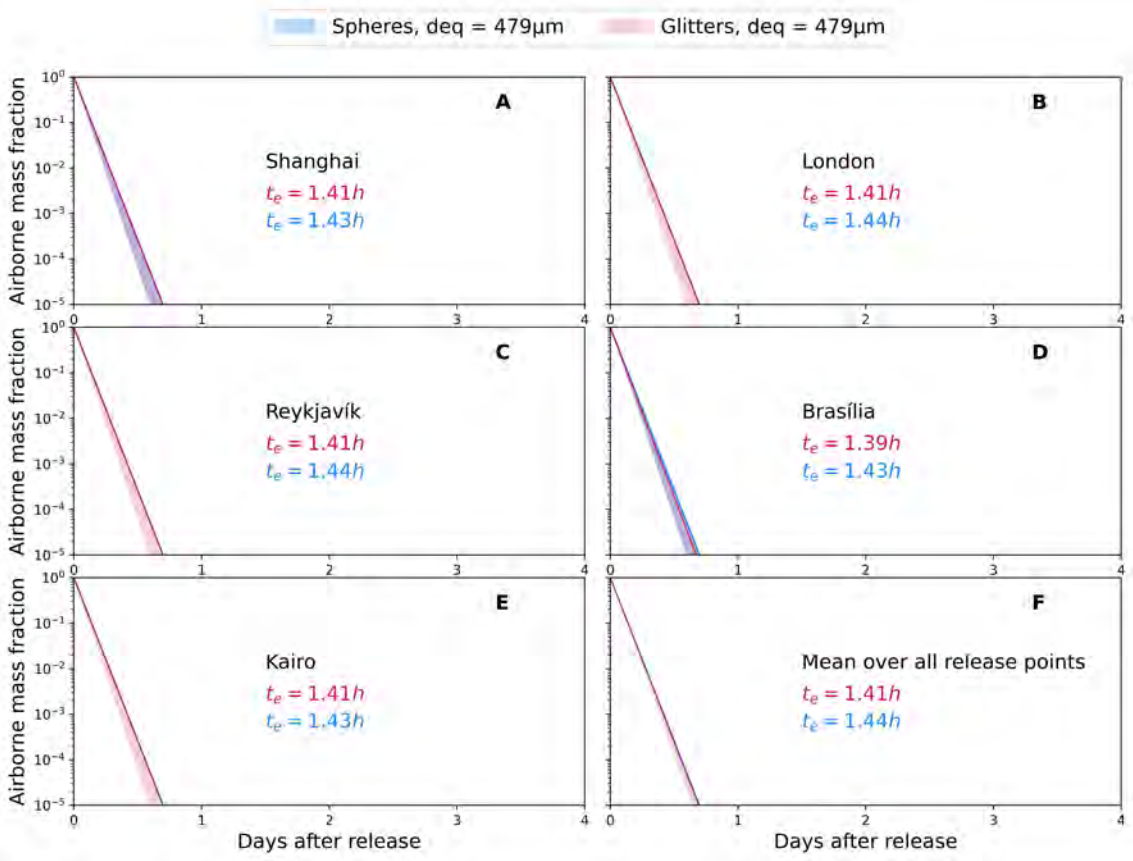

Figure 3.9.: Decrease of the atmospheric concentrations of glitters with $d_{eq} = 479$ µm and their volume-equivalent spheres as a function of time after released in Shanghai (A), London (B), Reykjavík (C), Brasília (D), and Cairo (E) and averaged over all release points (F). Solid lines depict the median values, and the shading displays the range between the 25th and 75th percentile. E-folding times t_e are reported in each panel.

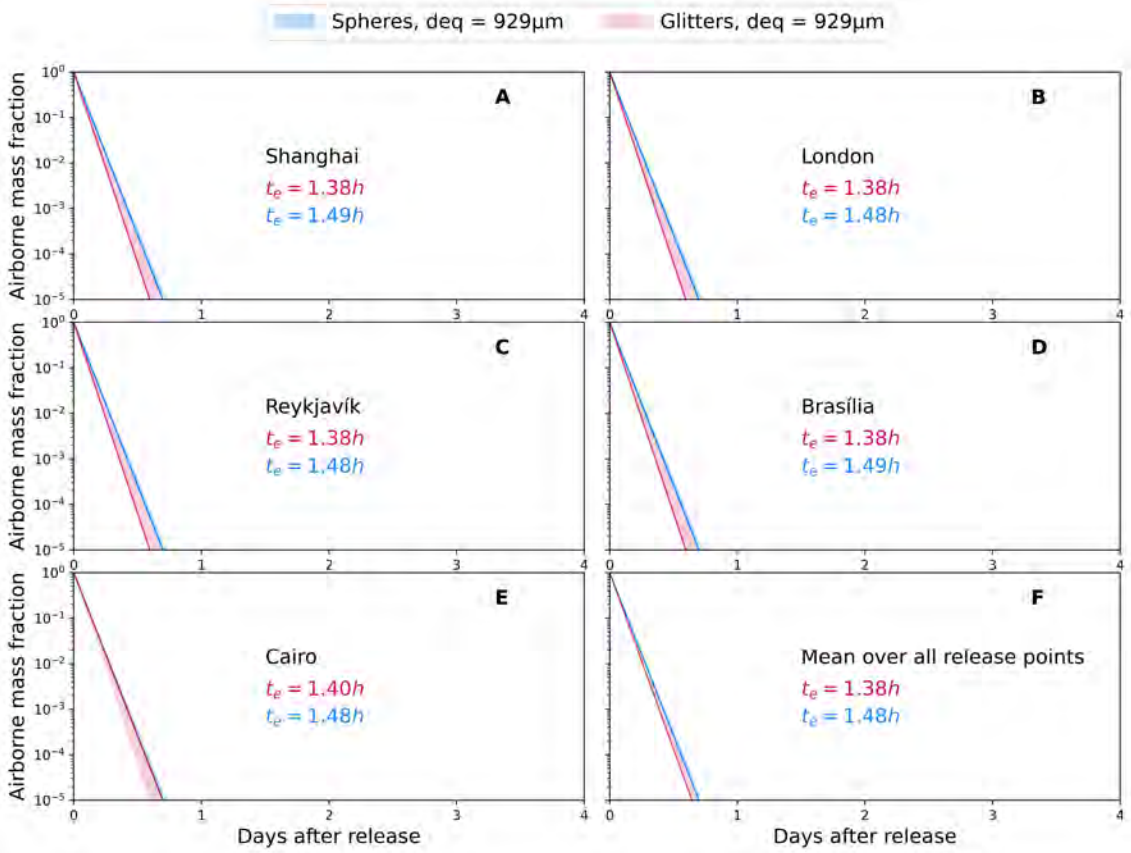

Figure 3.10.: Decrease of the atmospheric concentrations of glitters with d_{eq} = 929 µm and their volume-equivalent spheres as a function of time after released in Shanghai (A), London (B), Reykjavík (C), Brasília (D), and Cairo (E) and averaged over all release points (F). Solid lines depict the median values, and the shading displays the range between the 25th and 75th percentile. E-folding times t_e are reported in each panel.

3.3. Deposition Patterns

Figures 3.11 - A.35 depict the microplastic particles' deposition patterns (A),(B) and height distributions (C) resulting from the FLEXPART simulations. The figures display, both from a wider angle (A) and close up (B), the daily dry and wet deposition of glitters or films and their volume-equivalent spheres released in Cairo, Brasília, London, Reykjavík, and Shanghai, respectively. The deposition patterns of particles released in Cairo and Shanghai are shown in the results, while those for the other release points are listed in the appendix. To demonstrate the difference, daily dry and wet deposition patterns are shown separately for particles with equivalent diameters of 27, 58, and 43 µm.

3.3.1. Differences between particle sizes

The deposition patterns indicate that the atmospheric transport distances decrease with increasing particle size. The smallest particles (d_{eq} = 27, 43, and 58 µm) used in the simulations travel substantially further compared to the other sizes. Particles with equivalent diameters bigger than 43 µm are not transported considerably far globally. The largest particles (d_{eq} = 479 µm and d_{eq} = 929 µm) are deposited closest to their release points. For instance, particles with d_{eq} = 43 µm that were released in Reykjavík are transported to Northwestern Europe and southern Greenland; particles with d_{eq} = 111 µm hardly reach Greenland and Northern Europe; and particles with d_{eq} = 929 µm are not even deposited over all of Iceland. Particles with d_{eq} = 43 µm released in Shanghai are transported over the Pacific Ocean to North America; particles with d_{eq} = 111 µm reach South Korea and Southern Japan; and particles with d_{eq} = 929 µm are not even spread over the entire suburban area of Shanghai.
This is not surprising since the settling velocities of 111 mm diameter glitters are 3.4 times the settling velocity of 43 µm diameter glitters according to the scheme of Bagheri and Bonadonna [2016] and 929 µm diameter glitters settle even 13 times faster than 43 µm diameter glitters.
The differences in the deposition patterns of particles with d_{eq} = 188, 262, and 316 µm are minor. Especially particles with d_{eq} = 262 and 316 µm show similar deposition patterns. This is consistent with the similar atmospheric residence times and transport distances of these particle-sizes, and, as explained before, the reason could be that the transport distances are increased due to convection.

3.3.2. Differences between shapes

The deposition patterns of glitters and their volume-equivalent spheres are remarkably similar. However, glitter particles travel further than their volume-equivalent spheres, even if not substantially. The nested grid (shown in (B) in the figures) is where a difference is most visible. In addition to the deposition patterns, the deposition ratios glitters/spheres or films/spheres have been plotted and are listed in Figures 3.26, 3.27, 3.28, 3.40, 3.41,3.42, 3.43, A.10, A.11, A.12, A.13, A.23, A.24, A.25, A.26, A.36, A.37, and A.38. The reason for the small differences could again be the fact that not the settling velocity but turbulence constrains the time scales. The deposition patterns of square films and spheres with d_{eq} = 27 µm, on the other hand, are clearly different. Films are deposited over the entire northern hemisphere when released in Cairo, while spheres are deposited mainly over Europe, Northern and Western Africa, and Asia. The difference is less pronounced for films and spheres with equivalent diameters of 58 µm, but still more obvious compared to glitters and their volume-equivalent spheres.

3.3.3. Differences between dry and wet deposition

All in all, close to the release point, the total deposition patterns are dominated by dry deposition, as the mass deposited by dry deposition is larger than the mass deposited by wet deposition. This can be seen in Figures 3.12 and 3.13 for 27 µm films. Occasionally, wet deposition can lead to enhanced deposition further away from the source, which becomes apparent in Figures 3.15 and 3.16, where the wet deposition patterns of particles with d_{eq} = 43 µm show enhanced transport to the northern hemisphere compared to dry deposition patterns.

3.4. Atmospheric mass concentration

The vertical distribution of the microplastic particles resulting from the FLEXPART simulations is shown in Figures 3.11 - A.35 (C). Films and glitters reach higher altitudes than spheres. The mean mass concentration of 27 µm diameter films at altitudes greater than 4 km above the surface is 1.9 times higher than for volume-equivalent spheres; for 58 mm diameter films, it is 1.6 times higher. The average mass concentration of 50 µm, 111 µm, and 188 µm diameter glitters is 1.1, 2.5, and 1.7 times higher than those of spheres, respectively. The mass concentrations of 262 µm and 316 µm diameter glitters are 1.1 times larger than those of spheres, and the mass concentrations of 479 µm and 929 µm diameter glitters are 1.4 and 1.9 times larger, respectively. As expected, the total atmospheric mass concentration of glitters, films, and spheres decreases with increasing particle size. For instance, for 27 µm diameter films, the average atmospheric mass concentration is $1.02 \cdot 10^{-9}$ µg/m^3, while for 929 µm diameter glitters, the concentration is $1.32 \cdot 10^{-11}$ µg/m^3. However, larger particles reach surprisingly high altitudes, which supports the theory that convective updrafts increase the residence times and transport distances of these particles. Vertical transport seems to be reduced in Reykjavík compared to the other points of release. In all other release points, glitters are transported higher than 20 km; however, in Reykjavík, this is only the case for 43 µm diameter glitters.

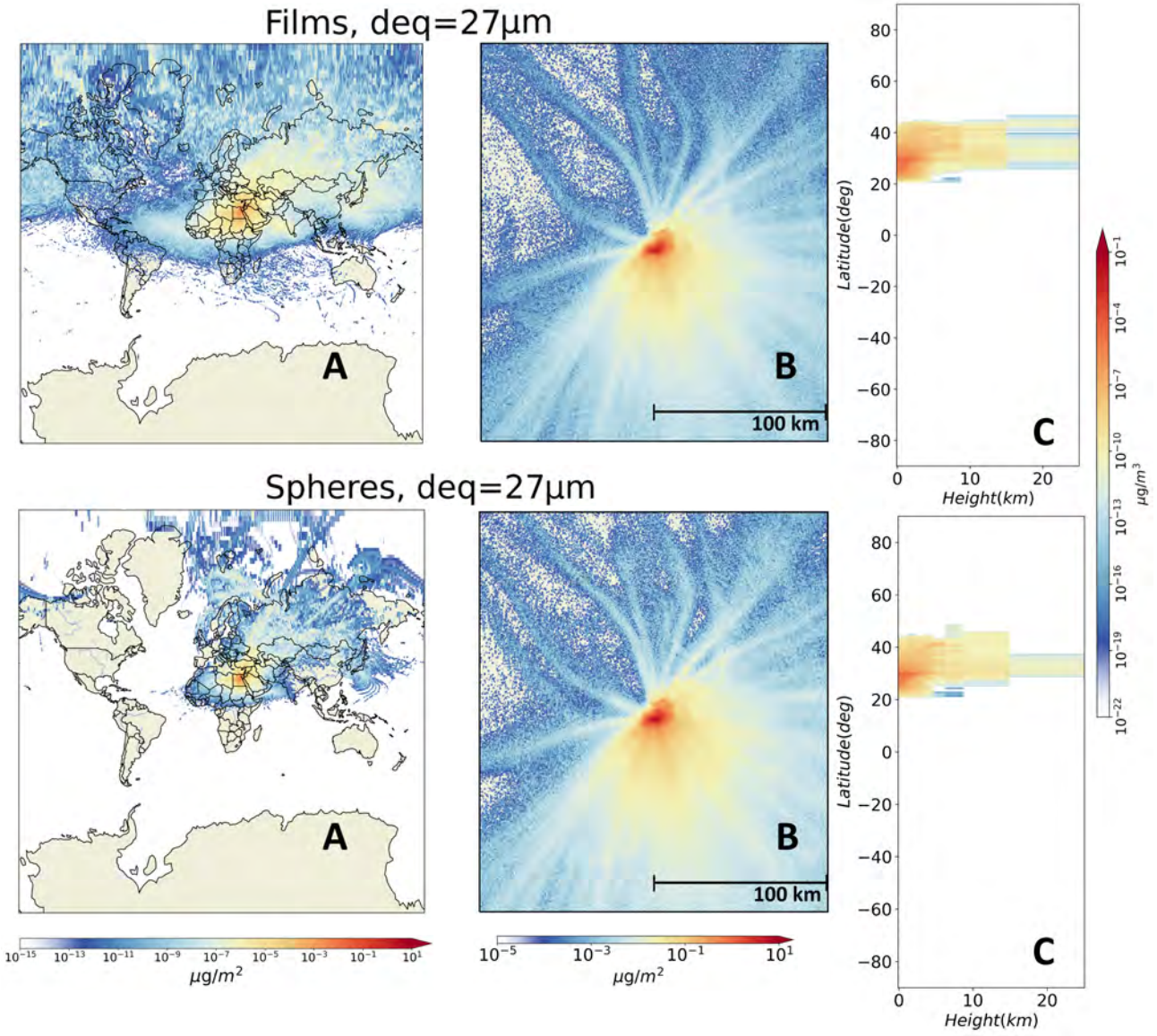

Figure 3.11.: (A) Daily dry and wet deposition of films and spheres with d_{eq} = 27 µm, released in Cairo. (B) Daily dry and wet deposition in the nested grid around the release point Cairo. (C) Zonal mean atmospheric mass concentration as a function of latitude and altitude.

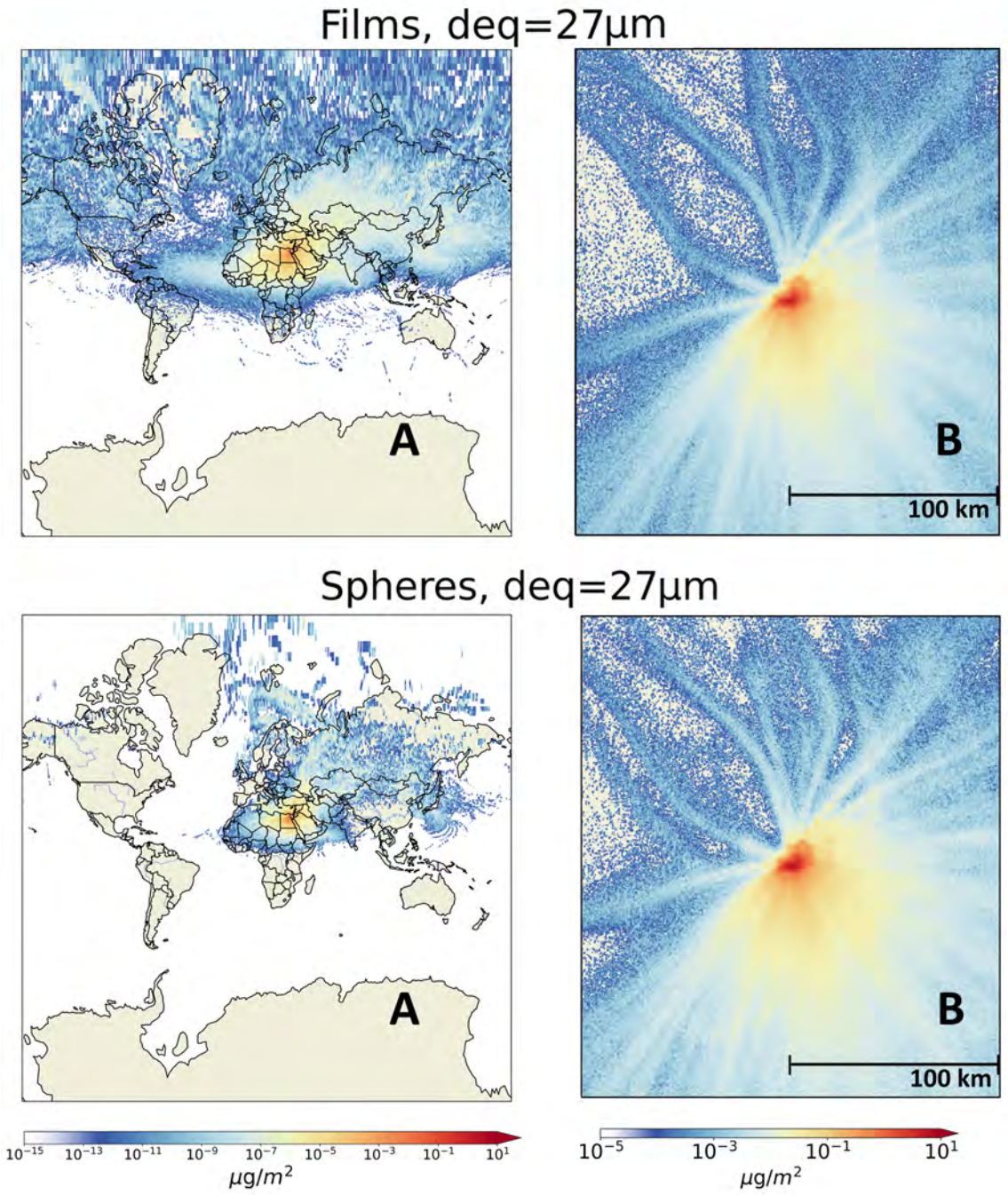

Figure 3.12.: (A) Daily dry deposition of films and spheres with $d_{eq} = 27$ µm, released in Cairo. (B) Daily dry deposition in the nested grid around the release point Cairo.

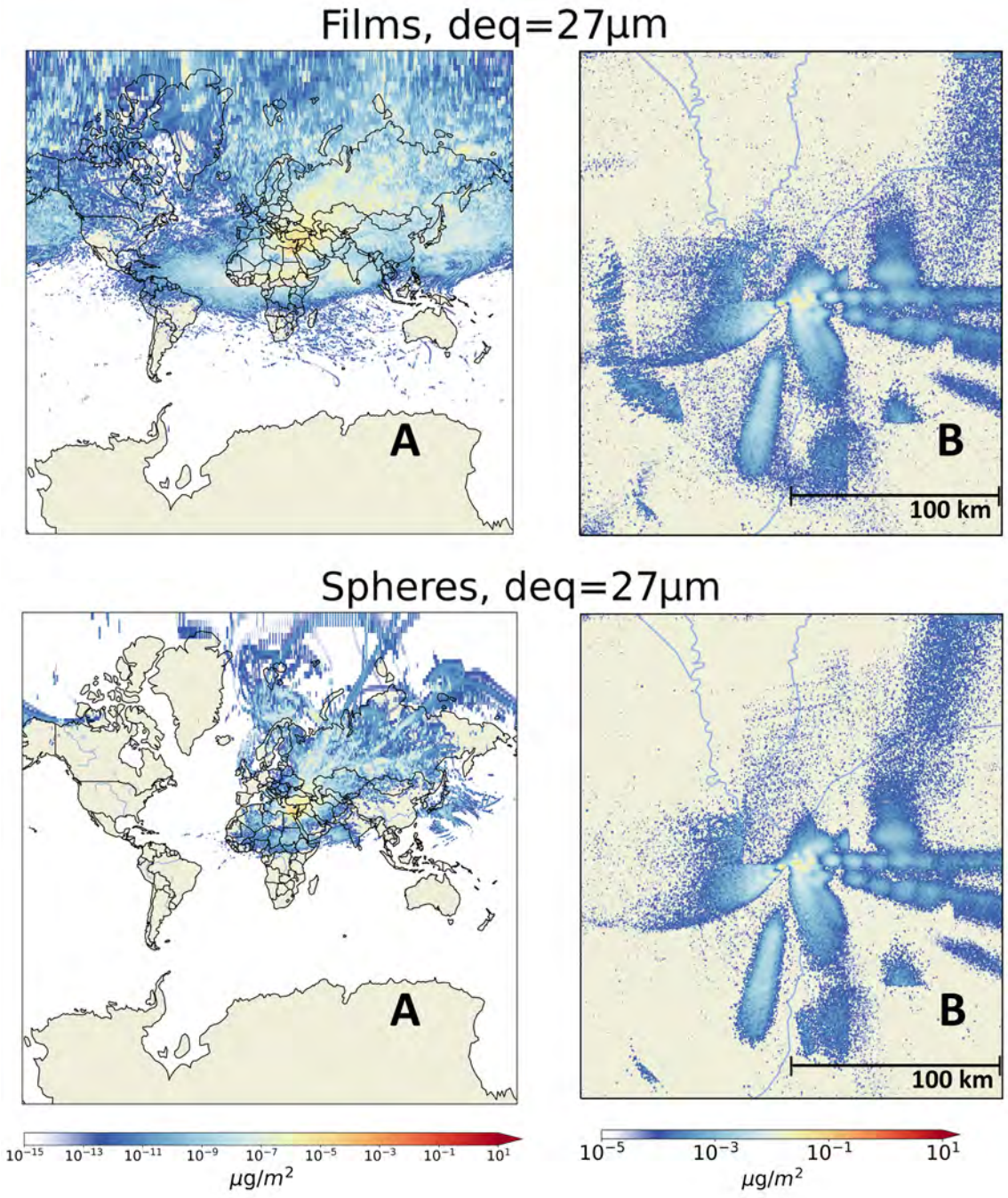

Figure 3.13.: (A) Daily wet deposition of films and spheres with d_{eq} = 27 µm, released in Cairo. (B) Daily wet deposition in the nested grid around the release point Cairo.

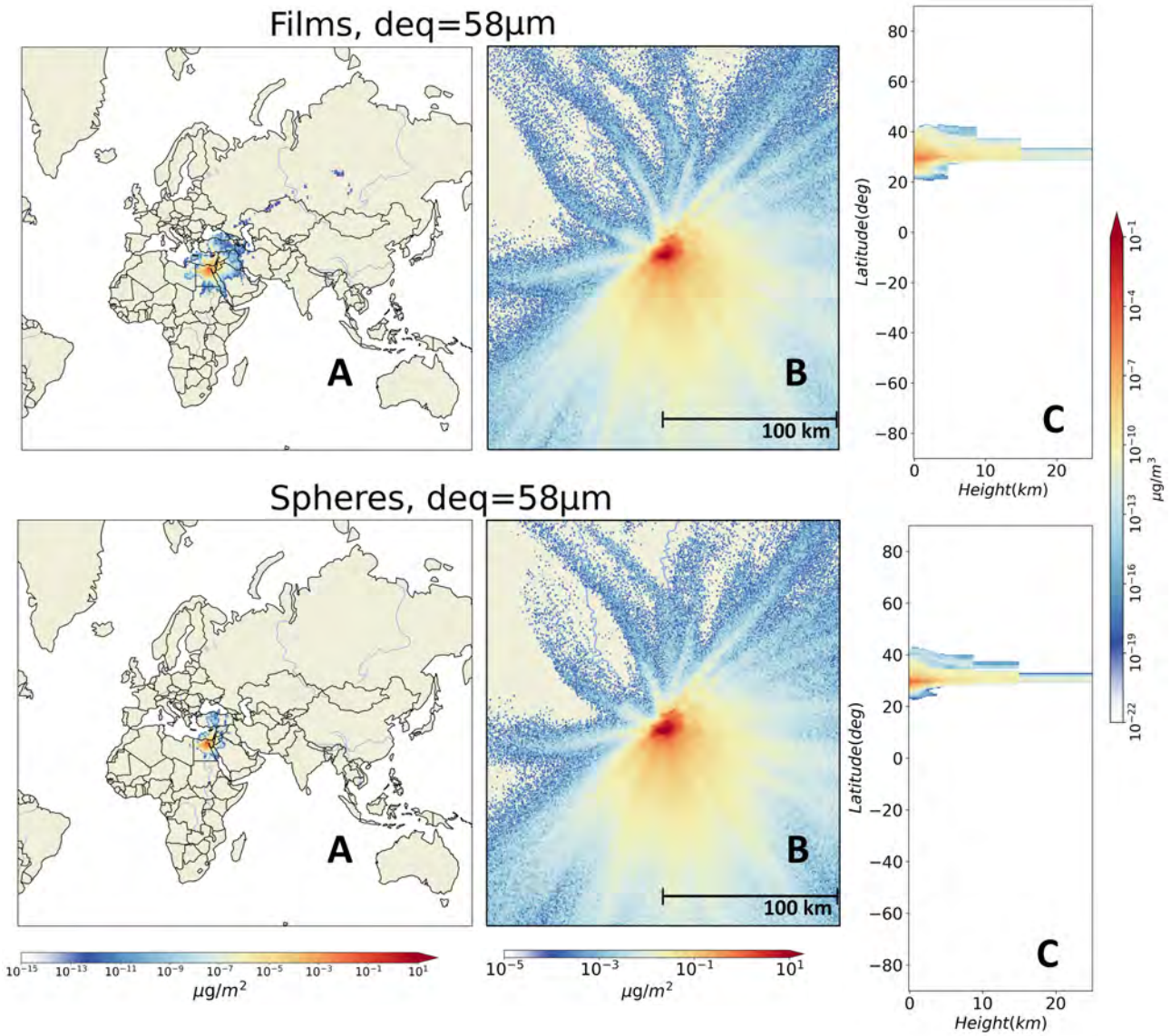

Figure 3.14.: (A) Daily dry and wet deposition of films and spheres with $d_{eq} = 58$ µm, released in Cairo. (B) Daily dry and wet deposition in the nested grid around the release point Cairo. (C) Zonal mean atmospheric mass concentration as a function of latitude and altitude.

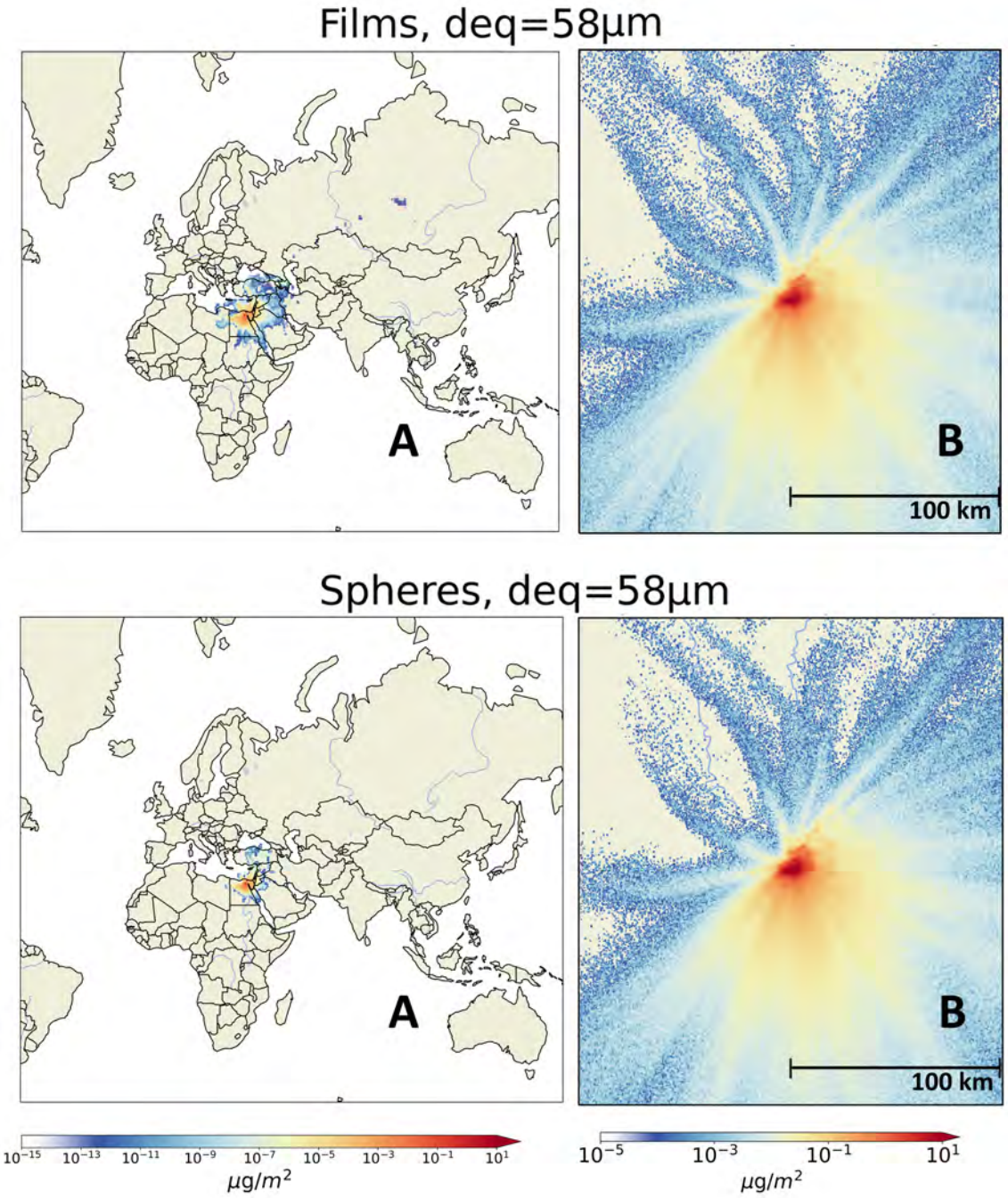

Figure 3.15.: (A) Daily dry deposition of films and spheres with d_{eq} = 58 µm, released in Cairo. (B) Daily dry deposition in the nested grid around the release point Cairo.

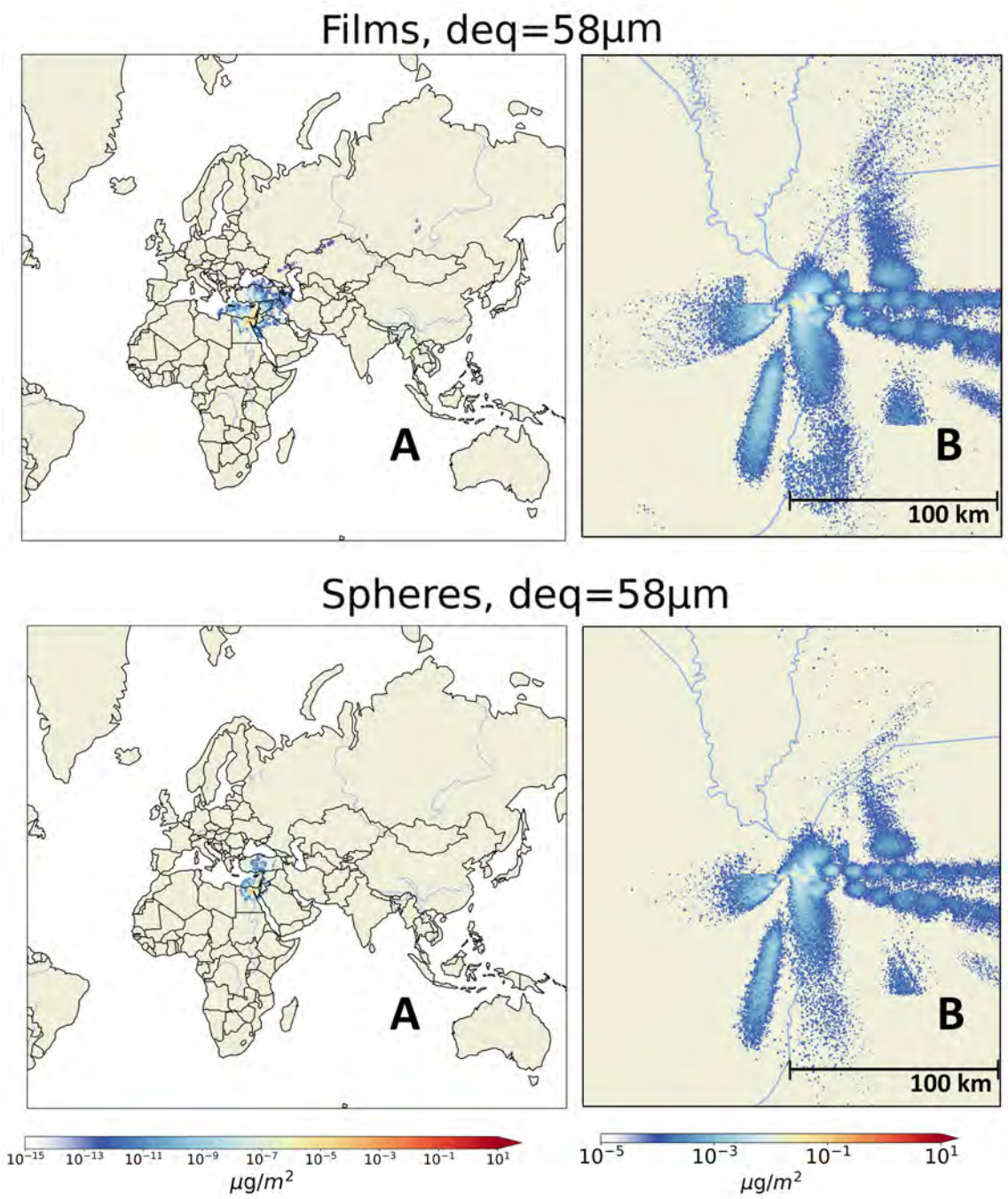

Figure 3.16.: (A) Daily wet deposition of films and spheres with d_{eq} = 58 µm, released in Cairo. (B) Daily wet deposition in the nested grid around the release point Cairo.

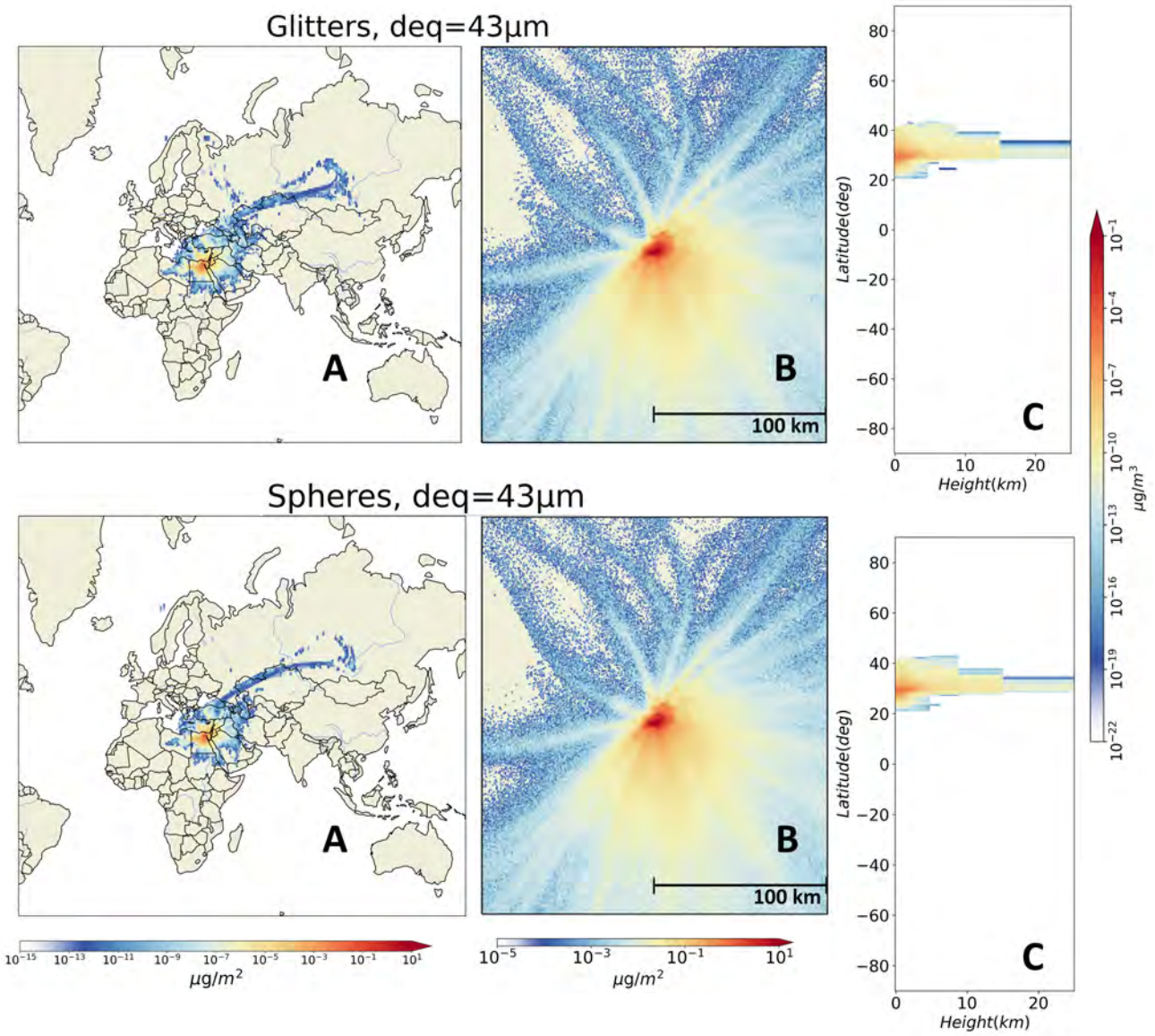

Figure 3.17.: (A) Daily dry and wet deposition of glitters and spheres with d_{eq} = 43 µm, released in Cairo. (B) Daily dry and wet deposition in the nested grid around the release point Cairo. (C) Zonal mean atmospheric mass concentration as a function of latitude and altitude.

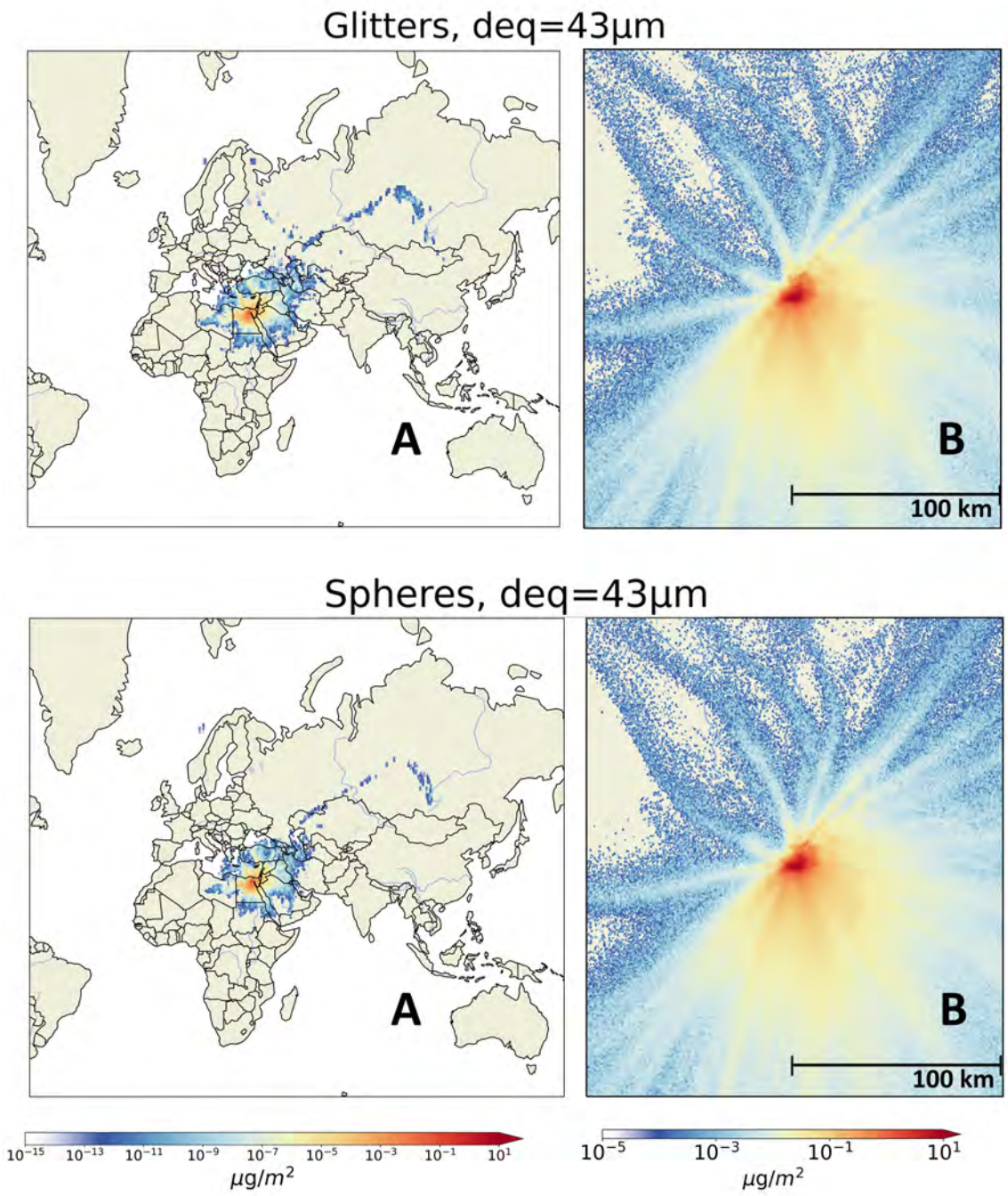

Figure 3.18.: (A) Daily dry deposition of glitters and spheres with $d_{eq} = 43$ µm, released in Cairo. (B) Daily dry deposition in the nested grid around the release point Cairo.

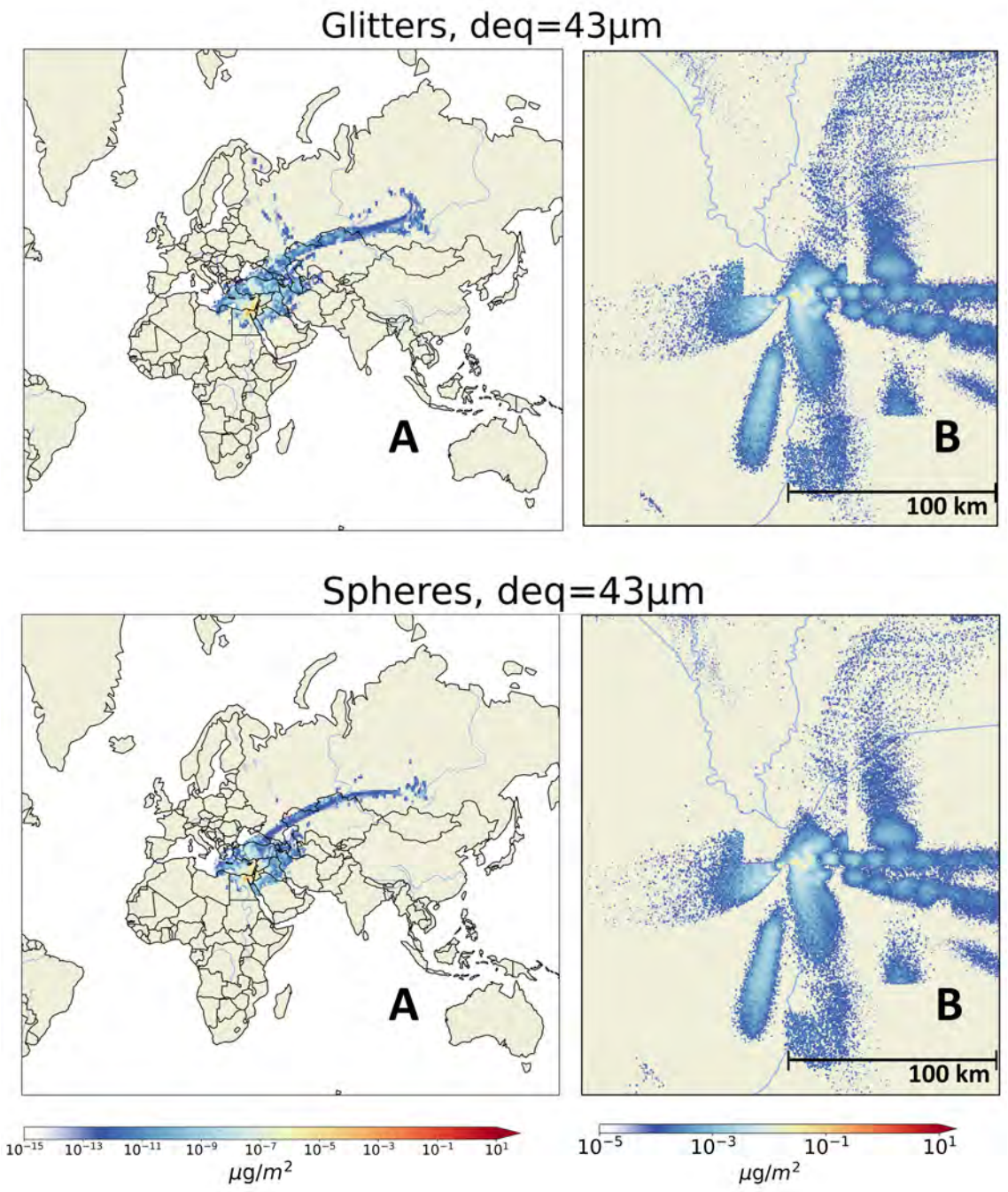

Figure 3.19.: (A) Daily wet deposition of glitters and spheres with d_{eq} = 43 µm, released in Cairo. (B) Daily wet deposition in the nested grid around the release point Cairo.

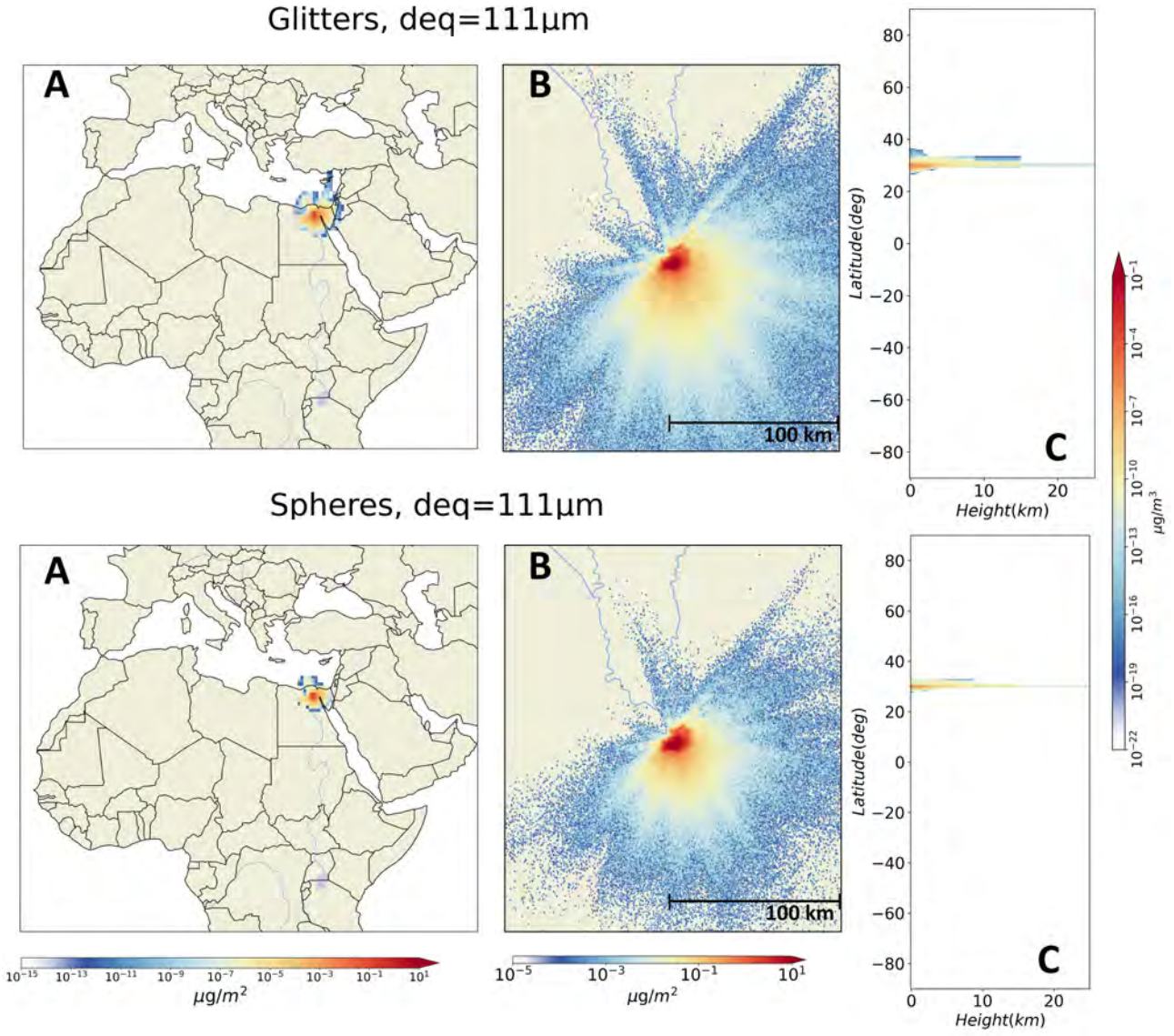

Figure 3.20.: (A) Daily dry and wet deposition of glitters and spheres with d_{eq} = 111 µm, released in Cairo. (B) Daily dry and wet deposition in the nested grid around the release point Cairo. (C) Zonal mean atmospheric mass concentration as a function of latitude and altitude.

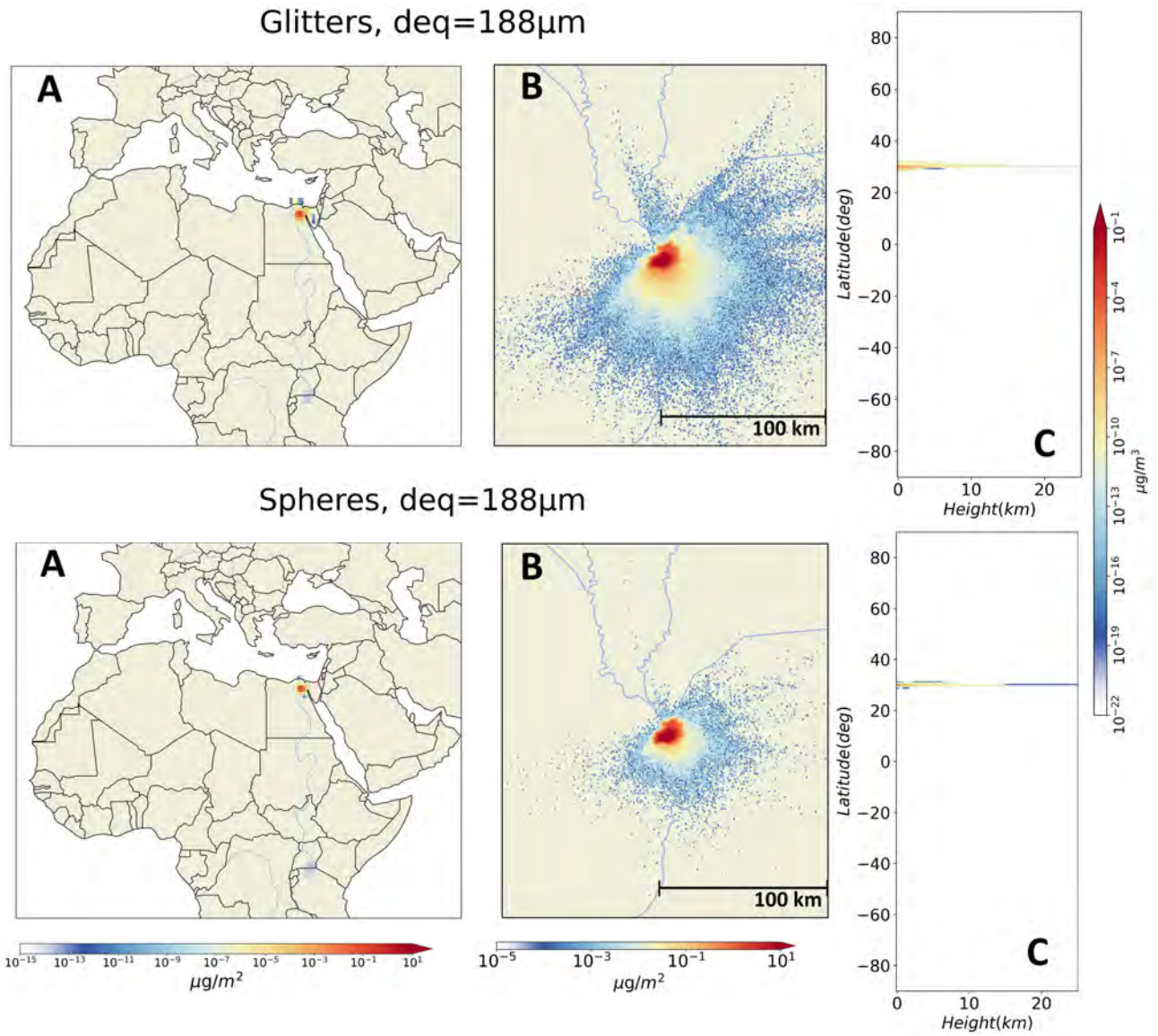

Figure 3.21.: (A) Daily dry and wet deposition of glitters and spheres with d_{eq} = 188 µm, released in Cairo. (B) Daily dry and wet deposition in the nested grid around the release point Cairo. (C) Zonal mean atmospheric mass concentration as a function of latitude and altitude.

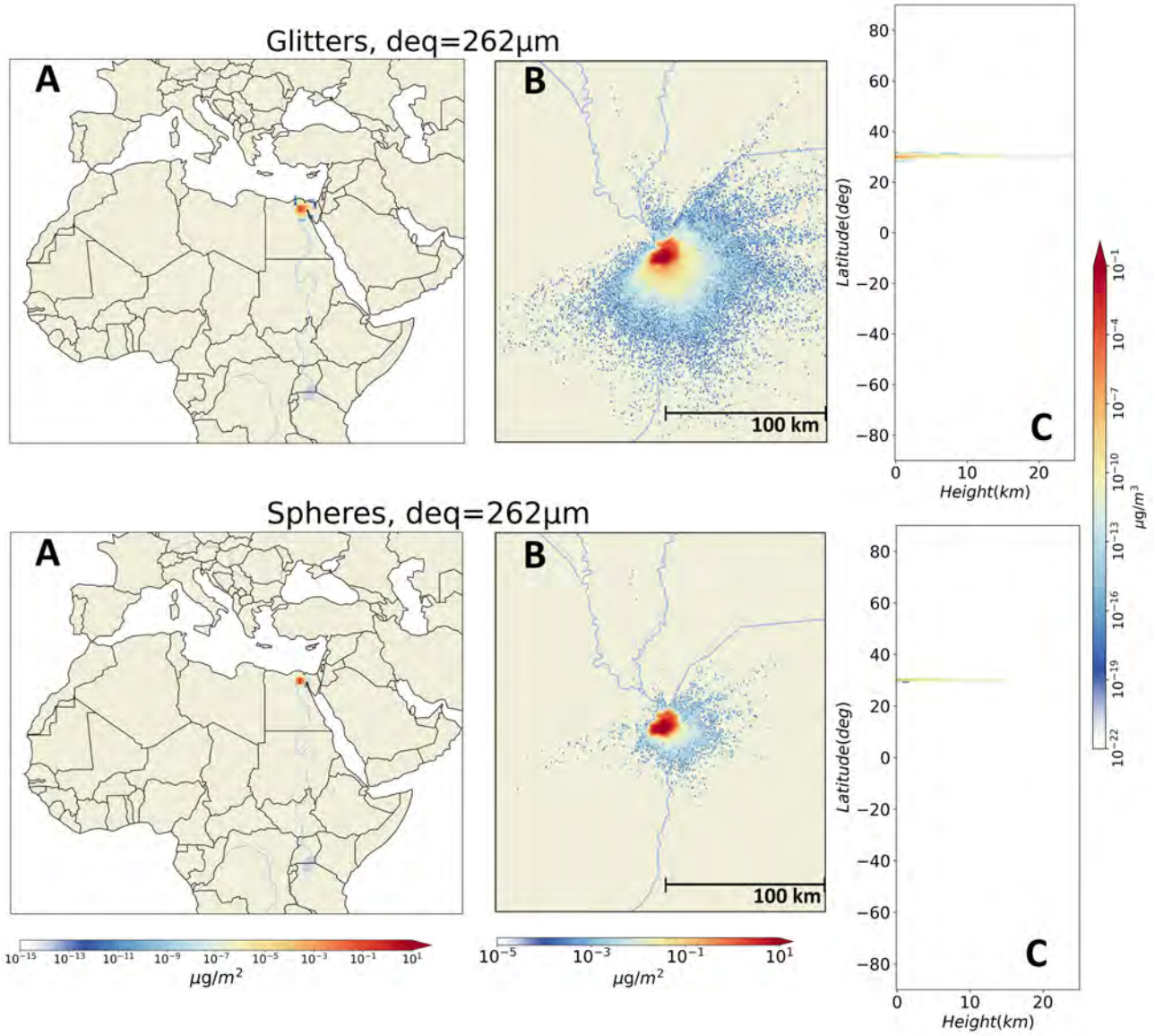

Figure 3.22.: (A) Daily dry and wet deposition of glitters and spheres with d_{eq} = 262 µm, released in Cairo. (B) Daily dry and wet deposition in the nested grid around the release point Cairo. (C) Zonal mean atmospheric mass concentration as a function of latitude and altitude.

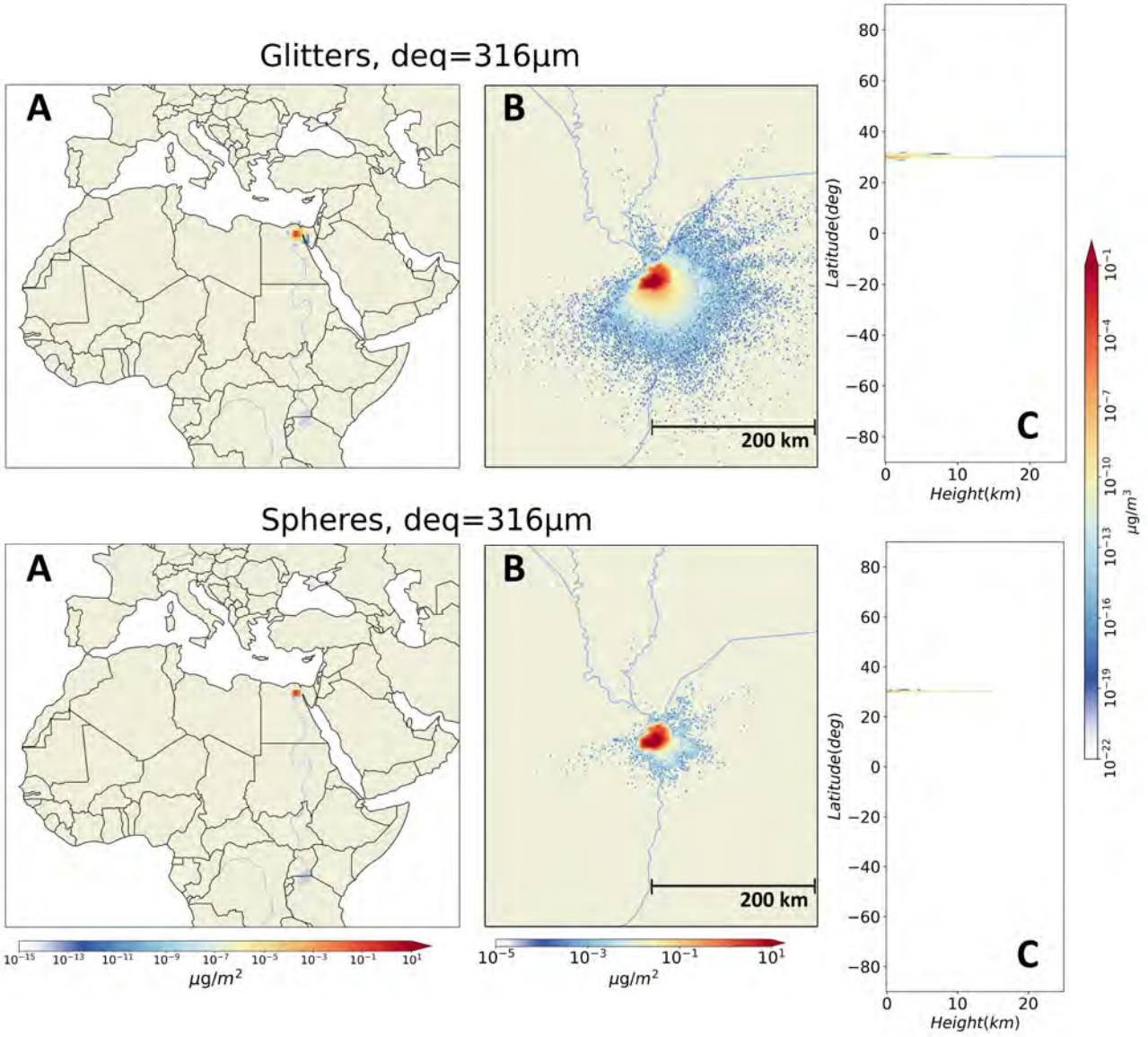

Figure 3.23.: (A) Daily dry and wet deposition of glitters and spheres with d_{eq} = 316 µm, released in Cairo. (B) Daily dry and wet deposition in the nested grid around the release point Cairo. (C) Zonal mean atmospheric mass concentration as a function of latitude and altitude.

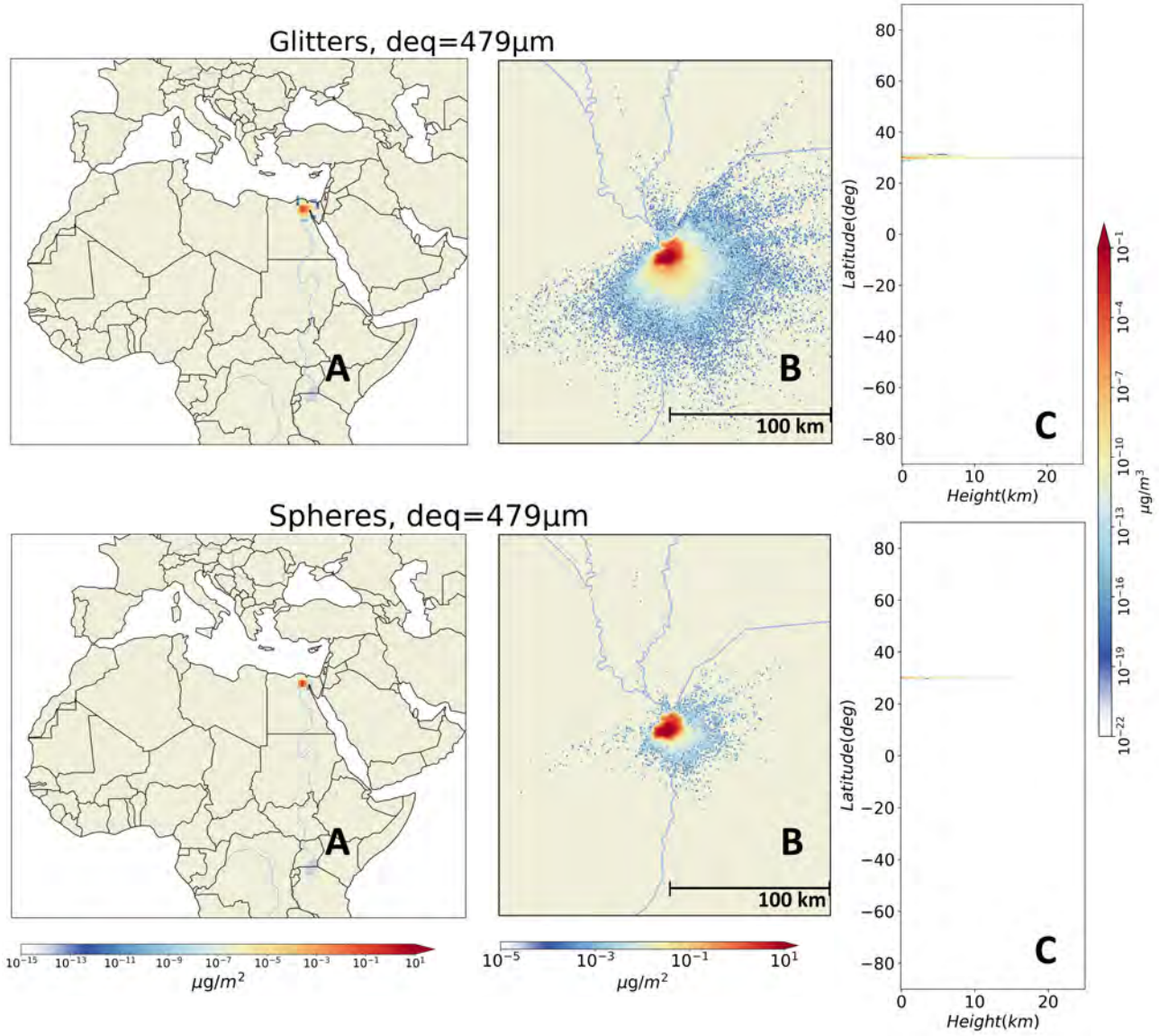

Figure 3.24.: (A) Daily dry and wet deposition of glitters and spheres with d_{eq} = 479 µm, released in Cairo. (B) Daily dry and wet deposition in the nested grid around the release point Cairo. (C) Zonal mean atmospheric mass concentration as a function of latitude and altitude.

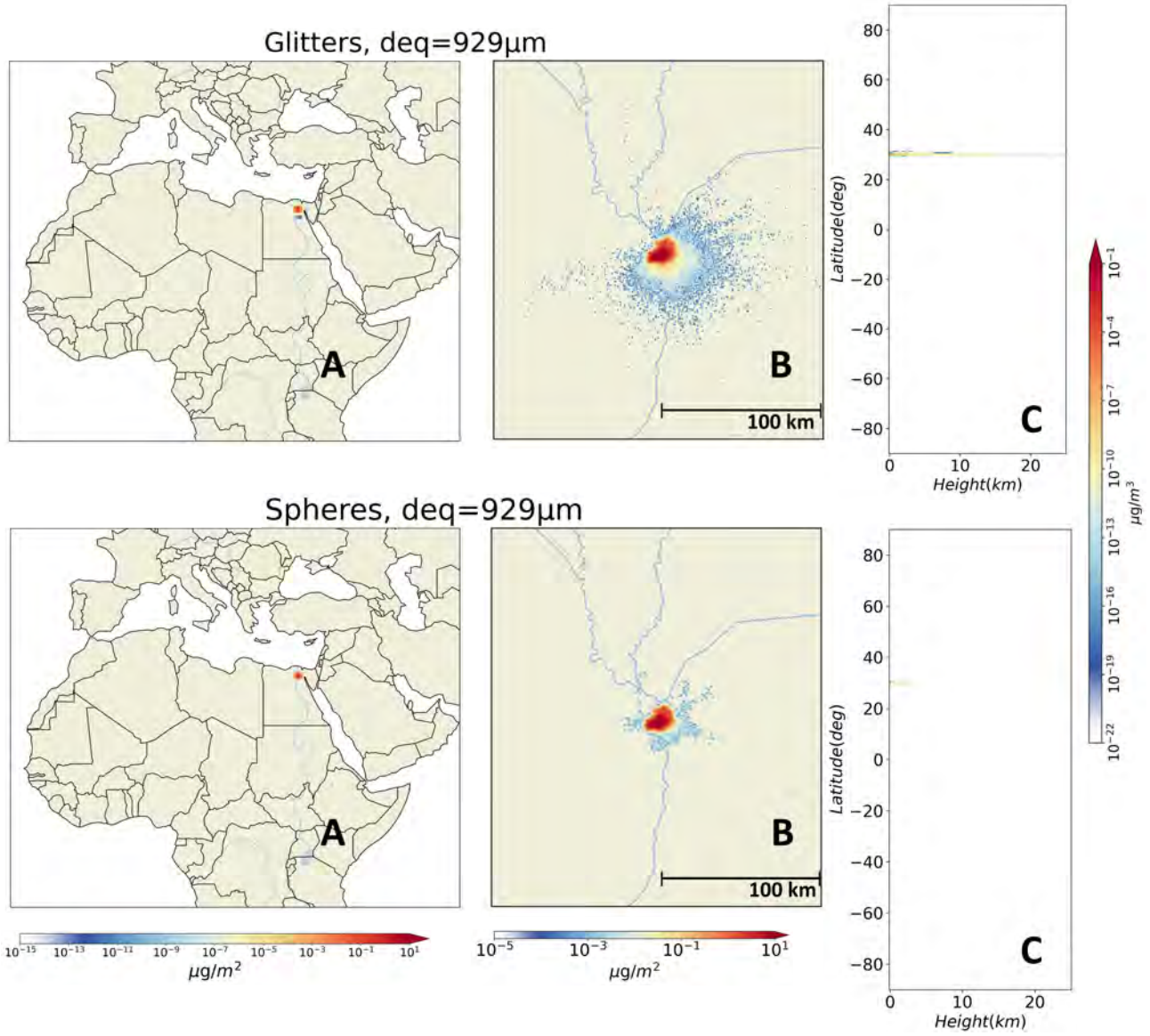

Figure 3.25.: (A) Daily dry and wet deposition of glitters and spheres with d_{eq} = 929 µm, released in Cairo. (B) Daily dry and wet deposition in the nested grid around the release point Cairo. (C) Zonal mean atmospheric mass concentration as a function of latitude and altitude.

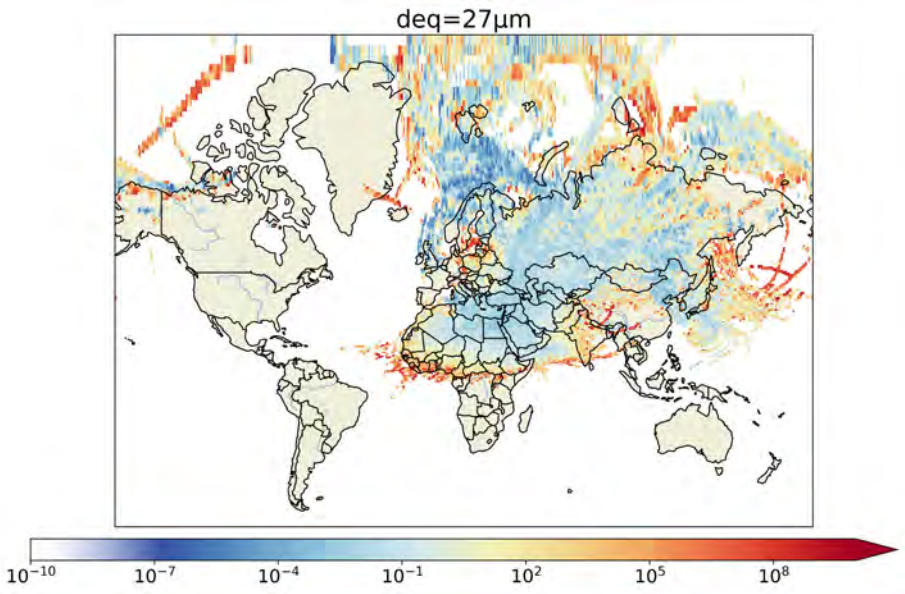

Figure 3.26.: Daily total deposition ratio of films and spheres with d_{eq} = 27 µm around the release point Cairo.

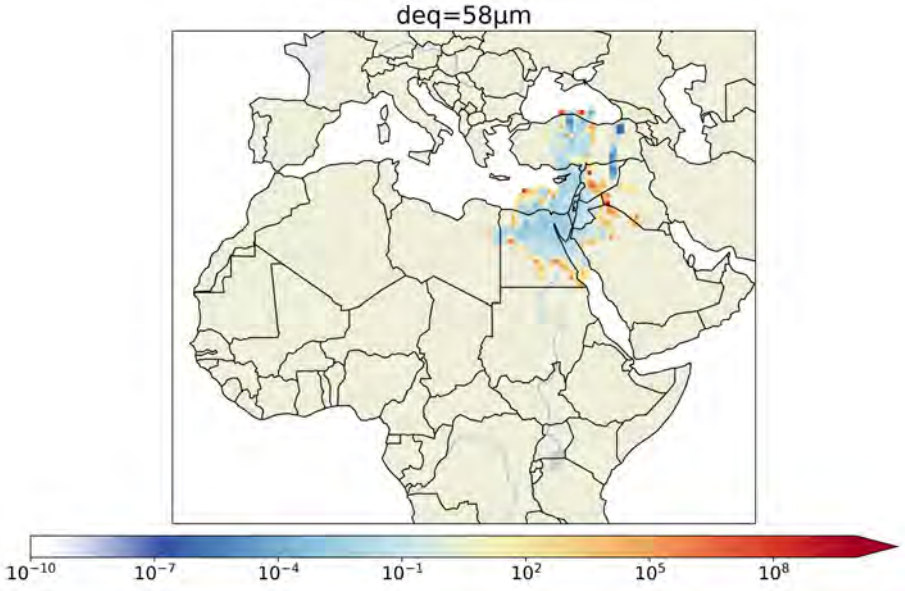

Figure 3.27.: Daily total deposition ratio of films and spheres with d_{eq} = 58 µm around the release point Cairo.

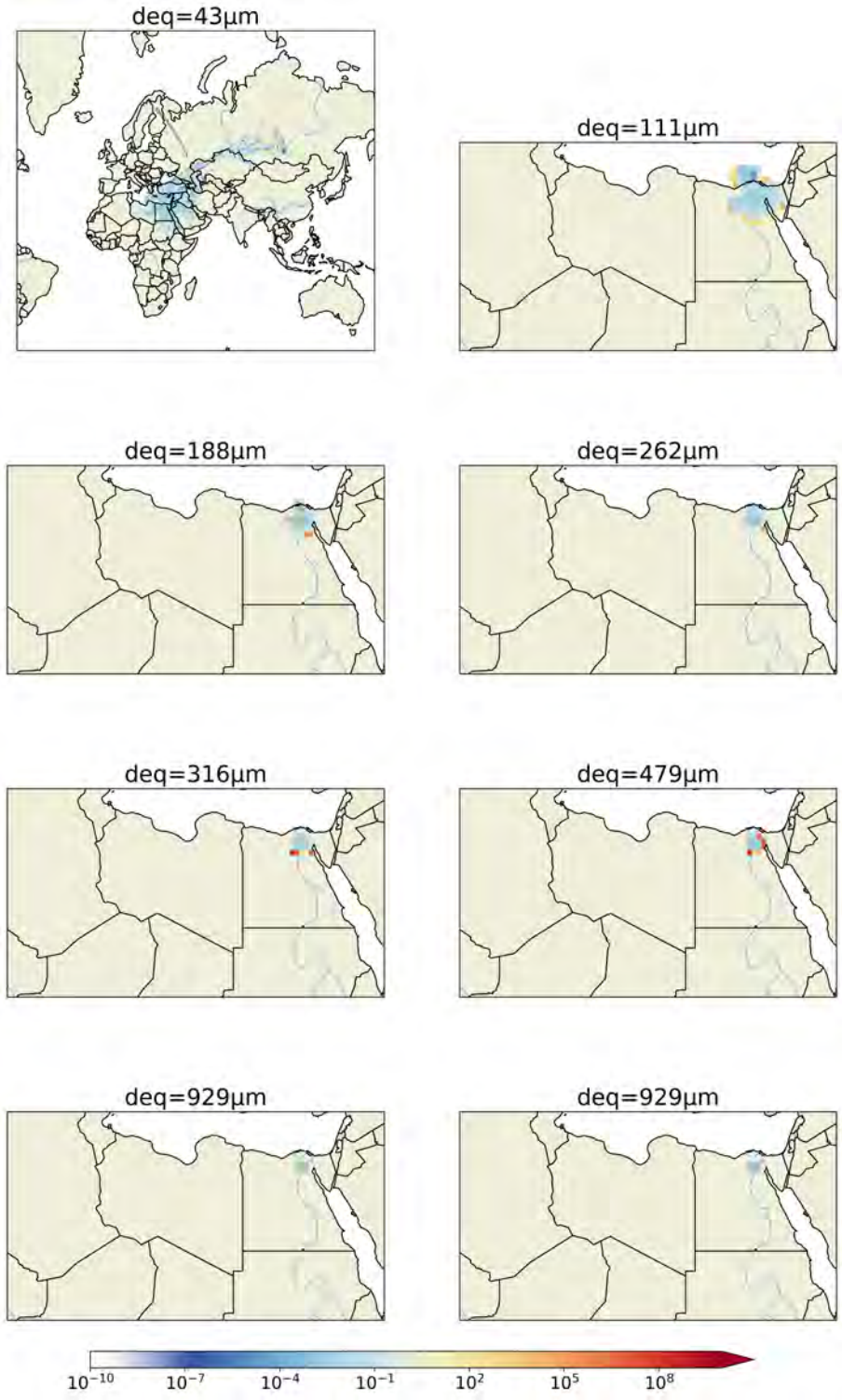

Figure 3.28.: Daily total deposition ratio of glitters and spheres around the release point Cairo.

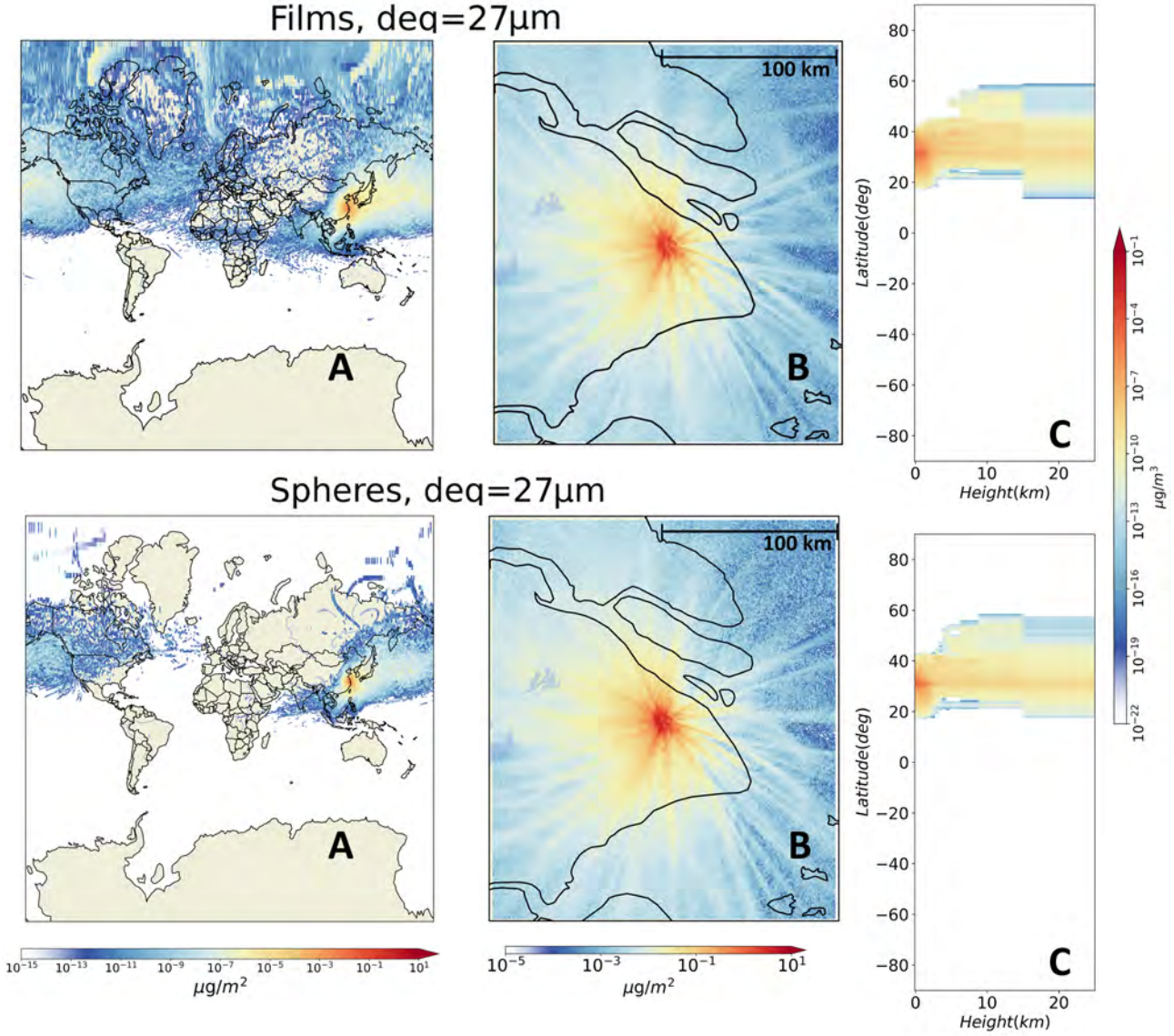

Figure 3.29.: (A) Daily dry and wet deposition of films and spheres with d_{eq} = 27 µm, released in Shanghai. (B) Daily dry and wet deposition in the nested grid around the release point Shanghai. (C) Zonal mean atmospheric mass concentration as a function of latitude and altitude.

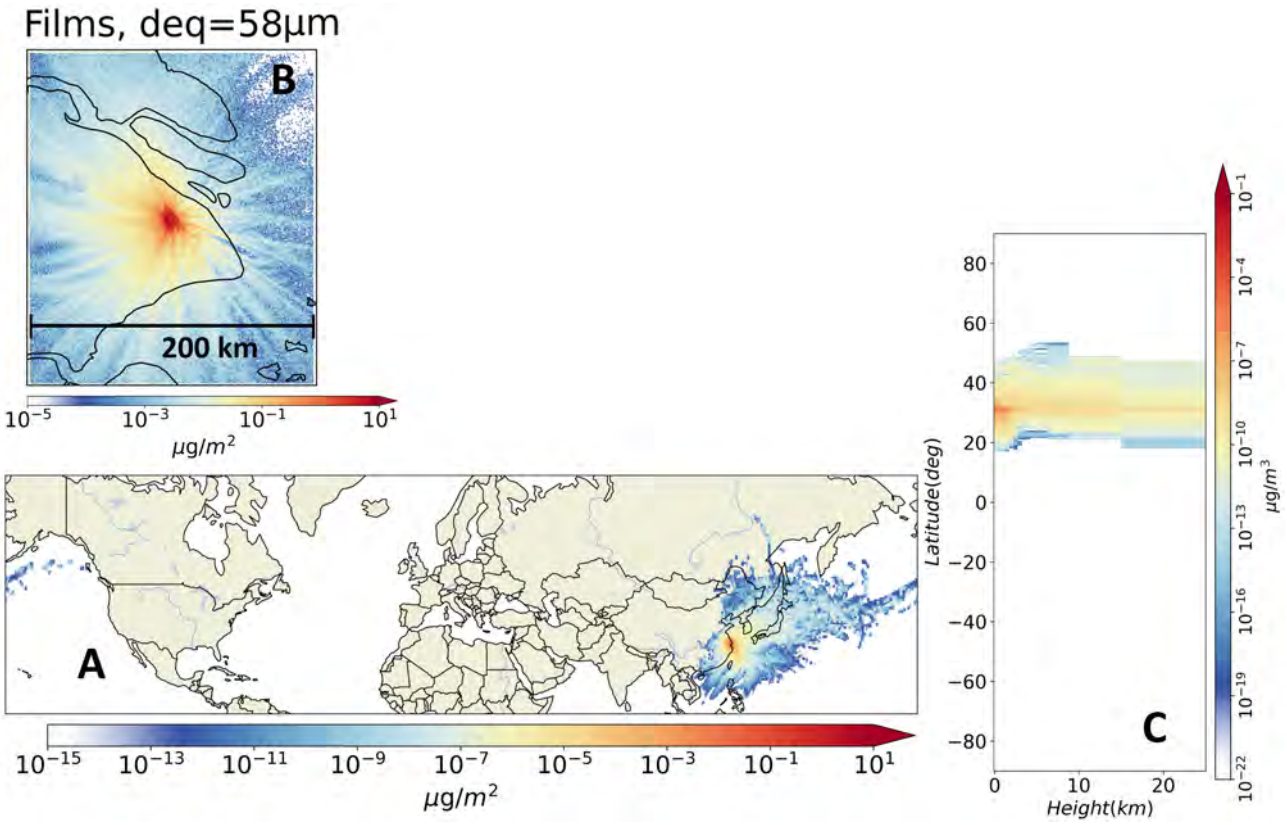

Figure 3.30.: (A) Daily dry and wet deposition of films with d_{eq} = 58 µm, released in Shanghai. (B) Daily dry and wet deposition in the nested grid around the release point Shanghai. (C) Zonal mean atmospheric mass concentration as a function of latitude and altitude.

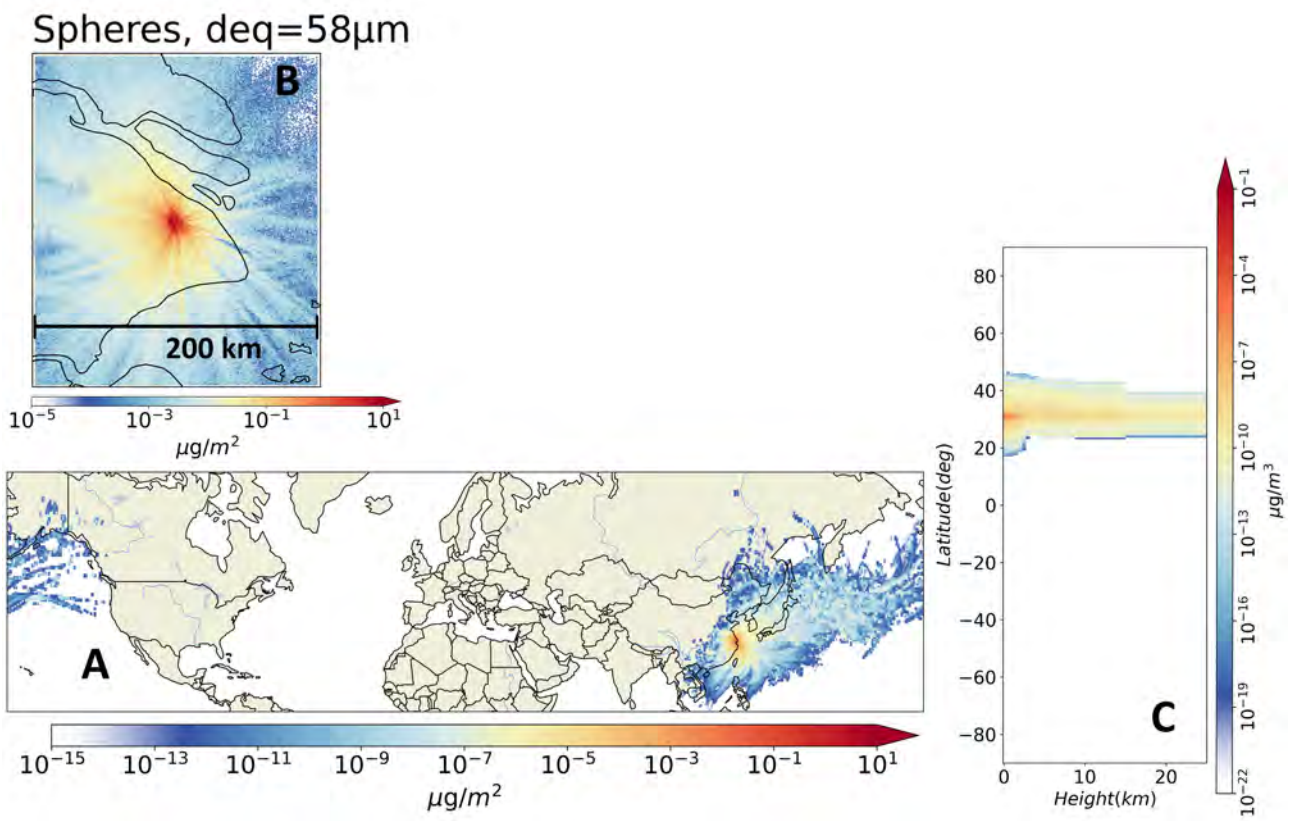

Figure 3.31.: (A) Daily dry and wet deposition of films and spheres with d_{eq} = 27 µm, released in Shanghai. (B) Daily dry and wet deposition in the nested grid around the release point Shanghai. (C) Zonal mean atmospheric mass concentration as a function of latitude and altitude.

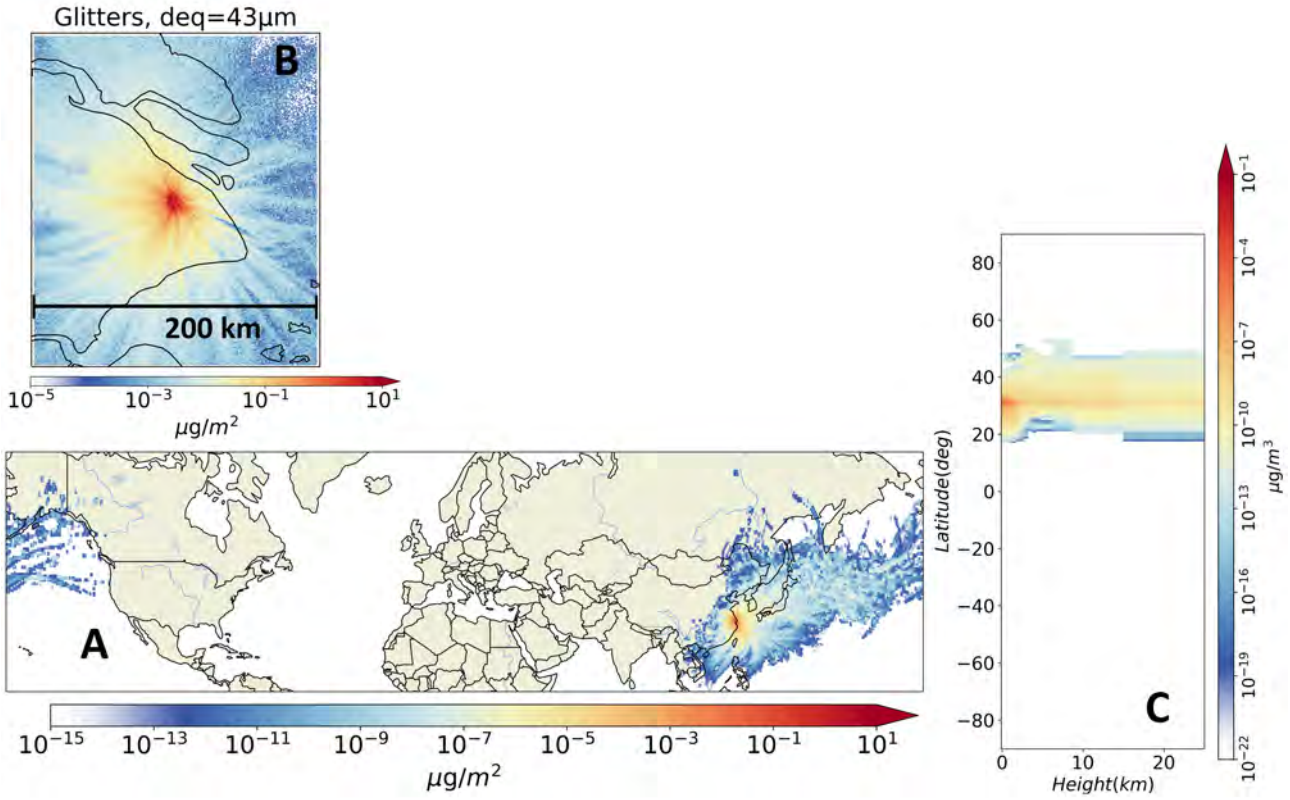

Figure 3.32.: (A) Daily dry and wet deposition of glitters with d_{eq} = 43 µm, released in Shanghai. (B) Daily dry and wet deposition in the nested grid around the release point Shanghai. (C) Zonal mean atmospheric mass concentration as a function of latitude and altitude.

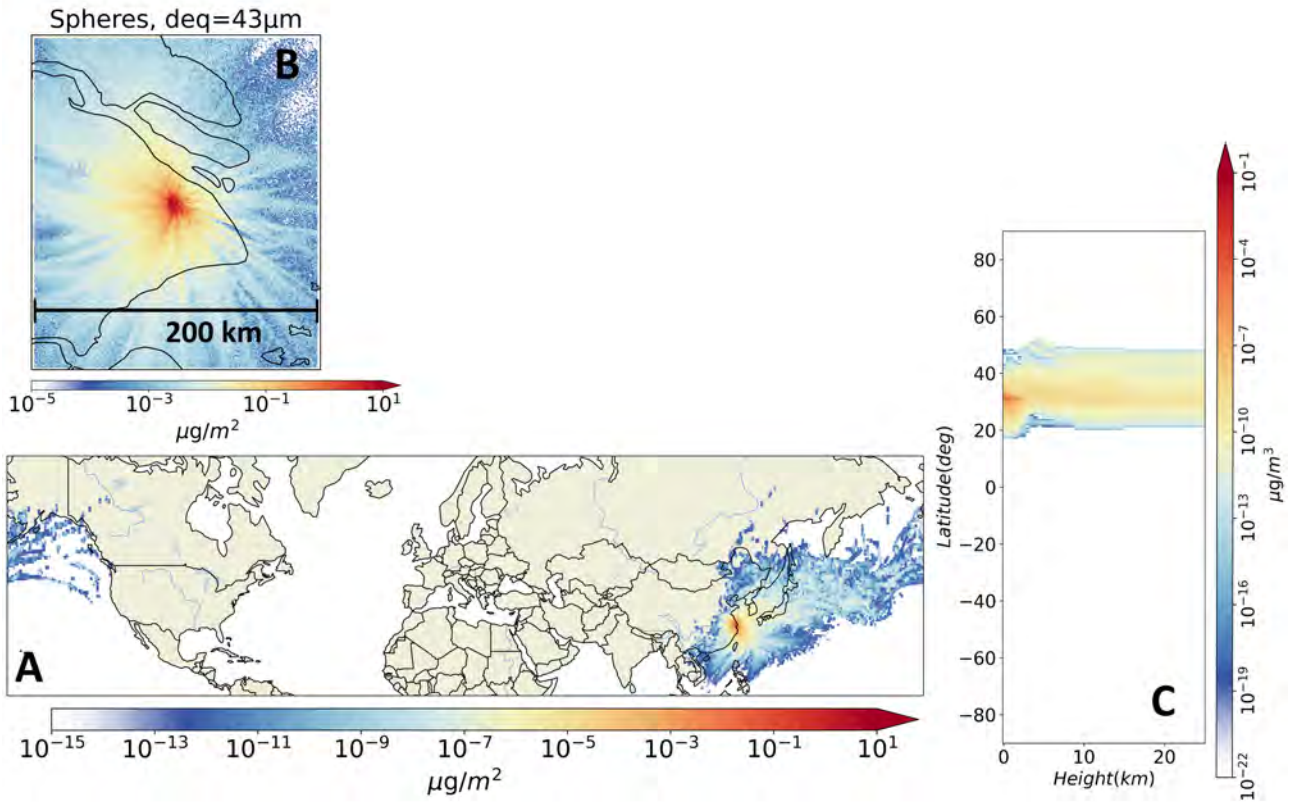

Figure 3.33.: (A) Daily dry and wet deposition of spheres with d_{eq} = 43 µm, released in Shanghai. (B) Daily dry and wet deposition in the nested grid around the release point Shanghai.

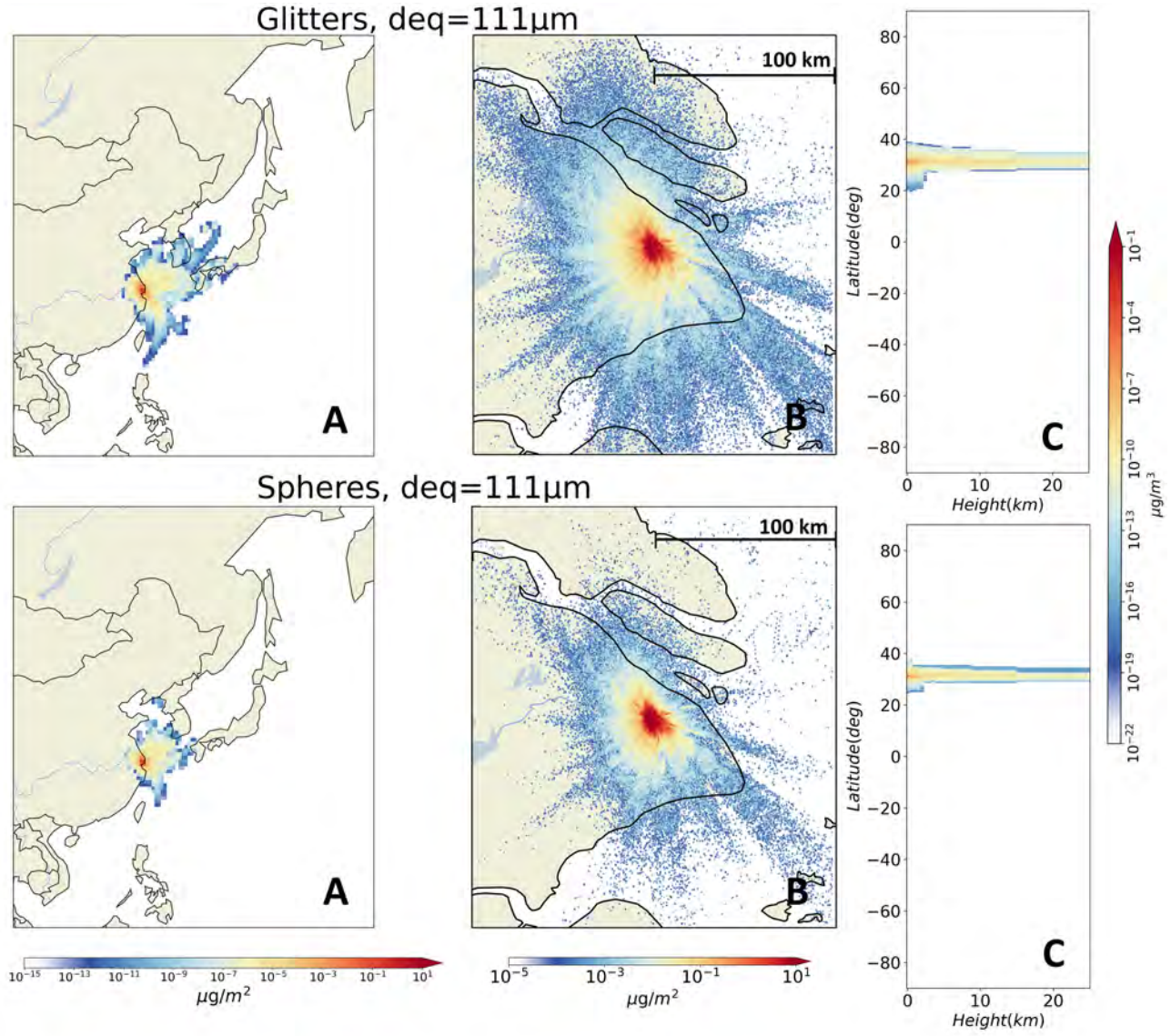

Figure 3.34.: (A) Daily dry and wet deposition of glitters and spheres with d_{eq} = 111 µm, released in Shanghai. (B) Daily dry and wet deposition in the nested grid around the release point Shanghai. (C) Zonal mean atmospheric mass concentration as a function of latitude and altitude.

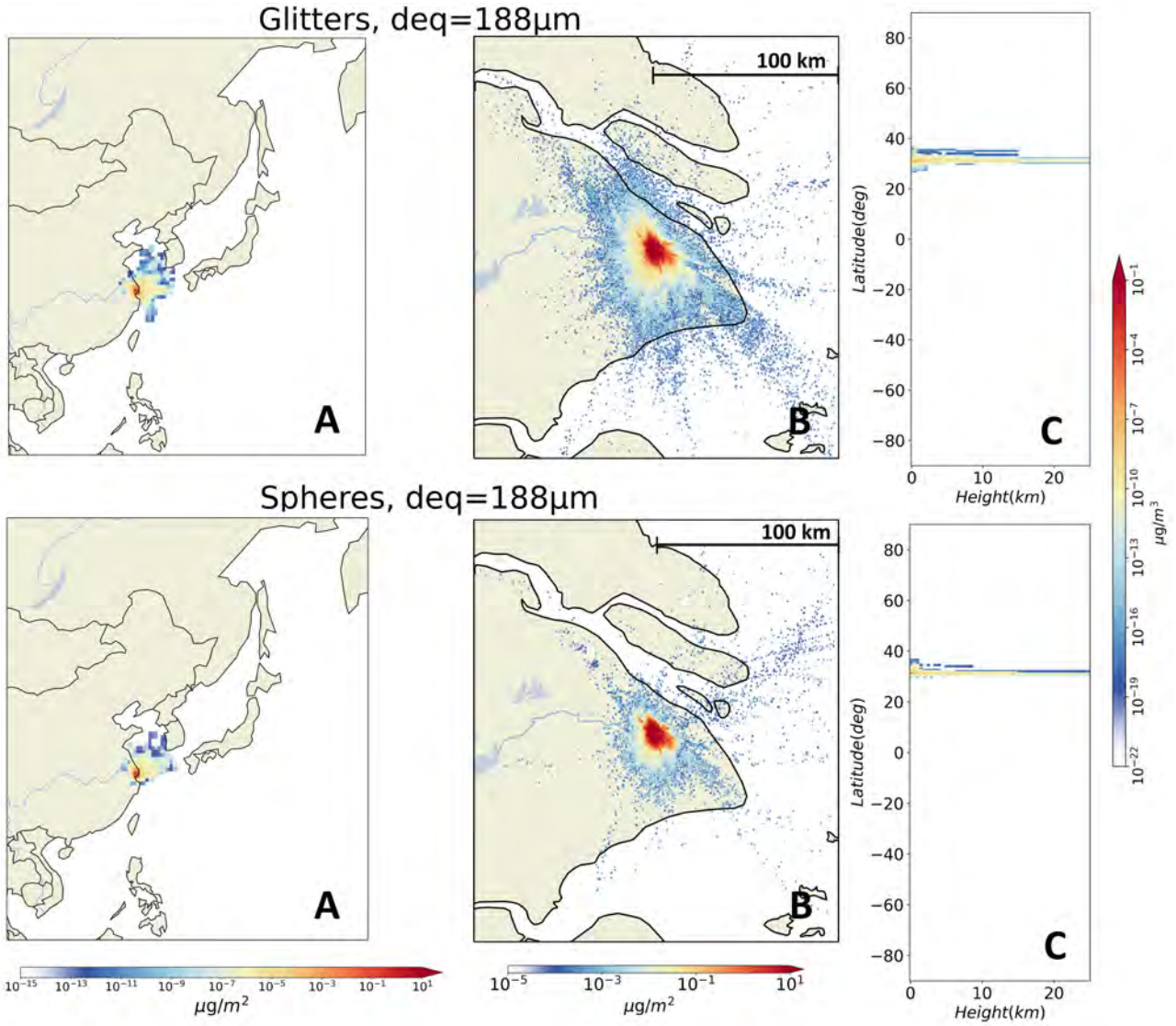

Figure 3.35.: (A) Daily dry and wet deposition of glitters and spheres with d_{eq} = 188 µm, released in Shanghai. (B) Daily dry and wet deposition in the nested grid around the release point Shanghai. (C) Zonal mean atmospheric mass concentration as a function of latitude and altitude.

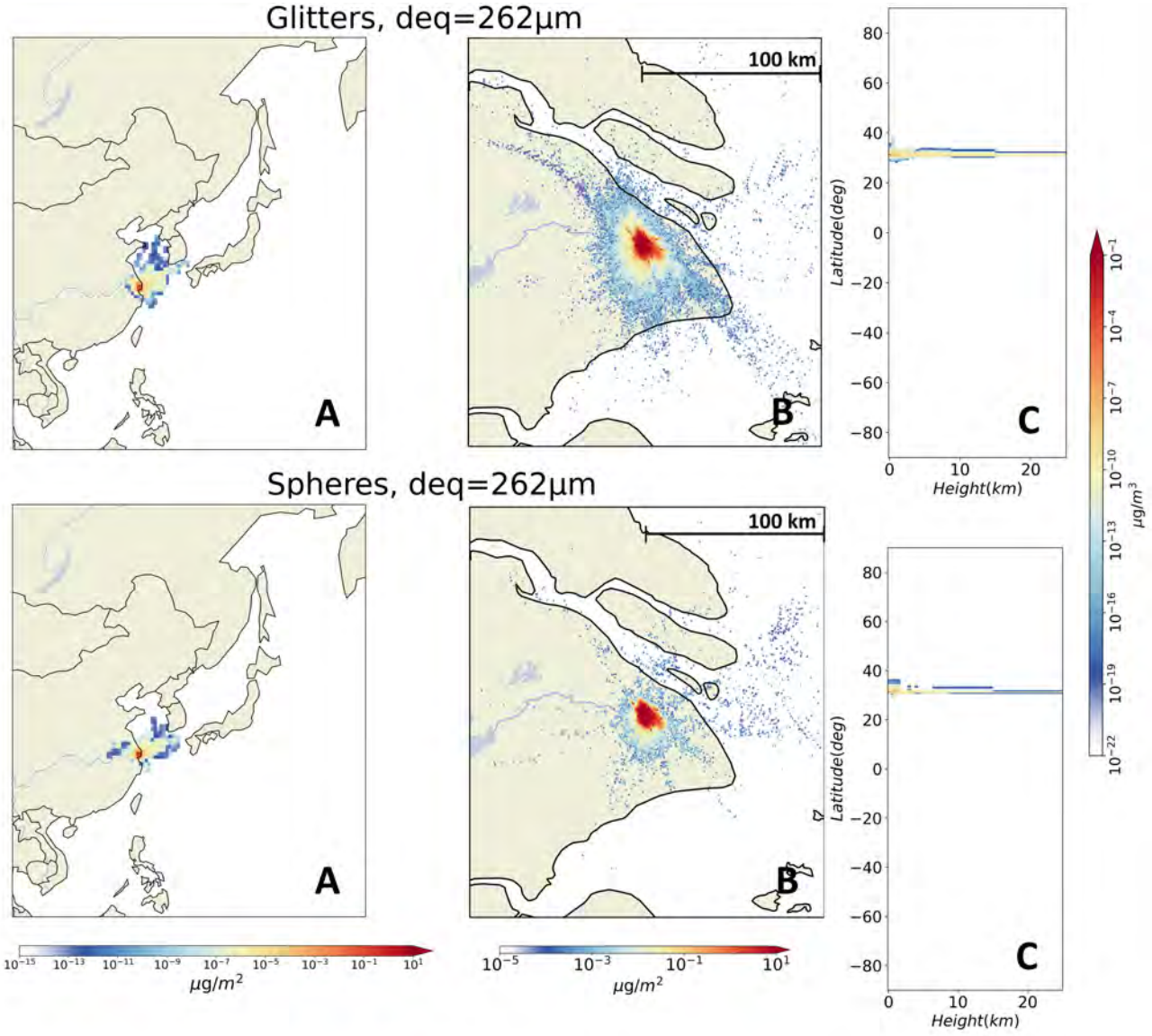

Figure 3.36.: (A) Daily dry and wet deposition of glitters and spheres with d_{eq} = 262 µm, released in Shanghai. (B) Daily dry and wet deposition in the nested grid around the release point Shanghai. (C) Zonal mean atmospheric mass concentration as a function of latitude and altitude.

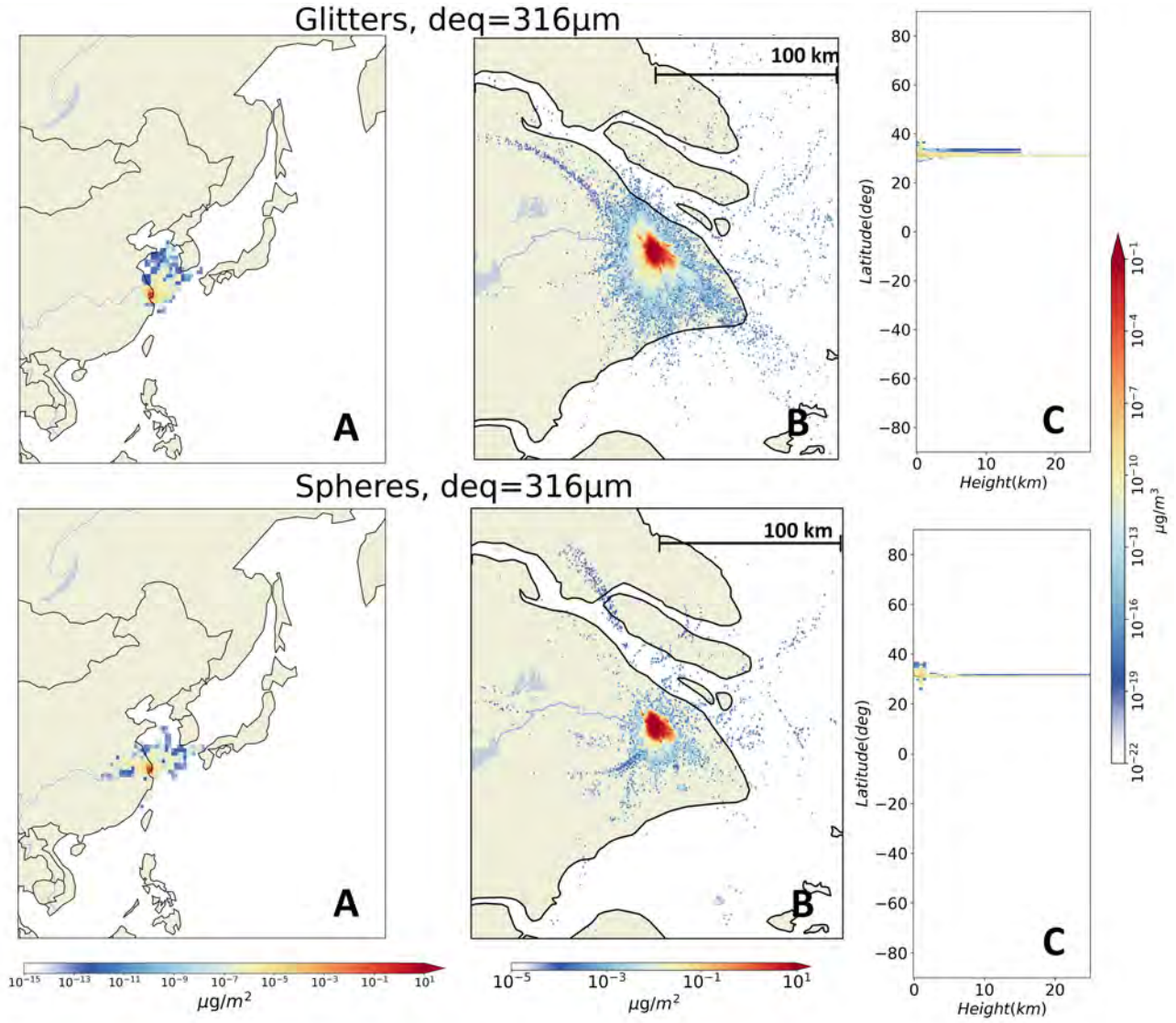

Figure 3.37.: (A) Daily dry and wet deposition of glitters and spheres with d_{eq} = 316 µm, released in Shanghai. (B) Daily dry and wet deposition in the nested grid around the release point Shanghai. (C) Zonal mean atmospheric mass concentration as a function of latitude and altitude.

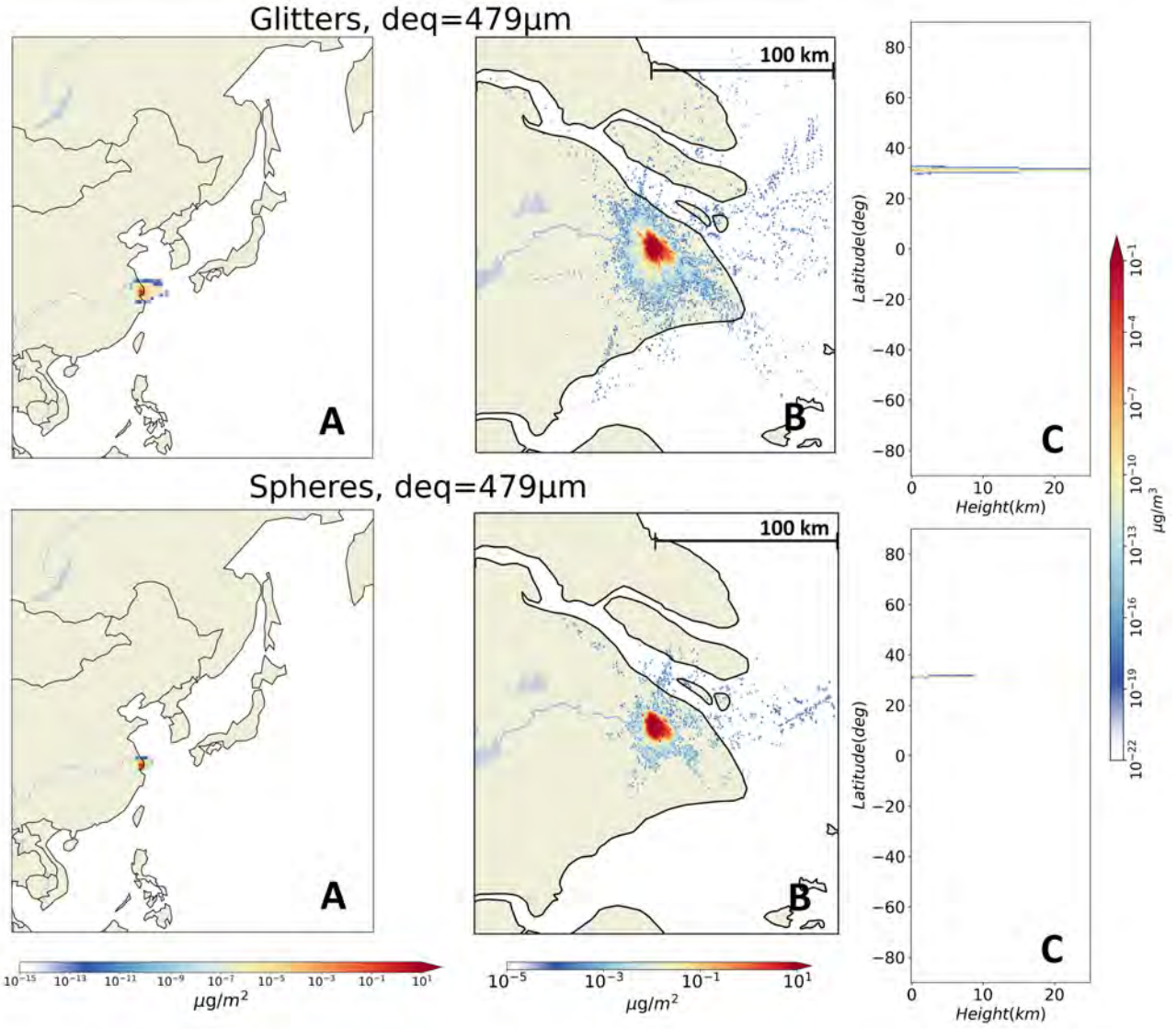

Figure 3.38.: (A) Daily dry and wet deposition of glitters and spheres with d_{eq} = 479 µm, released in Shanghai. (B) Daily dry and wet deposition in the nested grid around the release point Shanghai. (C) Zonal mean atmospheric mass concentration as a function of latitude and altitude.

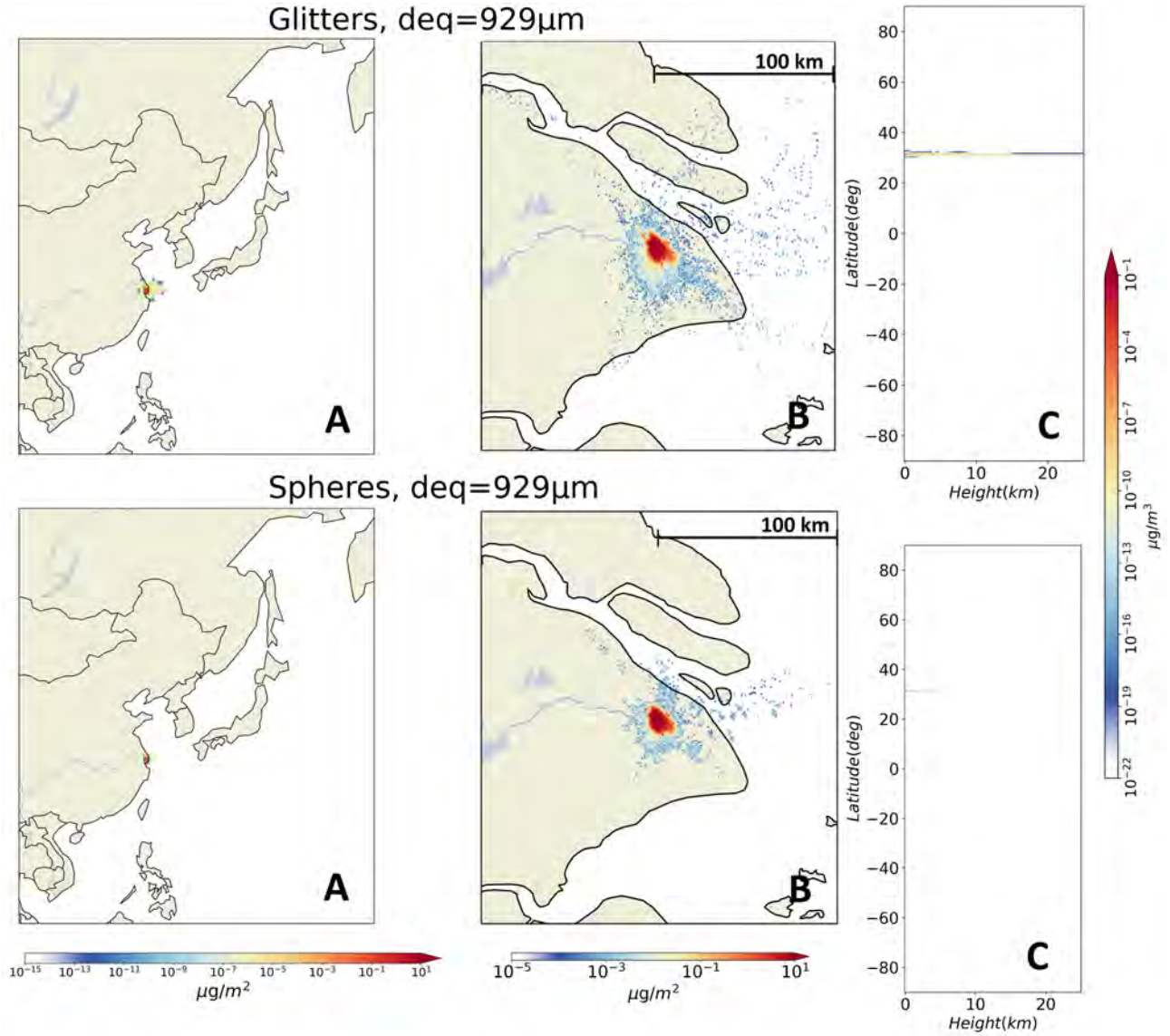

Figure 3.39.: (A) Daily dry and wet deposition of glitters and spheres with d_{eq} = 929 µm, released in Shanghai. (B) Daily dry and wet deposition in the nested grid around the release point Shanghai. (C) Zonal mean atmospheric mass concentration as a function of latitude and altitude.

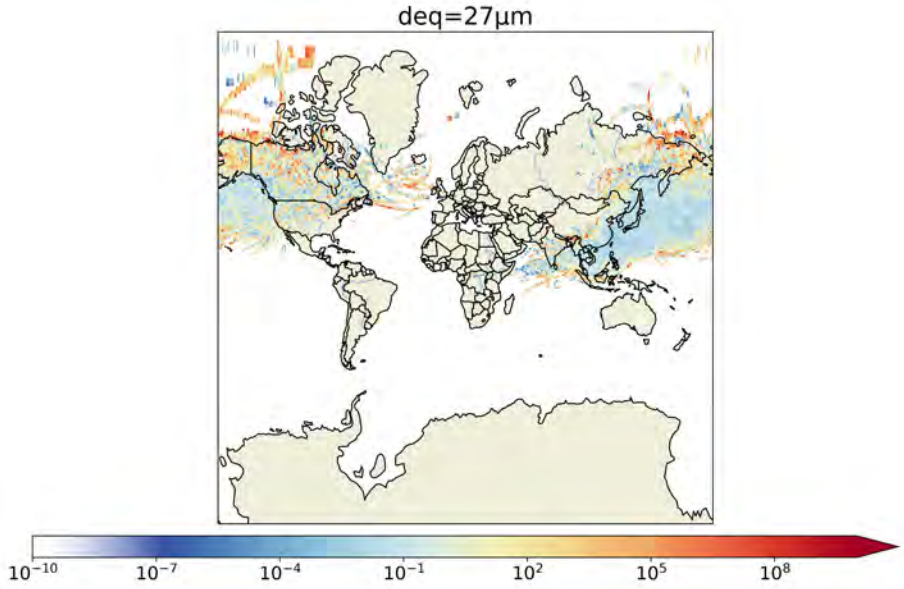

Figure 3.40.: Daily total deposition ratio of films and spheres with d_{eq} = 27 µm around the release point Shanghai.

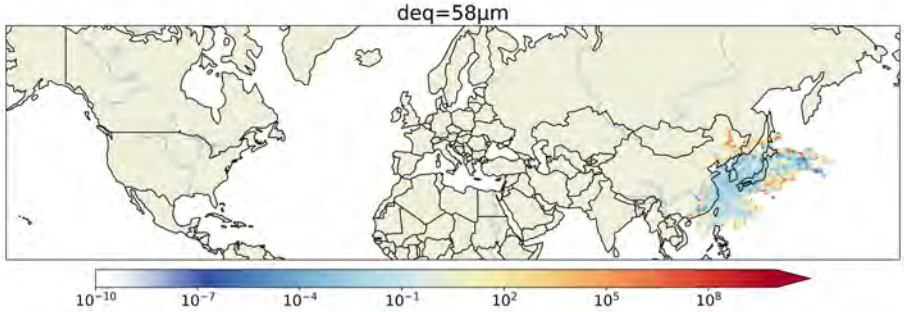

Figure 3.41.: Daily total deposition ratio of films and spheres with d_{eq} = 58 µm around the release point Shanghai.

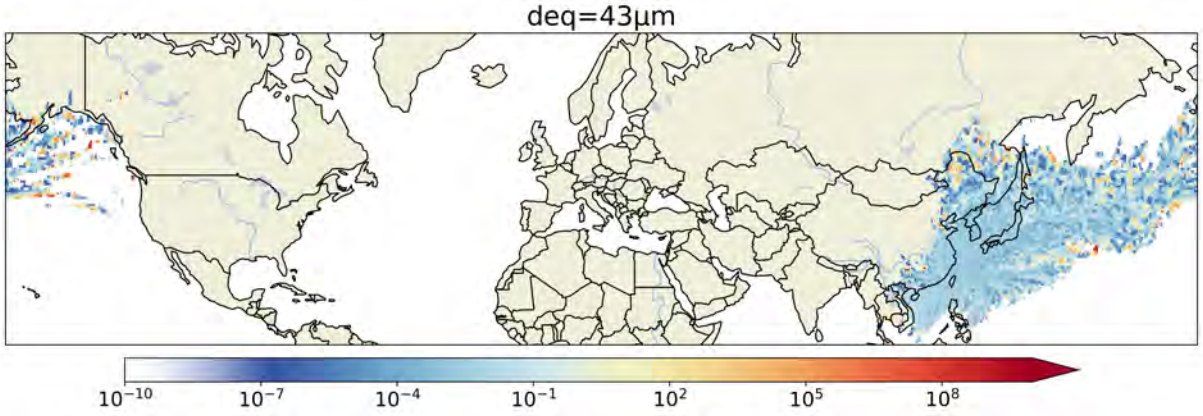

Figure 3.42.: Daily total deposition ratio of glitters and spheres with $d_{eq} = 43$ µm around the release point Shanghai.

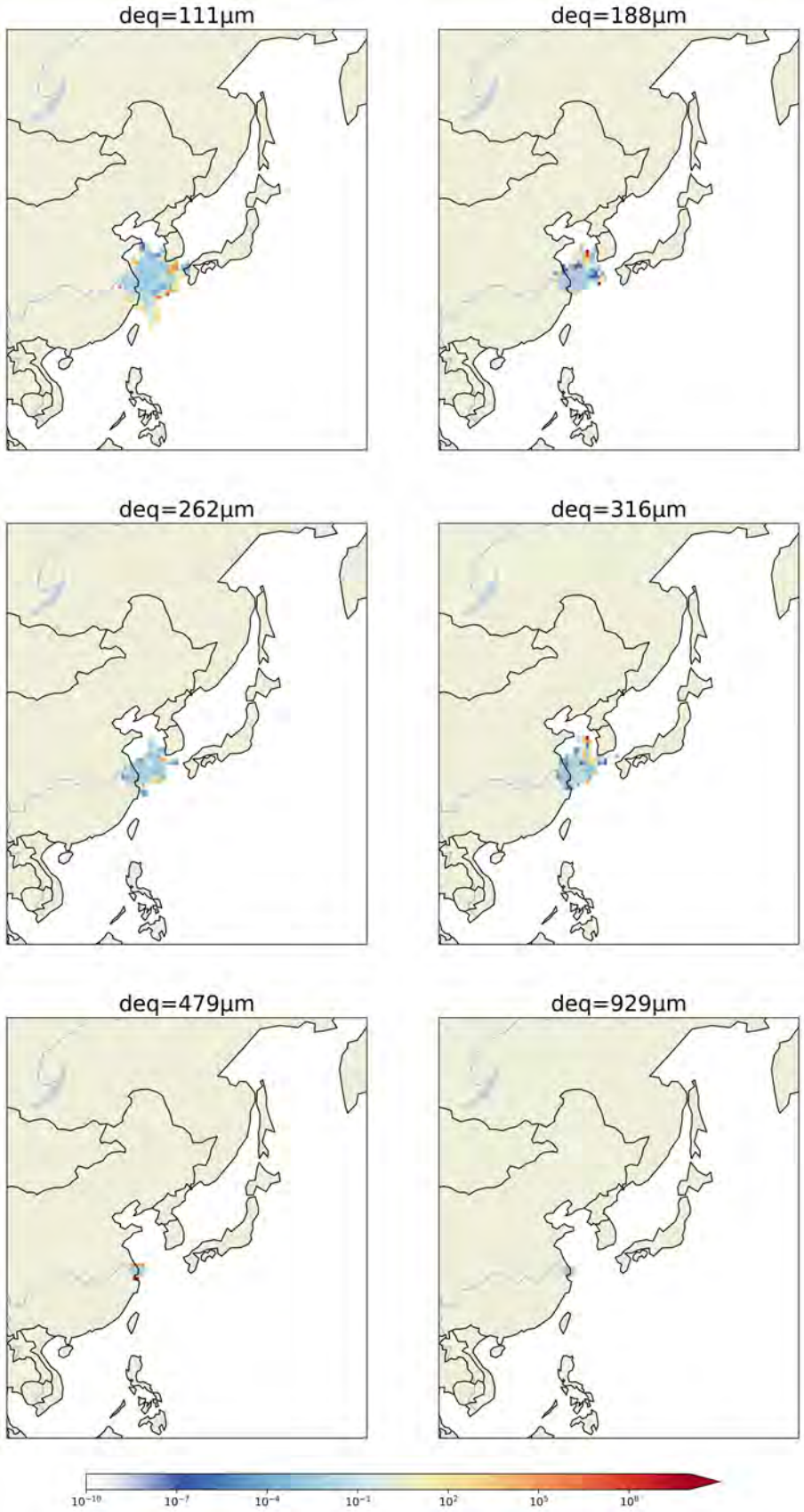

Figure 3.43.: Daily total deposition ratio of glitters and spheres around the release point Shanghai.

4. Conclusion

Microplastics are a major environmental threat and have been detected in diverse environmental compartments. However, there is still a lack of information on the transport and abundance of microplastics in the atmosphere. Due to their often complex shapes, airborne microplastics can experience lower settling velocities than volume-equivalent spheres. This in turn leads to longer atmospheric transport compared to spheres and the deposition in remote regions around the globe. The impact of the particle's shape on it's atmospheric transport behavior needs further investigation, as the atmospheric transport of fibers have already been studied, but information on film-like particles is lacking. Here, atmospheric transport simulations were performed using FLEXPART to study the transport of microplastic films in the global atmosphere. For the simulations, the shape-correction scheme of Bagheri and Bonadonna [2016] was used. To represent microplastic films, seven sizes of commercially sold craft glitter particles and two films (100 µm × 100 µm × 1 µm and 100 µm × 100 µm × 10 µm) were released during the simulations in five cities, representing different climate regions. For these particles, mean atmospheric transport distances, residence times, and global deposition patterns were evaluated. The results were compared to those of volume-equivalent spheres to study the impact of particle shape. This was done to to get a better understanding of the atmospheric transport of microplastic films and to investigate how far glitter released during festivities, for example, can be transported in the atmosphere.

Average atmospheric transport distances of the particles used in the simulations tend to decrease with increasing particle size. Square, thin films with d_{eq} = 27 µm are transported the furthest; their mean atmospheric transport distance is 245.33 km. Glitter particles with d_{eq} = 43 µm have mean atmospheric transport distances of 52.37 km, followed by films with d_{eq} = 58 µm, with average transport distances of 42.94 km. Glitters with equivalent diameters of 111 µm have mean atmospheric transport distances of 18.08 km. The mean atmospheric transport distances of glitters with d_{eq} = 188, 262, 316, 479, and 929 µm are remarkably similar, namely 13.99, 13.48, 13.33, 13.10, and 12.93 km.

It is shown that airborne glitter particles are not transported substantially further than spheres of the same volume. The mean atmospheric transport distances of glitters are between 2.5 % and 20.5 % greater than those of spheres. This is not the case for the 27 µm and 58 µm diameter films, which are much thinner than commercially available glitter and travel round 123 % and 45 % further than spheres. The largest differences occur for the smallest particle sizes.

Square films with d_{eq} = 27 µm display mean residence times of 13.76 h, and glitter particles with d_{eq} = 43 µm remain airborne for 4.18 h. and 2.73 h. On average, films with d_{eq} = 58 µm remain for 3.68 h in the atmosphere. Glitters with 111 -316 µm diameters display similar e-folding times, namely 1.65 h, 1.60 h, 1.57 h, and 1.66 h. The largest glitters (479 µm and 929 µm diameters) remain airborne for 1.41 and 1.38 h on average.

The atmospheric residence times of spheres and glitters of the same volume are similar. The largest relative differences occur for the square films, with 93 % and 28 % for 27 µm and 58 µm diameter films, respectively. For 43 µm, 111 µm, and 188 µm diameter glitters, the percentage differences are 4 %, 5 %, and 0.6 %. For 262 µm, 316 µm, 479 µm, and 929 µm diameter particles, the differences are 13 %, 12 %, 2 %, and 7 %.

These results indicate that glitter, when released into the air can be transported on an urban and regional scale. This is particularly relevant for glitter released during parades or carnivals in cities, since pollution may spread to areas surrounding the city, including agricultural land or conservation areas. Furthermore, these particles might fragment and be transported even further, even across country boundaries. In this context, further regulations and bans for the use of plastics and glitters in particular are recommended. For now, awareness must be raised in order for consumers to change their habits regarding (micro)plastic, for example, a transition to biodegradable alternatives to glitter.

For the simulations, the maximum drag orientation configuration of the Bagheri and Bonadonna [2016] settling scheme has been used, as it agrees best with the measured settling velocities on average. However, for the larger particles, i.e., particles with diameters $\geq$ 316 µm, random orientation configuration might deliver even better results and maximum drag orientation might underestimate their settling velocities. On one hand, this could have reduced the differences between the atmospheric transport behavior of the different glitter sizes. On the other hand, this could have led to larger differences between the atmospheric transport of large glitters and their volume-equivalent spheres. Moreover, the time of day at which particles are released might have a large impact on their transport distances and residence times. The particles were released at 15:00 local time when convective conditions prevail; if the particles are released during nighttime, for example, their transport distances might be much shorter.

Research on microplastics is lacking when it comes to glitters, especially those used in cosmetics. More research into possible sources and pathways of glitter particles in the environment is needed. Furthermore, data on the production, sales, use, and emission of glitter particles is scarce and needs to be established. With this knowledge, further simulations, such as sensitivity analyses, can be performed to identify regions susceptible to the deposition of microplastics and to quantify the concentration and deposition rates of these particles accurately. Additionally, the simulations could be repeated when particles are released at nighttime to investigate the impact of convective updrafts.

The environmental risks of microplastics are no longer disputable. In this context, awareness must be raised in order for consumers to change their consumption habits. Most of all, additional regulations and bans are needed for glitter particles, just like they have been established for microbeads in cosmetics. The EU already restricted microplastics, including glitter on its own and in products [Regulation 2023/2055.]. In the UK, if glitter is contained in "rinse-off" cosmetics and personal care products, it is covered by the 2018 ban on microbeads in cosmetics; other glitters, for example, craft glitters, are not [Gabbatiss]. Due to environmental concerns, 61 independent music festivals in the UK banned the use of plastic glitter in the summer of 2018 [Street]. For now, a change to biodegradable alternatives to glitter is necessary.

Bibliography

S. Abbasi, B. Keshavarzi, F. Moore, H. Delshab, N. Soltani, and A. Sorooshian. Investigation of microrubbers, microplastics and heavy metals in street dust: a study in Bushehr city, Iran. *Environmental Earth Sciences*, 76:1–19, 2017. URL https://doi.org/10.1007/s12665-017-7137-0.

M. B. Alfonso, A. H. Arias, A. C. Ronda, and M. C. Piccolo. Continental microplastics: Presence, features, and environmental transport pathways. *Science of The Total Environment*, 799: 149447, 2021. ISSN 0048-9697. doi: https://doi.org/10.1016/j.scitotenv.2021.149447. URL https://www.sciencedirect.com/science/article/pii/S0048969721045216.

S. Allen, D. Allen, V. R. Phoenix, G. Le Roux, P. Durántez Jiménez, A. Simonneau, S. Binet, and D. Galop. Atmospheric transport and deposition of microplastics in a remote mountain catchment. *Nature Geoscience*, 12(5), 2020. doi: 10.1038/s41561-019-0335-5. URL https://doi.org/10.1038/s41561-019-0335-5.

H.S. Auta, C.U Emenike, and S.H Fauziah. Distribution and importance of microplastics in the marine environment: A review of the sources, fate, effects, and potential solutions. *Environment International*, 102:165–176, 2017. ISSN 0160-4120. doi: https://doi.org/10.1016/j.envint.2017.02.013. URL https://www.sciencedirect.com/science/article/pii/S016041201631011X.

G. Bagheri and C. Bonadonna. On the drag of freely falling non-spherical particles. *Powder Technology*, 301:526–544, 2016. ISSN 0032-5910. doi: https://doi.org/10.1016/j.powtec.2016.06.015. URL https://www.sciencedirect.com/science/article/pii/S0032591016303539.

G. Bagheri and C. Bonadonna. Erratum to "On the drag of freely falling non-spherical particles". *Powder Technology*, 349:108, 2019. ISSN 0032-5910. doi: https://doi.org/10.1016/j.powtec.2018.12.040. URL https://www.sciencedirect.com/science/article/pii/S0032591018310775.

L. Bakels, D. Tatsii, A. Tipka, R. Thompson, M. Dütsch, M. Blaschek, P. Seibert, K. Baier, S. Bucci, M. Cassiani, S. Eckhardt, C. Groot Zwaaftink, S. Henne, P. Kaufmann, V. Lechner, C. Maurer, M. D. Mulder, I. Pisso, A. Plach, R. Subramanian, M. Vojta, and A. Stohl. Flexpart version 11: Improved accuracy, efficiency, and flexibility. *EGUsphere*, 2024:1–50, 2024. doi: 10.5194/egusphere-2024-1713. URL https://egusphere.copernicus.org/preprints/2024/egusphere-2024-1713/.

L. C. Becker, W. F. Bergfeld, D. V. Belsito, R. A. Hill, C. D. Klaassen, D. C. Liebler, J. G. Jr Marks, R. C. Shank, T. J. Slaga, P. W. Snyder, and F. A. Andersen. Safety Assessment of Modified Terephthalate Polymers as Used in Cosmetics. *International Journal of Toxicology*, 33:36–47, 2014.

M. Bergmann, S. Mützel, S. Primpke, M. B. Tekman, J. Trachsel, and G. Gerdts. White and wonderful? Microplastics prevail in snow from the Alps to the Arctic. *Sci. Adv*, 5(8):eaax1157, 2019. doi: 10.1126/sciadv.aax1157. URL https://www.science.org/doi/abs/10.1126/sciadv.aax1157.

R. D Blackledge and E. L Jones Jr. All that glitters is gold! *Forensic analysis on the cutting edge: New methods for trace evidence analysis*, pages 1–32, 2007.

M. Bläsing and W. Amelung. Plastics in soil: Analytical methods and possible sources. *Science of The Total Environment*, 612:422–435, 2018. ISSN 0048-9697. doi: https://doi.org/10.1016/j.scitotenv.2017.08.086. URL https://www.sciencedirect.com/science/article/pii/S0048969717320843.

J. Boucher and D. Friot. Primary Microplastics in the Oceans: A Global Evaluation of Sources. *Gland, Switzerland: IUCN.*, 2017. doi: dx.doi.org/10.2305/IUCN.CH.2017.01.en. URL www.iucn.org/resources/publications.

J. Brahney, M. Hallerud, E. Heim, M. Hahnenberger, and S. Sukumaran. Plastic rain in protected areas of the united states. *Science*, 368(6496):1257–1260, 2020. doi: 10.1126/science.aaz5819. URL https://www.science.org/doi/abs/10.1126/science.aaz5819.

G. P. Brasseur and D. J. Jacob. *Modeling of Atmospheric Chemistry*. Cambridge University Press, 2017.

D. Brennecke, B. Duarte, F. Paiva, I. Caçador, and J. Canning-Clode. Microplastics as vector for heavy metal contamination from the marine environment. *Estuarine, Coastal and Shelf Science*, 178:189–195, 2016. ISSN 0272-7714. doi: https://doi.org/10.1016/j.ecss.2015.12.003. URL https://www.sciencedirect.com/science/article/pii/S027277141530158X.

R. Clift and W. H. Gauvin. Motion of entrained particles in gas streams. *The Canadian Journal of Chemical Engineering*, 49(4):439–448, 1971. doi: https://doi.org/10.1002/cjce.5450490403. URL https://onlinelibrary.wiley.com/doi/abs/10.1002/cjce.5450490403.

M. Cole, P. Lindeque, C. Halsband, and T. S. Galloway. Microplastics as contaminants in the marine environment: A review. *Marine Pollution Bulletin*, 62(12):2588–2597, 2011. ISSN 0025-326X. doi: https://doi.org/10.1016/j.marpolbul.2011.09.025. URL https://www.sciencedirect.com/science/article/pii/S0025326X11005133.

R. Coyle, M. Service, U. Witte, G. Hardiman, and J. McKinley. Modeling microplastic transport in the marine environment: Testing empirical models of particle terminal sinking velocity for irregularly shaped particles. *ACS ES&T Water*, 3(4):984–995, 2023. doi: 10.1021/acsestwater.2c00466.

R. Dris, J. Gasperi, M. Saad, C. Mirande, and B. Tassin. Synthetic fibers in atmospheric fallout: A source of microplastics in the environment? *Environmental Pollution*, 104(1):290–293, 2016. ISSN 0025-326X. doi: https://doi.org/10.1016/j.marpolbul.2016.01.006. URL https://www.sciencedirect.com/science/article/pii/S0025326X16300066.

K. Duis and A. Coors. Microplastics in the aquatic and terrestrial environment: sources (with a specific focus on personal care products), fate and effects. *Environmental Sciences Europe*, 28, 2016. doi: 10.1186/s12302-015-0069-y. URL https://doi.org/10.1186/s12302-015-0069-y.

N. Evangeliou, H. Grythe, Z. Klimont, C. Heyes, S. Eckhardt, S. Lopez-Aparicio, and A. Stohl. Atmospheric transport is a major pathway of microplastics to remote regions. *Nature Communications*, 11, 2020. URL https://doi.org/10.1038/s41467-020-17201-9.

J. Gabbatiss. (16. November 2017). Glitter should be banned over environmental impact, scientists warn. *Independent*. URL https://www.independent.co.uk/climate-change/news/glitter-ban-environment-microbead-impact-microplastics-scientists-warning-deep-ocean-a8056196.html.

L. Garcia-Carreras, DJ Parker, JH Marsham, PD Rosenberg, IM Brooks, AP Lock, F Marenco, JB McQuaid, and M Hobby. The turbulent structure and diurnal growth of the saharan atmospheric boundary layer. *Journal of the Atmospheric Sciences*, 72(2):693–713, 2015.

C. Guerranti, T. Martellini, G. Perra, C. Scopetani, and A. Cincinelli. Microplastics in cosmetics: Environmental issues and needs for global bans. *Environmental Toxicology and Pharmacology*, 68:75–79, 2019. ISSN 1382-6689. doi: https://doi.org/10.1016/j.etap.2019.03.007. URL https://www.sciencedirect.com/science/article/pii/S1382668918305635.

N.B. Hartmann, T. Hüffer, R.C. Thompson, M. Hassellöv, A. Verschoor, A.E. Daugaard, S. Rist, T. Karlsson, N. Brennholt, M. Cole, M.P. Herrling, M.C. Hess, N.P. Ivleva, A.L. Lusher, and M. Wagner. Are We Speaking the Same Language? Recommendations for a Definition and Categorization Framework for Plastic Debris. *Environ Sci Technol.*, 53(3):1039–1047, 2019. doi: 10.1021/acs.est.8b05297. URL https://doi.org/10.1021/acs.est.8b05297.

H. Hersbach, B. Bell, P. Berrisford, S. Hirahara, A. Horányi, J. Muñoz-Sabater, ..., and J. N Thépaut. The ERA5 global reanalysis. *Quarterly Journal of the Royal Meteorological Society*, 146:1999–2049, 2020.

W. C. Hinds and Y. Zhu. *Aerosol Technology: Properties, Behavior, and Measurement of Airborne Particles*. John Wiley & Sons, 2022.

R. Hurley, J. Woodward, and J. J. Rothwell. Microplastic contamination of river beds significantly reduced by catchment-wide flooding. *Nature Geoscience*, 11:251–257, 2018. URL https://doi.org/10.1038/s41561-018-0080-1.

S. Kim, A. Sin, H. Nam, Y. Park, H. Lee, and C. Han. Advanced oxidation processes for microplastics degradation: A recent trend. *Chemical Engineering Journal Advances*, 9:100213, 2022. ISSN 2666-8211. doi: https://doi.org/10.1016/j.ceja.2021.100213. URL https://www.sciencedirect.com/science/article/pii/S2666821121001289.

K. Liu, T. Wu, X. Wang, Z. Song, C. Zong, N. Wei, and D. Li. Consistent transport of terrestrial microplastics to the ocean through atmosphere. *Environmental Science & Technology*, 53(18):10612–10619, 2019. doi: 10.1021/acs.est.9b03427. URL https://doi.org/10.1021/acs.est.9b03427. PMID: 31408609.

A. L. Lusher, R. Hurley, C. Vogelsang, L. Nizzetto, and M. Olsen. Mapping microplastics in sludge. *Norsk institutt for vannforskning*, 2017. URL https://niva.brage.unit.no/niva-xmlui/handle/11250/2493527.

M. J. Machado, R. B. Dextro, R. B. Cruz, S. R. Cotta, and M. F. Fiore. Response of two cyanobacterial strains to non-biodegradable glitter particles. *Aquatic Toxicology*, 260:106590, 2023. ISSN 0166-445X. doi: https://doi.org/10.1016/j.aquatox.2023.106590. URL https://www.sciencedirect.com/science/article/pii/S0166445X23001935.

NJ Middleton, PR Betzer, and PA Bull. Long-range transport of 'giant'aeolian quartz grains: linkage with discrete sedimentary sources and implications for protective particle transfer. *Marine Geology*, 177(3-4):411–417, 2001.

F. Petersen and J. A. Hubbart. The occurrence and transport of microplastics: The state of the science. *Science of The Total Environment*, 758:143936, 2021. ISSN 0048-9697. doi: https://doi.org/10.1016/j.scitotenv.2020.143936. URL https://www.sciencedirect.com/science/article/pii/S0048969720374672.

I. Pisso, E. Sollum, H. Grythe, N. I. Kristiansen, M. Cassiani, S. Eckhardt, D. Arnold, D. Morton, R. L. Thompson, C. D. Groot Zwaaftink, N. Evangeliou, H. Sodemann, L. Haimberger, S. Henne, D. Brunner, J. F. Burkhart, A. Fouilloux, J. Brioude, A. Philipp, P. Seibert, and A. Stohl. The lagrangian particle dispersion model flexpart version 10.4. *Geoscientific Model Development*, 12(12):4955–4997, 2019. doi: 10.5194/gmd-12-4955-2019. URL https://gmd.copernicus.org/articles/12/4955/2019/.

F. Provenza, S. Anselmi, A. Specchiulli, M. Piccardo, D. Barceló, M. Prearo, P. Pastorino, and M. Renzi. Sparkling plastic: Effects of exposure to glitter on the Mediterranean mussel Mytilus galloprovincialis. *Environmental Toxicology and Pharmacology*, 96:103994, 2022. ISSN 1382-6689. doi: https://doi.org/10.1016/j.etap.2022.103994. URL https://www.sciencedirect.com/science/article/pii/S1382668922001879.

S. Raju, M. Carbery, A. Kuttykattil, K. Senthirajah, A. Lundmark, Z. Rogers, Suresh SCB, G. Evans, and T. Palanisami. Improved methodology to determine the fate and transport of microplastics in a secondary wastewater treatment plant. *Water Research*, 173:115549, 2020. ISSN 0043-1354. doi: https://doi.org/10.1016/j.watres.2020.115549. URL https://www.sciencedirect.com/science/article/pii/S0043135420300853.

Regulation 2023/2055. Commission Regulation (EU) 2023/2055 of September 25 2023 amending Annex XVII to Regulation (EC) No. 1907/2006 of the European Parliament and the Coucil concerning the Registration, Evaluation, Authorization and Restriction of Chemicals (REACH) as regards synthetic polymer microparticles. *Official Journal of the European Union*. URL https://eur-lex.europa.eu/legal-content/EN/ALL/?uri=CELEX:32023R2055.

A. S. W. Reininger. Gravitational Settling of Microplastic Films, 2024.

J. Renard, F. Dulac, P. Durand, Q. Bourgeois, C. Denjean, D. Vignelles, B. Couté, M. Jeannot, N. Verdier, and M. Mallet. In situ measurements of desert dust particles above the western

mediterranean sea with the balloon-borne light optical aerosol counter/sizer (loac) during the charmex campaign of summer 2013. *Atmospheric Chemistry and Physics*, 18(5):3677–3699, 2018.

J. Saxby, F. Beckett, K. Cashman, A. Rust, and E. Tennant. The impact of particle shape on fall velocity: Implications for volcanic ash dispersion modelling. *Journal of Volcanology and Geothermal Research*, 362:32–48, 2018. ISSN 0377-0273. doi: https://doi.org/10.1016/j.jvolgeores.2018.08.006. URL https://www.sciencedirect.com/science/article/pii/S037702731830177X.

J. H. Seinfeld and S. N. Pandis. *Atmospheric Chemistry and Physics: From Air Pollution to Climate Change*. John Wiley & Sons, 2016.

C. Street. (6. August 2018). 61 UK music festivals are banning glitter. Here's why it's time to switch to biodegradable sparkle. *Evening Standard*. URL https://www.standard.co.uk/beauty/music-festivals-ban-glitter-microbeads-microplastic-a3812661.html.

J. Sun, X. Dai, Q. Wang, M. C.M. van Loosdrecht, and BJ Ni. Microplastics in wastewater treatment plants: Detection, occurrence and removal. *Water Research*, 152:21–37, 2019. ISSN 0043-1354. doi: https://doi.org/10.1016/j.watres.2018.12.050. URL https://www.sciencedirect.com/science/article/pii/S0043135418310686.

A. S. Tagg and J. A. Ivar do Sul. Is this your glitter? An overlooked but potentially environmentally-valuable microplastic. *Marine Pollution Bulletin*, 146:50–53, 2019. ISSN 0025-326X. doi: https://doi.org/10.1016/j.marpolbul.2019.05.068. URL https://www.sciencedirect.com/science/article/pii/S0025326X19304448.

D. Tatsii, S. Bucci, T. Bhowmick, J. Guettler, L. Bakels, G. Bagheri, and A. Stohl. Shape matters: Long-range transport of microplastic fibers in the atmosphere. *Environmental Science & Technology*, 58(1):671–682, 2024. doi: 10.1021/acs.est.3c08209.

M. Van Der Does, P. Knippertz, P. Zschenderlein, R Giles Harrison, and JBW Stuut. The mysterious long-range transport of giant mineral dust particles. *Science advances*, 4(12): eaau2768, 2018.

G. Varga, P. Dagsson-Waldhauserová, F. Gresina, and A. Helgadottir. Saharan dust and giant quartz particle transport towards iceland. *Scientific reports*, 11(1):11891, 2021.

C. Weaver. (21. December 2018). What Is Glitter? A strange journey to the glitter factory. *New York Times*. URL https://www.nytimes.com/2018/12/21/style/glitter-factory.html.

Y. Xiang., L. Jiang., Y. Zhou., Z. Luo., D. Zhi, J. Yang, and S. S. Lam. Microplastics and environmental pollutants: Key interaction and toxicology in aquatic and soil environments. *Journal of Hazardous Materials*, 422:126843, 2022. ISSN 0304-3894. doi: https://doi.org/10.1016/j.jhazmat.2021.126843. URL https://www.sciencedirect.com/science/article/pii/S0304389421018112.

M. Yurtsever. Tiny, shiny, and colorful microplastics: Are regular glitters a significant source of microplastics? *Marine Pollution Bulletin*, 146:678–682, 2019a. ISSN 0025-326X. doi: https://doi.org/10.1016/j.marpolbul.2019.07.009. URL https://www.sciencedirect.com/science/article/pii/S0025326X19305405.

M. Yurtsever. Glitters as a Source of Primary Microplastics: An Approach to Environmental Responsibility and Ethics. *Journal of Agricultural and Environmental Ethics*, 32:459 – 478, 2019b. doi: 10.1007/s10806-019-09785-0. URL https://doi.org/10.1007/s10806-019-09785-0.

X. Zhang, T. Lin, and X. Wang. Investigation of microplastics release behavior from ozone-exposed plastic pipe materials. *Environmental Pollution*, 296:118758, 2022. ISSN 0269-7491. doi: https://doi.org/10.1016/j.envpol.2021.118758. URL https://www.sciencedirect.com/science/article/pii/S026974912102340X.

A. Appendix

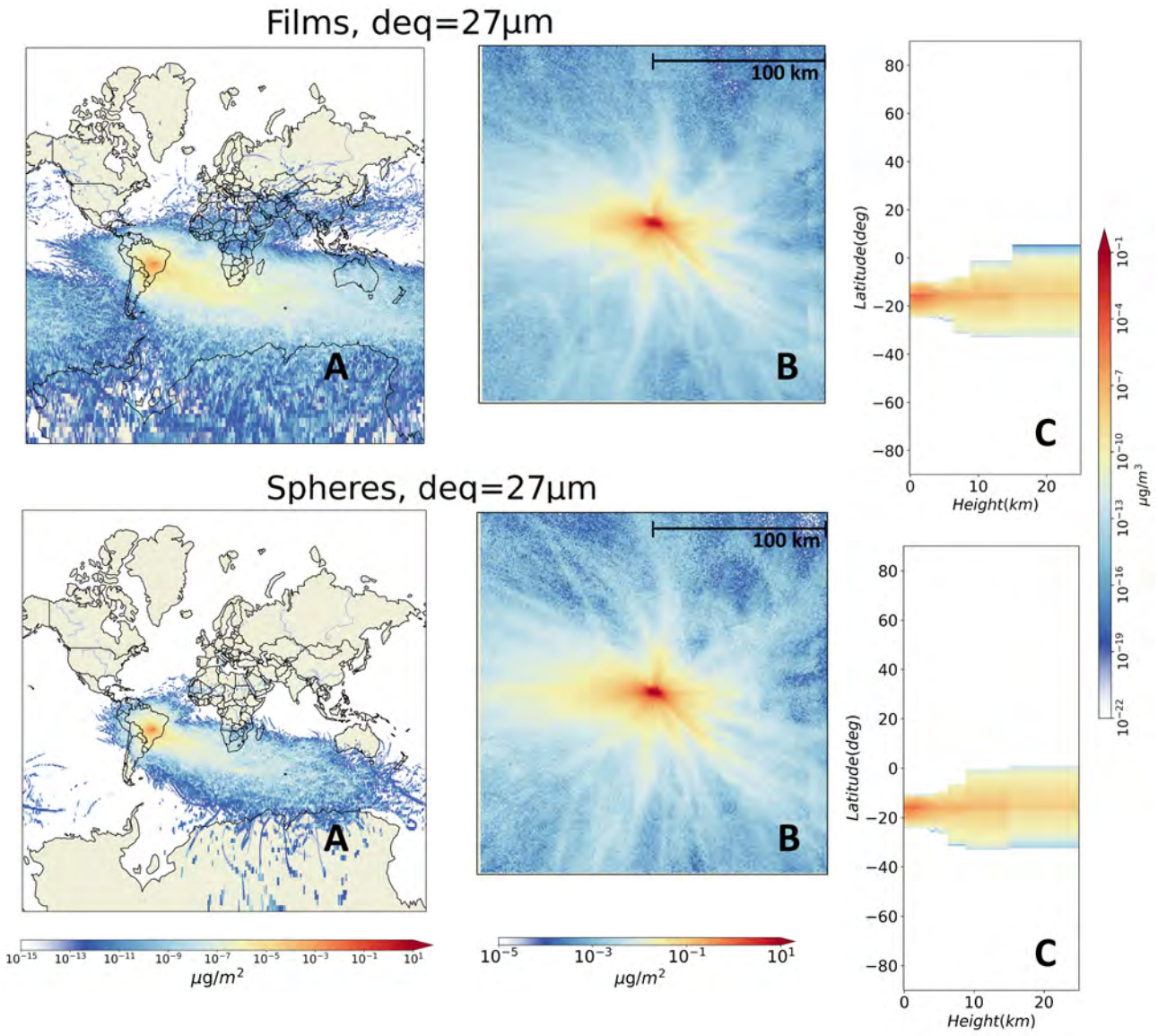

Figure A.1.: (A) Daily dry and wet deposition of films and spheres with d_{eq} = 27 µm, released in Brasília. (B) Daily dry and wet deposition in the nested grid around the release point Shanghai. (C) Zonal mean atmospheric mass concentration as a function of latitude and altitude.

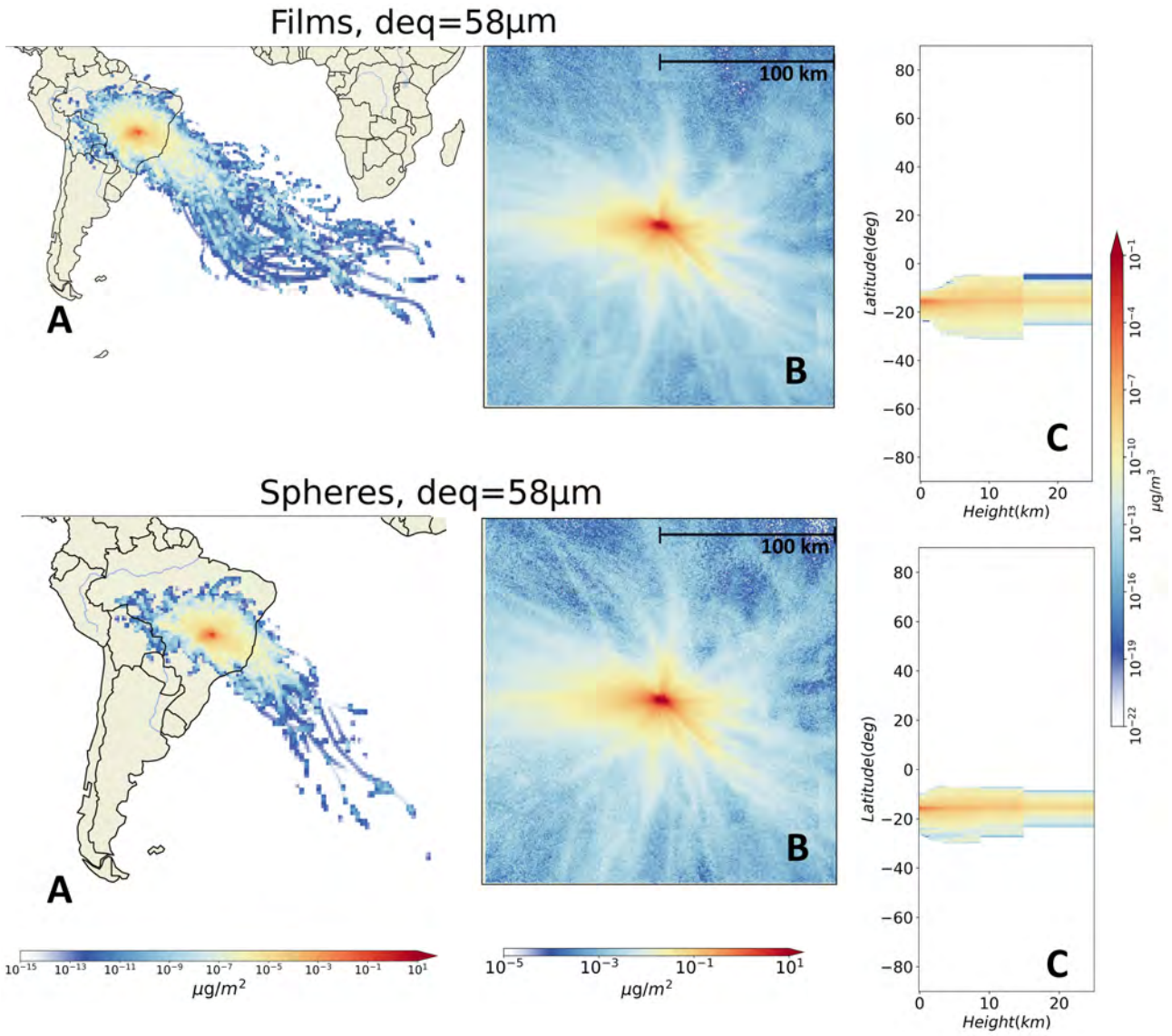

Figure A.2.: (A) Daily dry and wet deposition of films and spheres with d_{eq} = 58 µm, released in Brasília. (B) Daily dry and wet deposition in the nested grid around the release point Shanghai. (C) Zonal mean atmospheric mass concentration as a function of latitude and altitude.

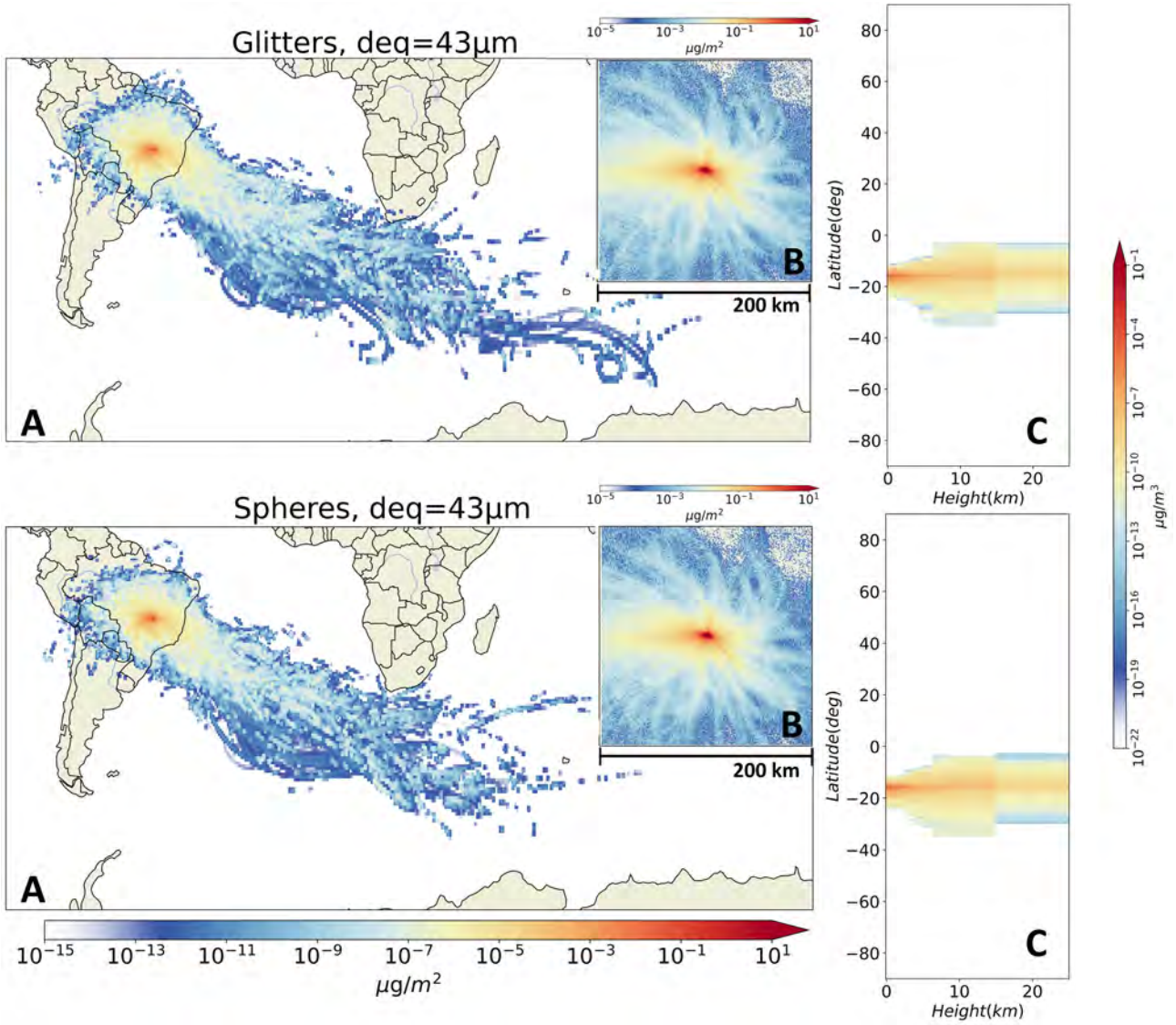

Figure A.3.: (A) Daily dry and wet deposition of glitters and spheres with $d_{eq} = 43$ µm, released in Brasília. (B) Daily dry and wet deposition in the nested grid around the release point Brasília. (C) Zonal mean atmospheric mass concentration as a function of latitude and altitude.

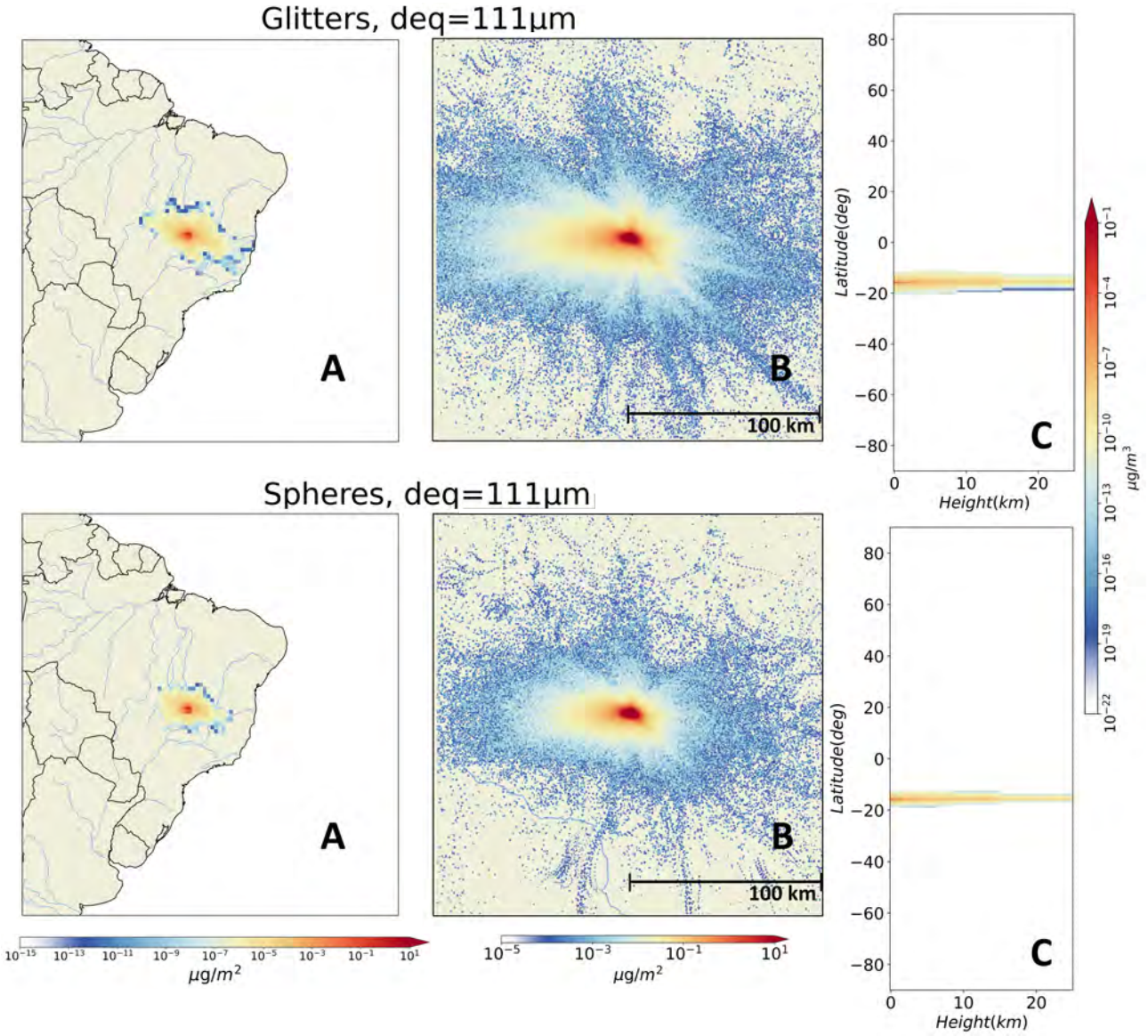

Figure A.4.: (A) Daily dry and wet deposition of glitters and spheres with $d_{eq} = 111$ µm, released in Brasília. (B) Daily dry and wet deposition in the nested grid around the release point Brasília. (C) Zonal mean atmospheric mass concentration as a function of latitude and altitude.

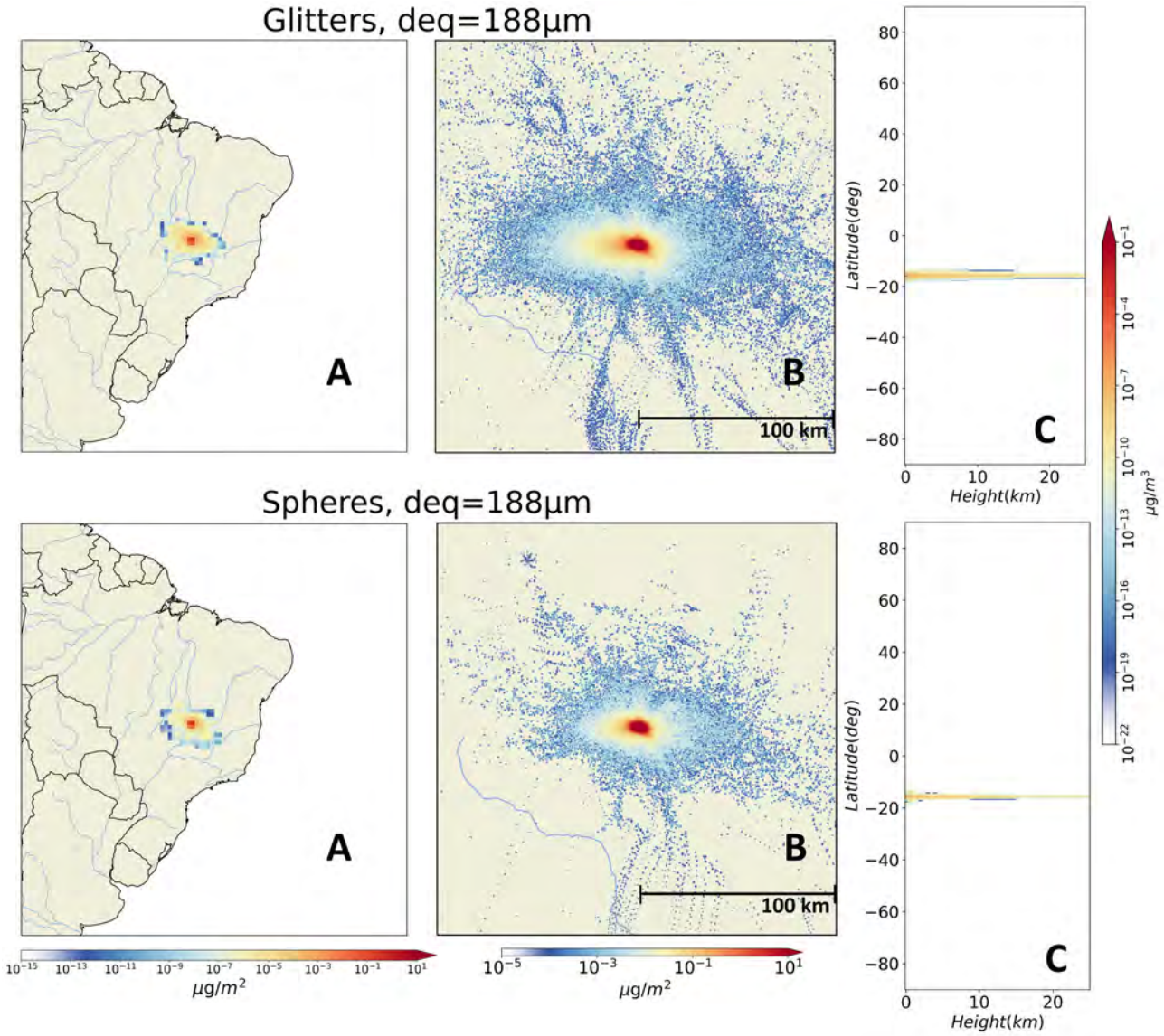

Figure A.5.: (A) Daily dry and wet deposition of glitters and spheres with d_{eq} = 188 µm, released in Brasília. (B) Daily dry and wet deposition in the nested grid around the release point Brasília. (C) Zonal mean atmospheric mass concentration as a function of latitude and altitude.

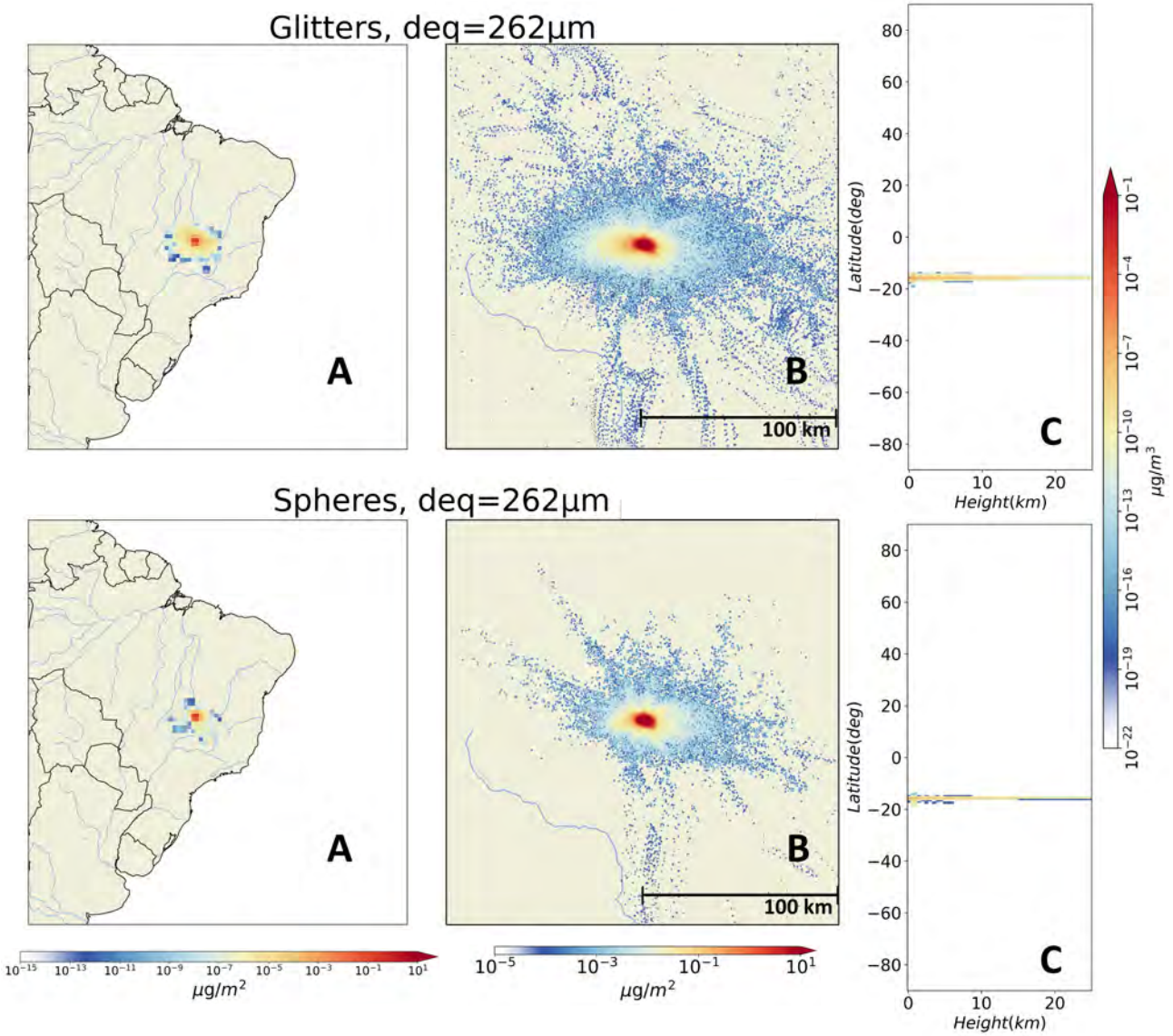

Figure A.6.: (A) Daily dry and wet deposition of glitters and spheres with $d_{eq} = 262$ µm, released in Brasília. (B) Daily dry and wet deposition in the nested grid around the release point Brasília. (C) Zonal mean atmospheric mass concentration as a function of latitude and altitude.

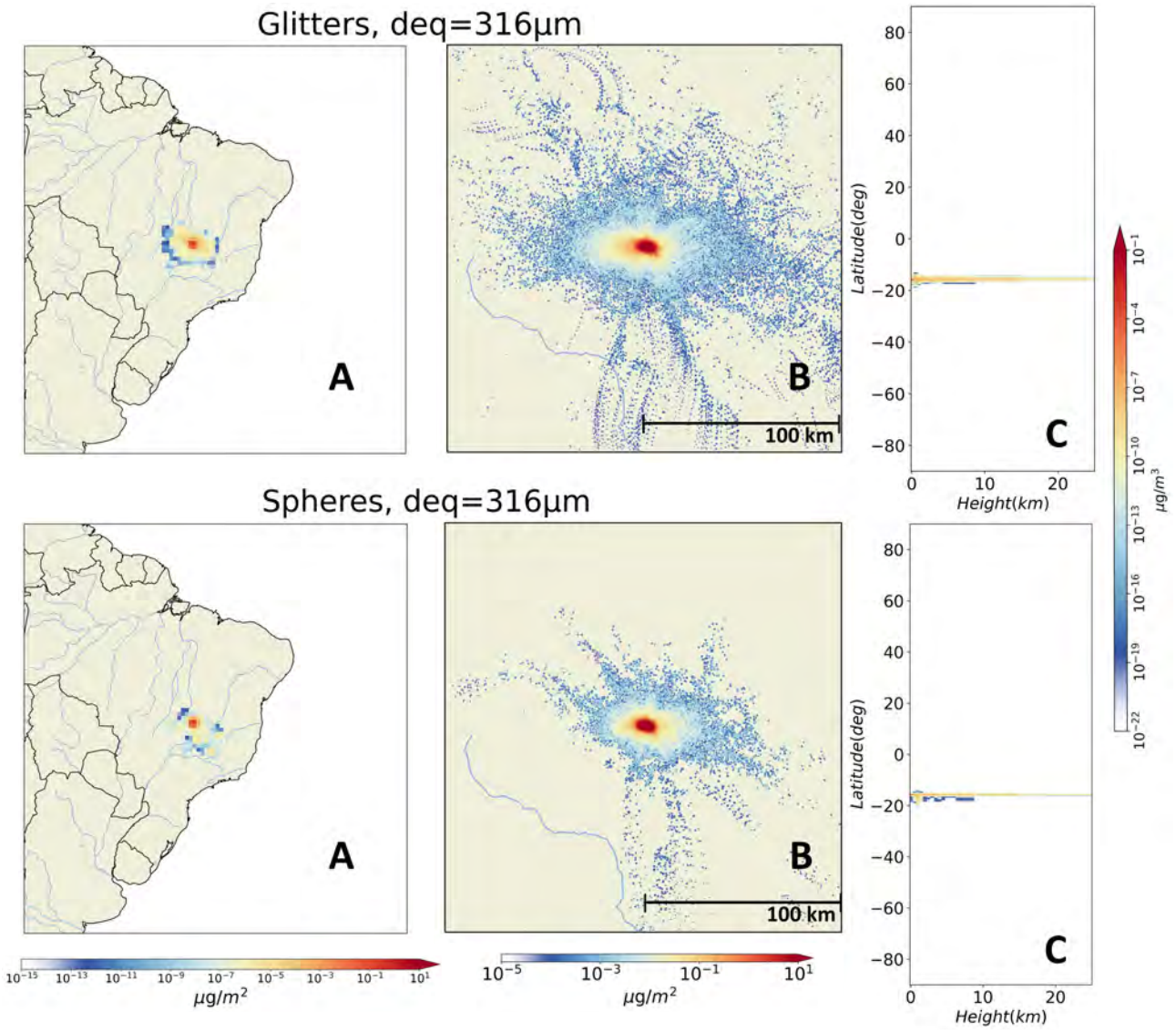

Figure A.7.: (A) Daily dry and wet deposition of glitters and spheres with d_{eq} = 316 µm, released in Brasília. (B) Daily dry and wet deposition in the nested grid around the release point Brasília. (C) Zonal mean atmospheric mass concentration as a function of latitude and altitude.

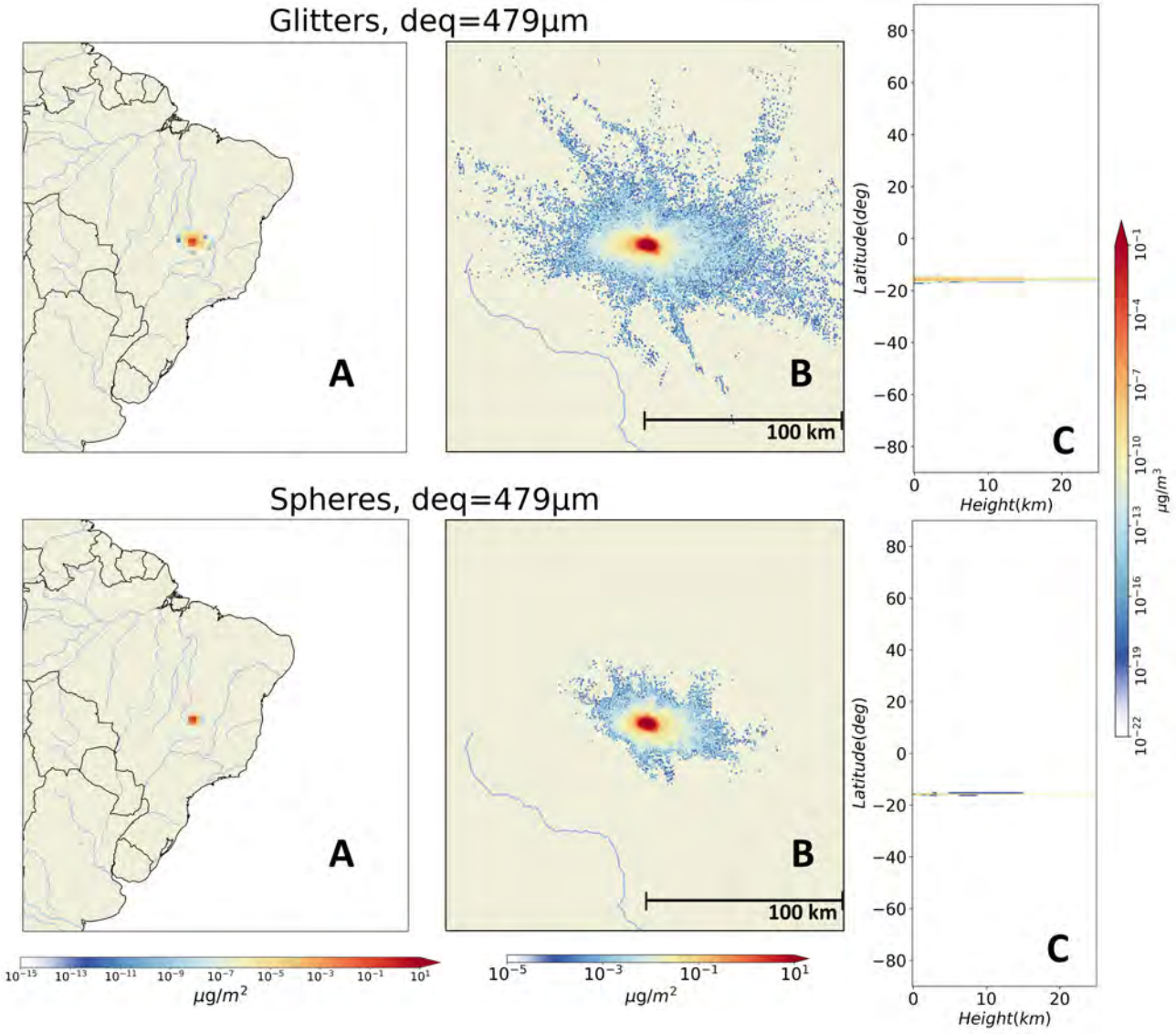

Figure A.8.: (A) Daily dry and wet deposition of glitters and spheres with $d_{eq} = 479$ µm, released in Brasília. (B) Daily dry and wet deposition in the nested grid around the release point Brasília. (C) Zonal mean atmospheric mass concentration as a function of latitude and altitude.

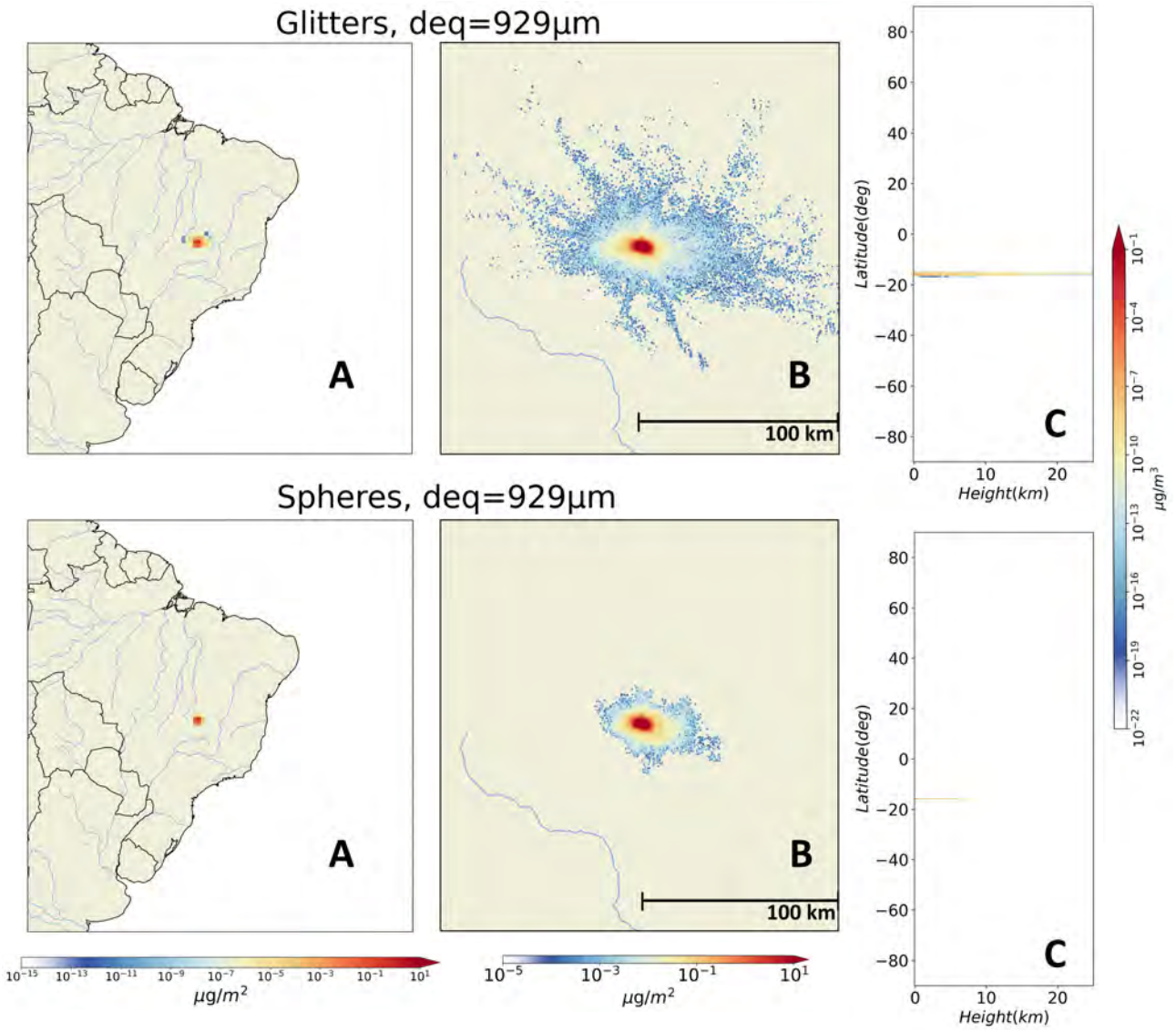

Figure A.9.: (A) Daily dry and wet deposition of glitters and spheres with d_{eq} = 929 µm, released in Brasília. (B) Daily dry and wet deposition in the nested grid around the release point Brasília. (C) Zonal mean atmospheric mass concentration as a function of latitude and altitude.

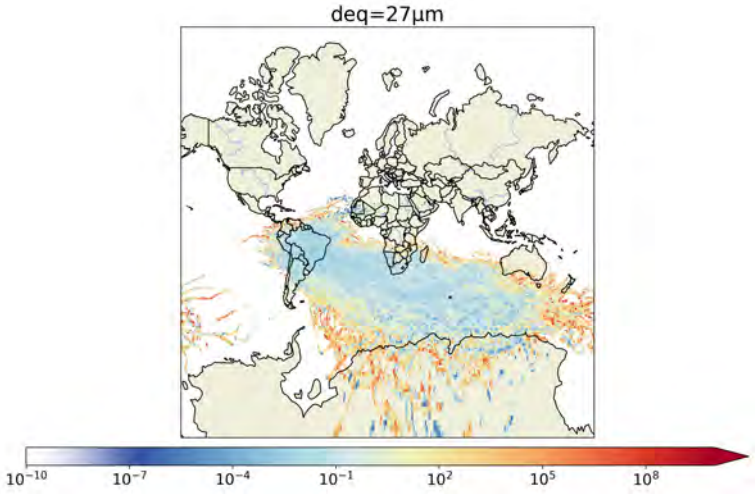

Figure A.10.: Daily total deposition ratio of films and spheres $d_{eq} = 27$ µm around the release point Brasília.

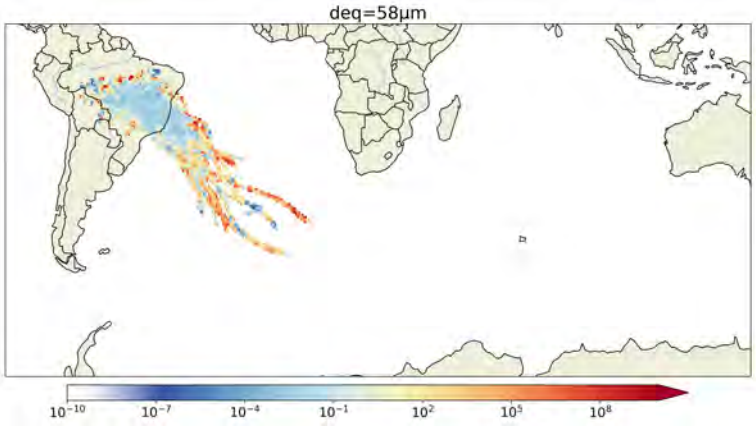

Figure A.11.: Daily total deposition ratio of films and spheres $d_{eq} = 58$ µm around the release point Brasília.

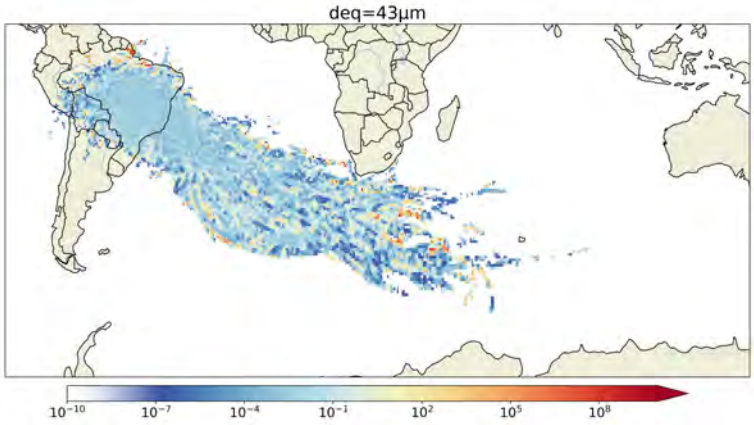

Figure A.12.: Daily total deposition ratio of glitters and spheres d_{eq} = 43 µm around the release point Brasília.

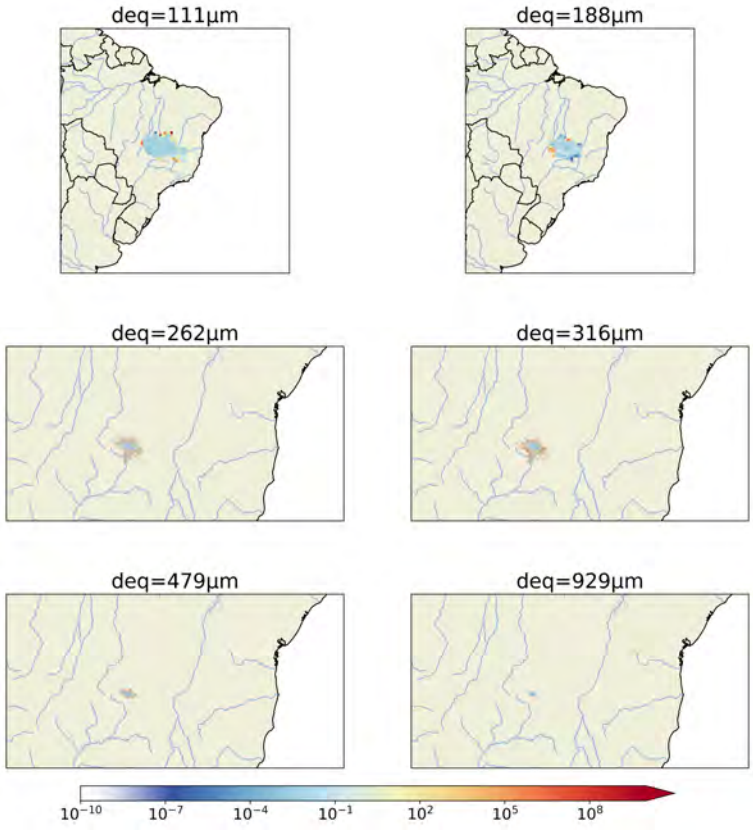

Figure A.13.: Daily total deposition ratio of glitters and spheres around the release point Brasília.

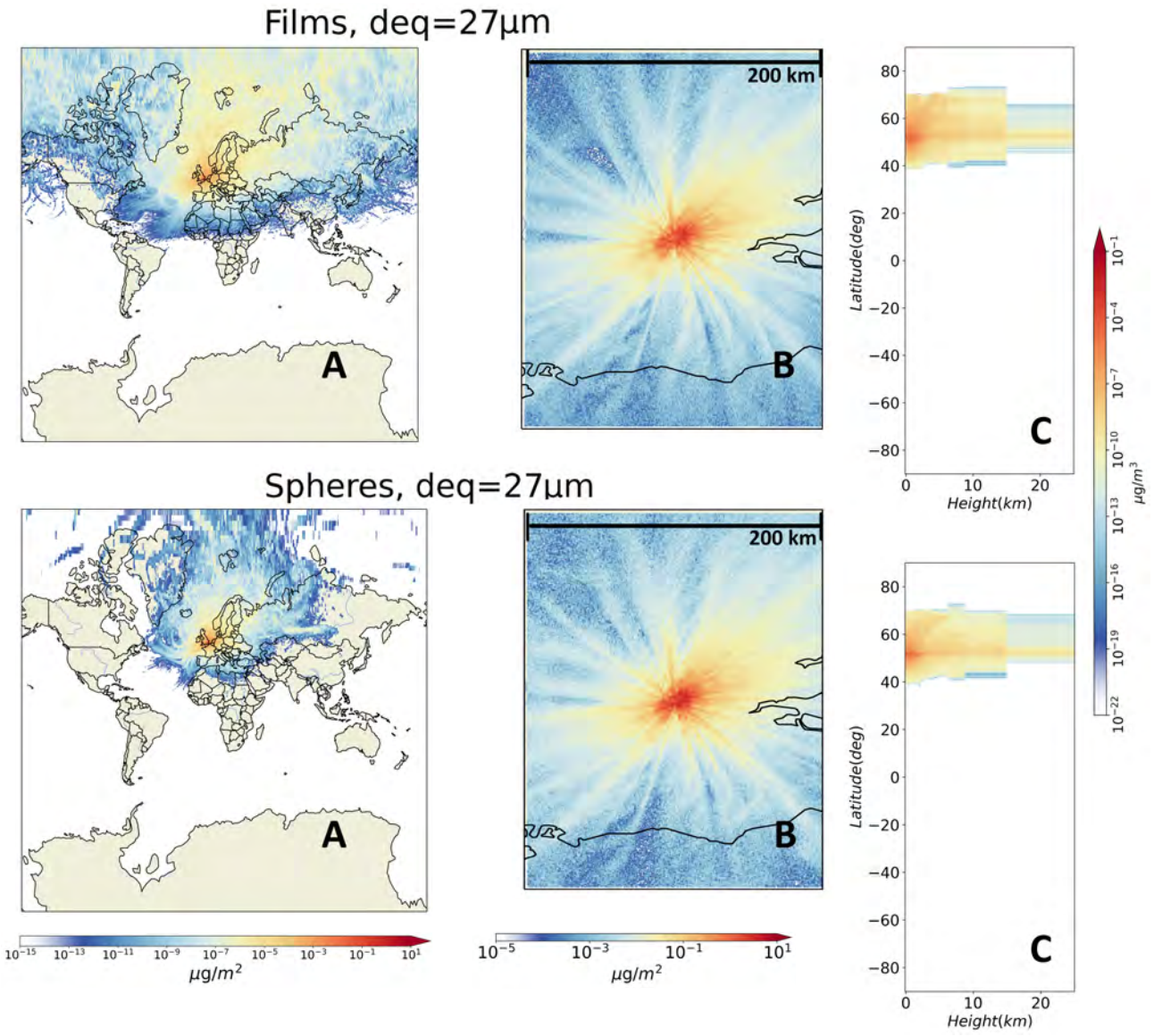

Figure A.14.: (A) Daily dry and wet deposition of films and spheres with d_{eq} = 27 µm, released in London. (B) Daily dry and wet deposition in the nested grid around the release point Shanghai. (C) Zonal mean atmospheric mass concentration as a function of latitude and altitude.

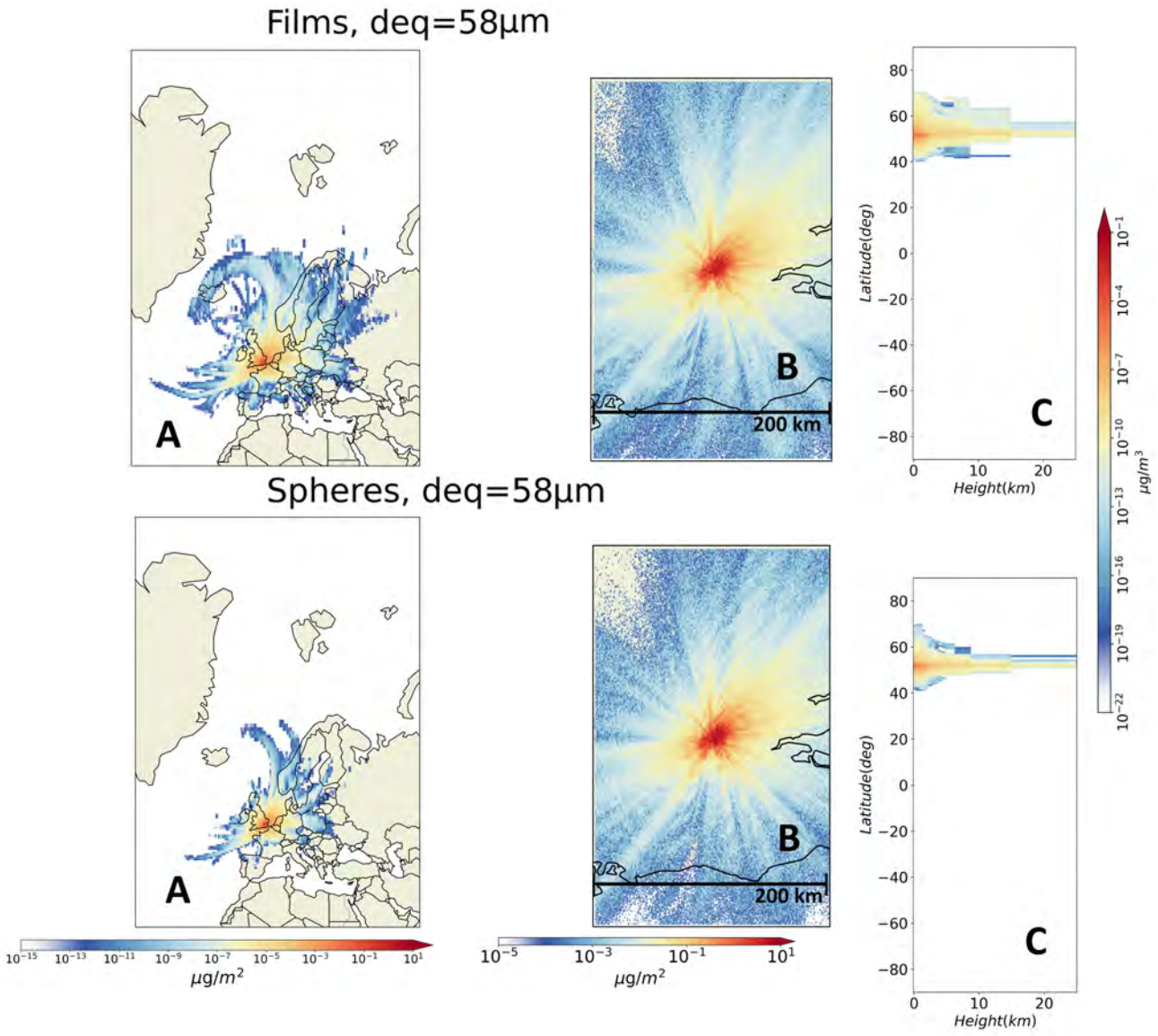

Figure A.15.: (A) Daily dry and wet deposition of films and spheres with d_{eq} = 58 µm, released in London. (B) Daily dry and wet deposition in the nested grid around the release point Shanghai. (C) Zonal mean atmospheric mass concentration as a function of latitude and altitude.

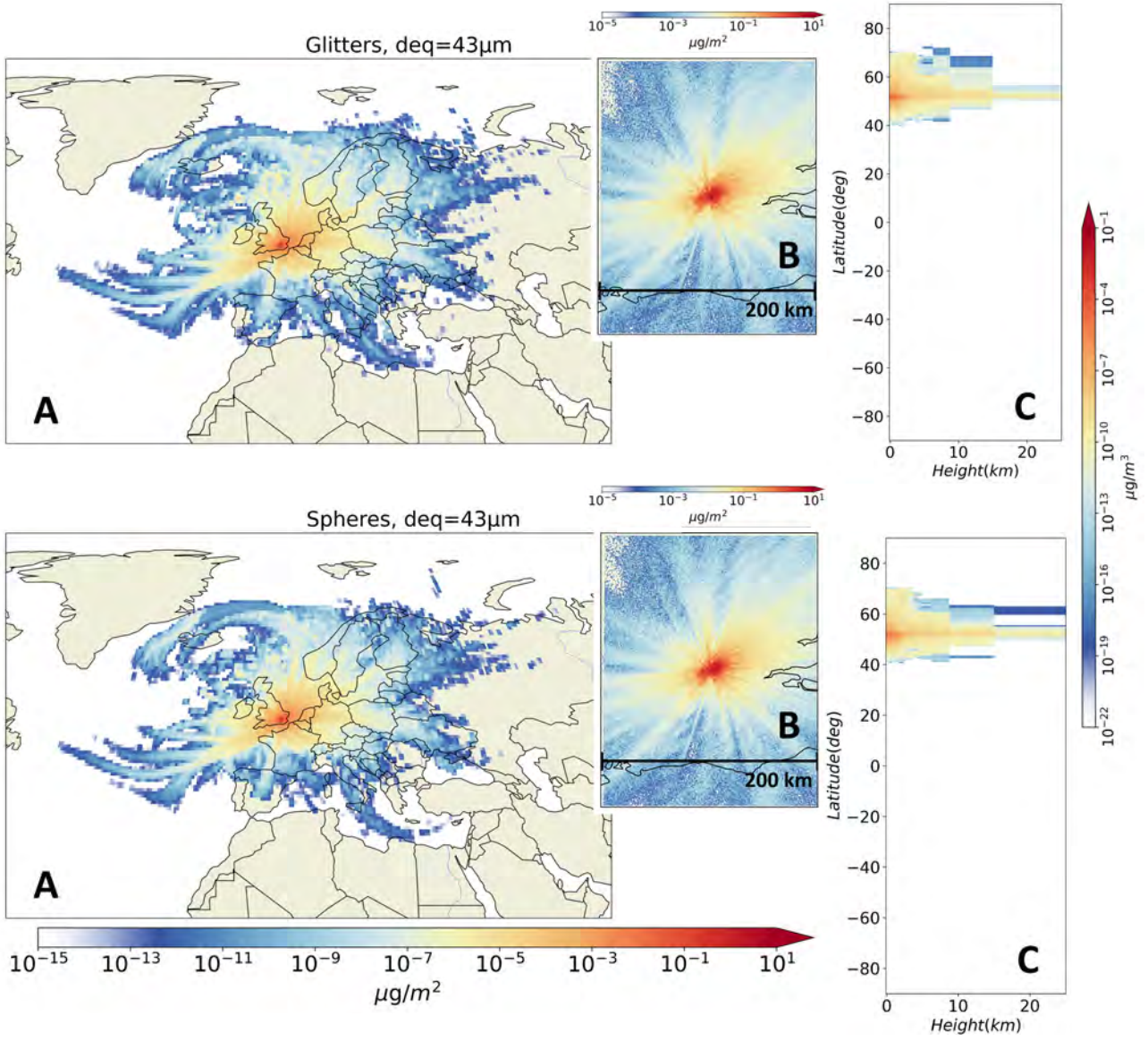

Figure A.16.: (A) Daily dry and wet deposition of glitters and spheres with $d_{eq} = 43$ µm, released in London. (B) Daily dry and wet deposition in the nested grid around the release point London. (C) Zonal mean atmospheric mass concentration as a function of latitude and altitude.

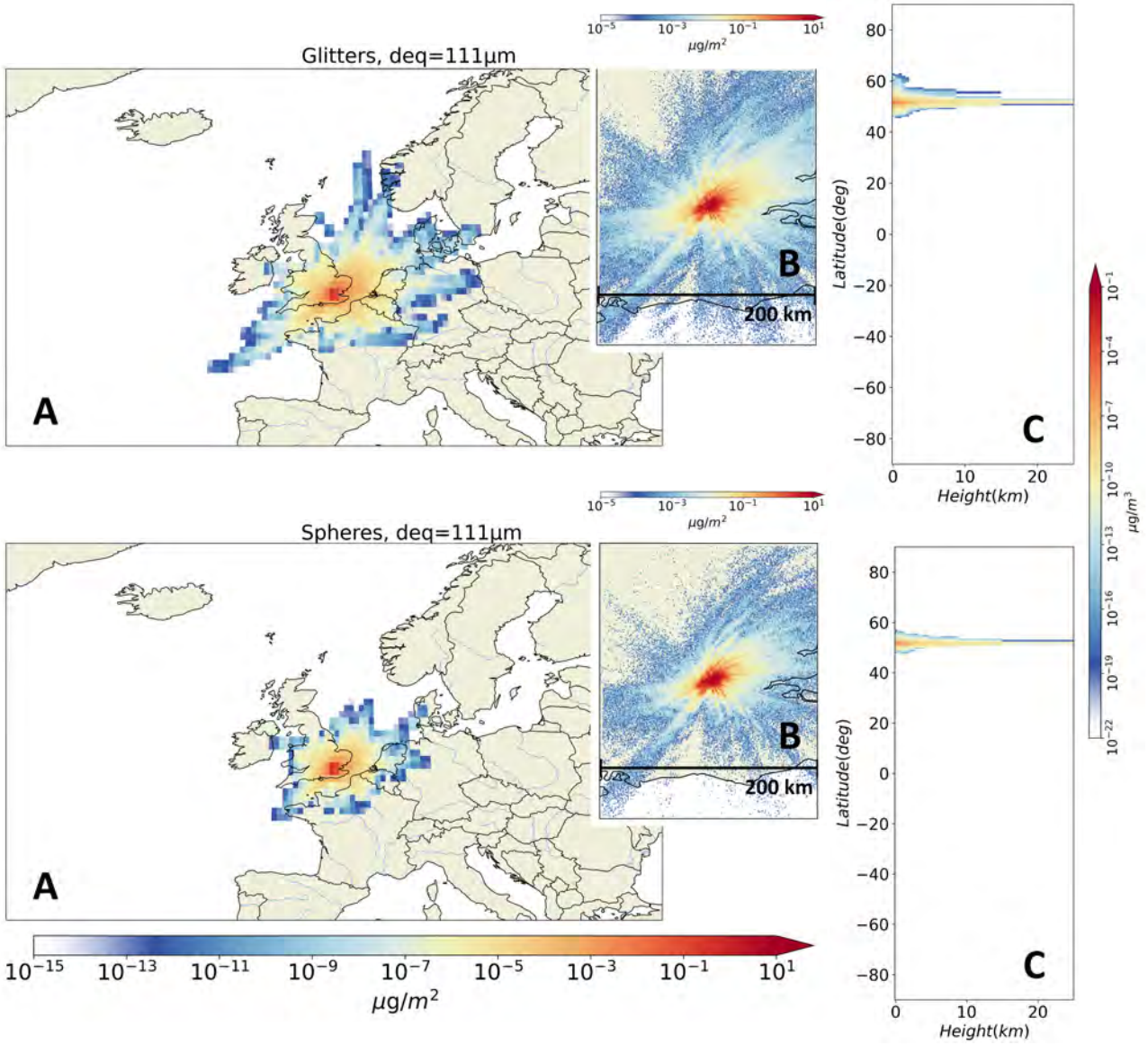

Figure A.17.: (A) Daily dry and wet deposition of glitters and spheres with d_{eq} = 111 µm, released in London. (B) Daily dry and wet deposition in the nested grid around the release point London. (C) Zonal mean atmospheric mass concentration as a function of latitude and altitude.

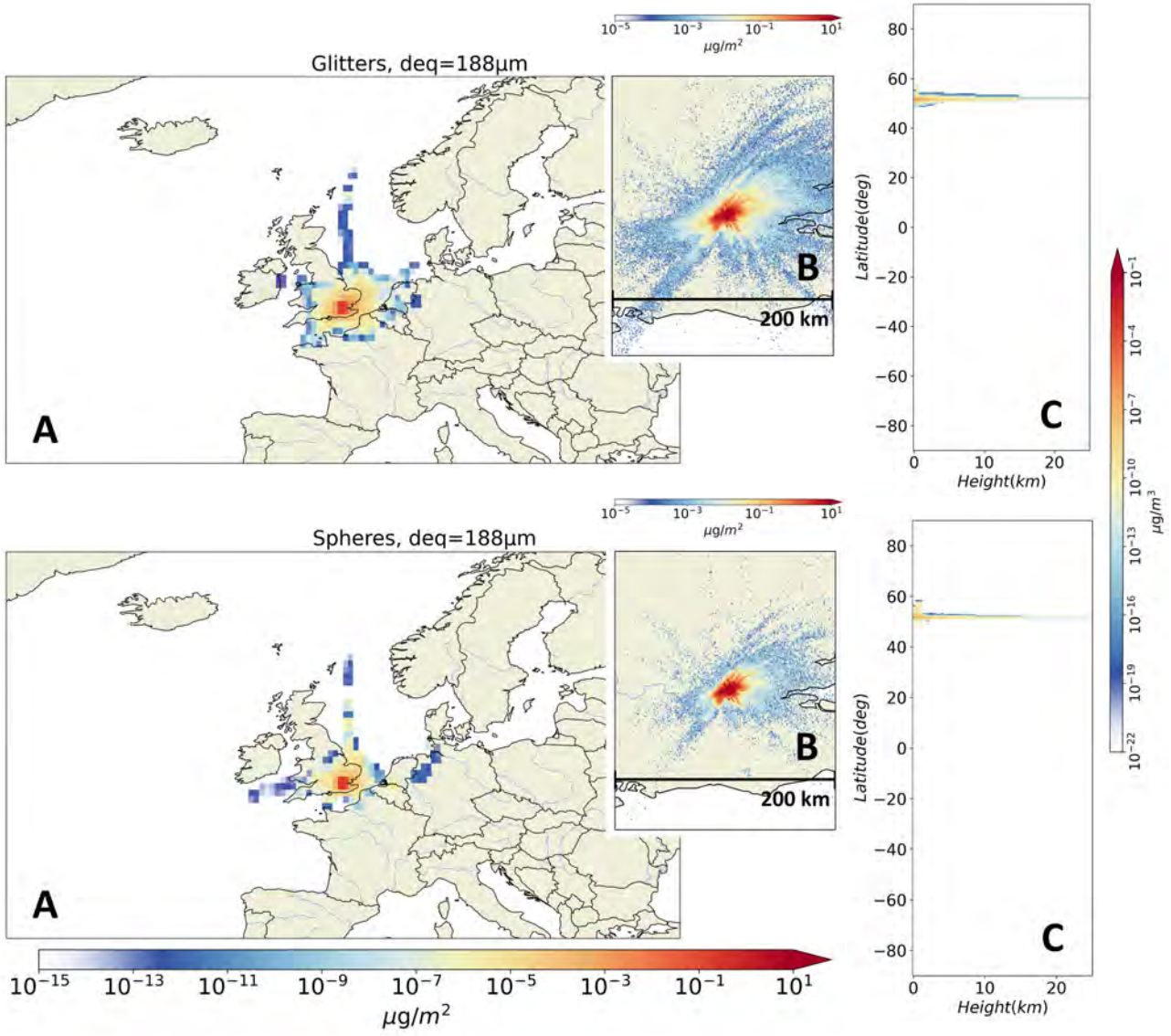

Figure A.18.: (A) Daily dry and wet deposition of glitters and spheres with d_{eq} = 188 µm, released in London. (B) Daily dry and wet deposition in the nested grid around the release point London. (C) Zonal mean atmospheric mass concentration as a function of latitude and altitude.

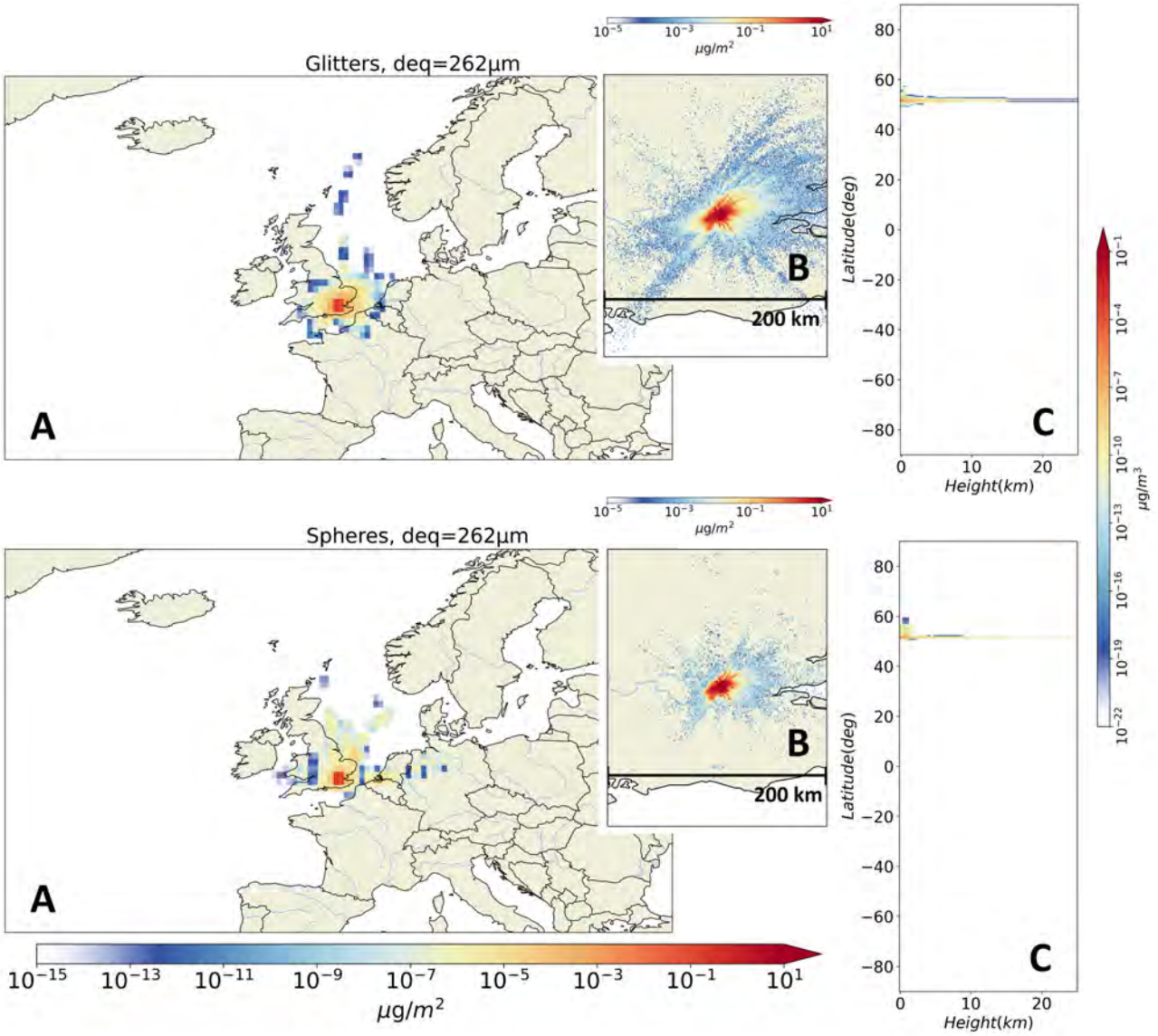

Figure A.19.: (A) Daily dry and wet deposition of glitters and spheres with d_{eq} = 262 µm, released in London. (B) Daily dry and wet deposition in the nested grid around the release point London. (C) Zonal mean atmospheric mass concentration as a function of latitude and altitude.

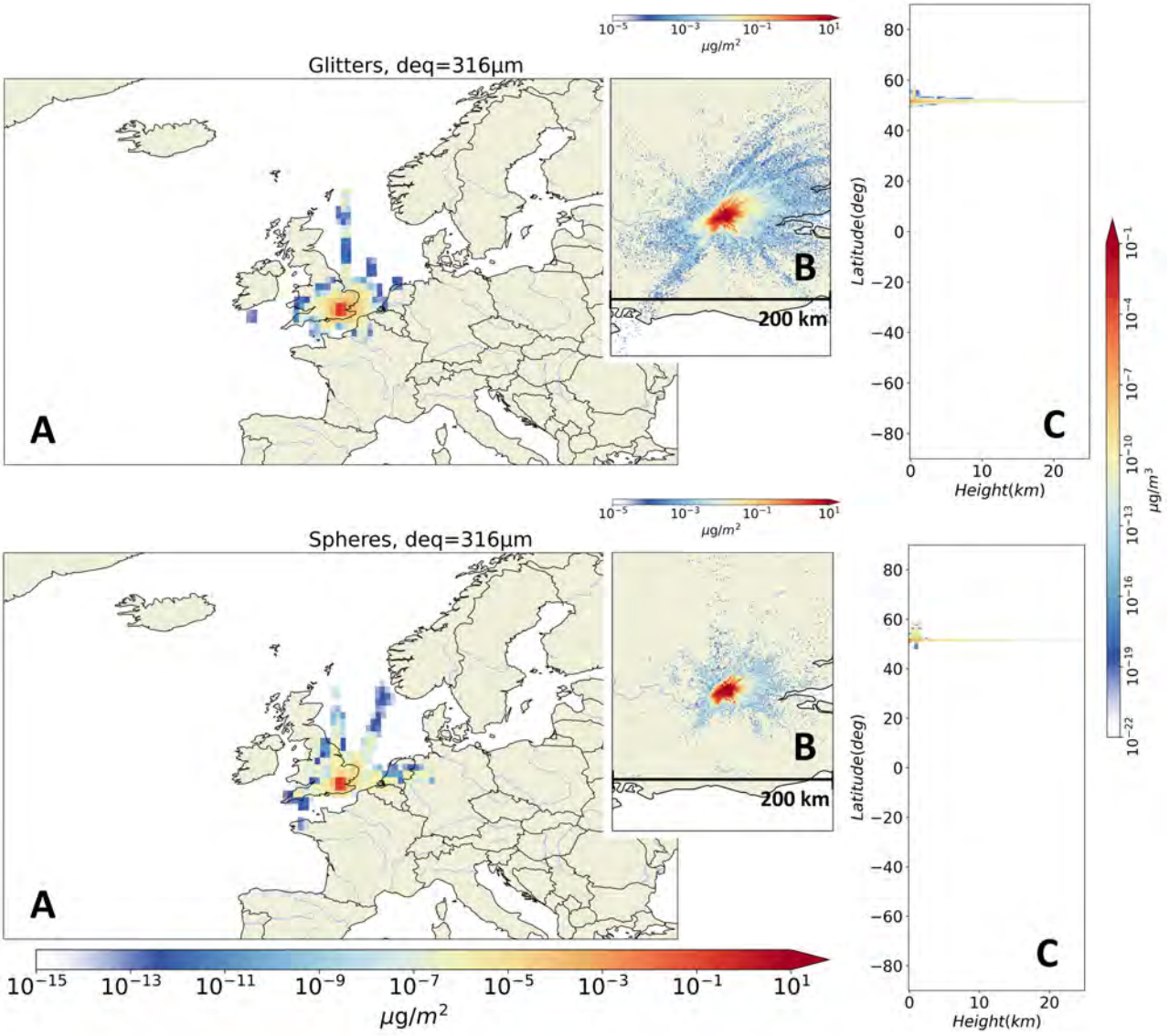

Figure A.20.: (A) Daily dry and wet deposition of glitters and spheres with $d_{eq} = 316$ µm, released in London. (B) Daily dry and wet deposition in the nested grid around the release point London. (C) Zonal mean atmospheric mass concentration as a function of latitude and altitude.

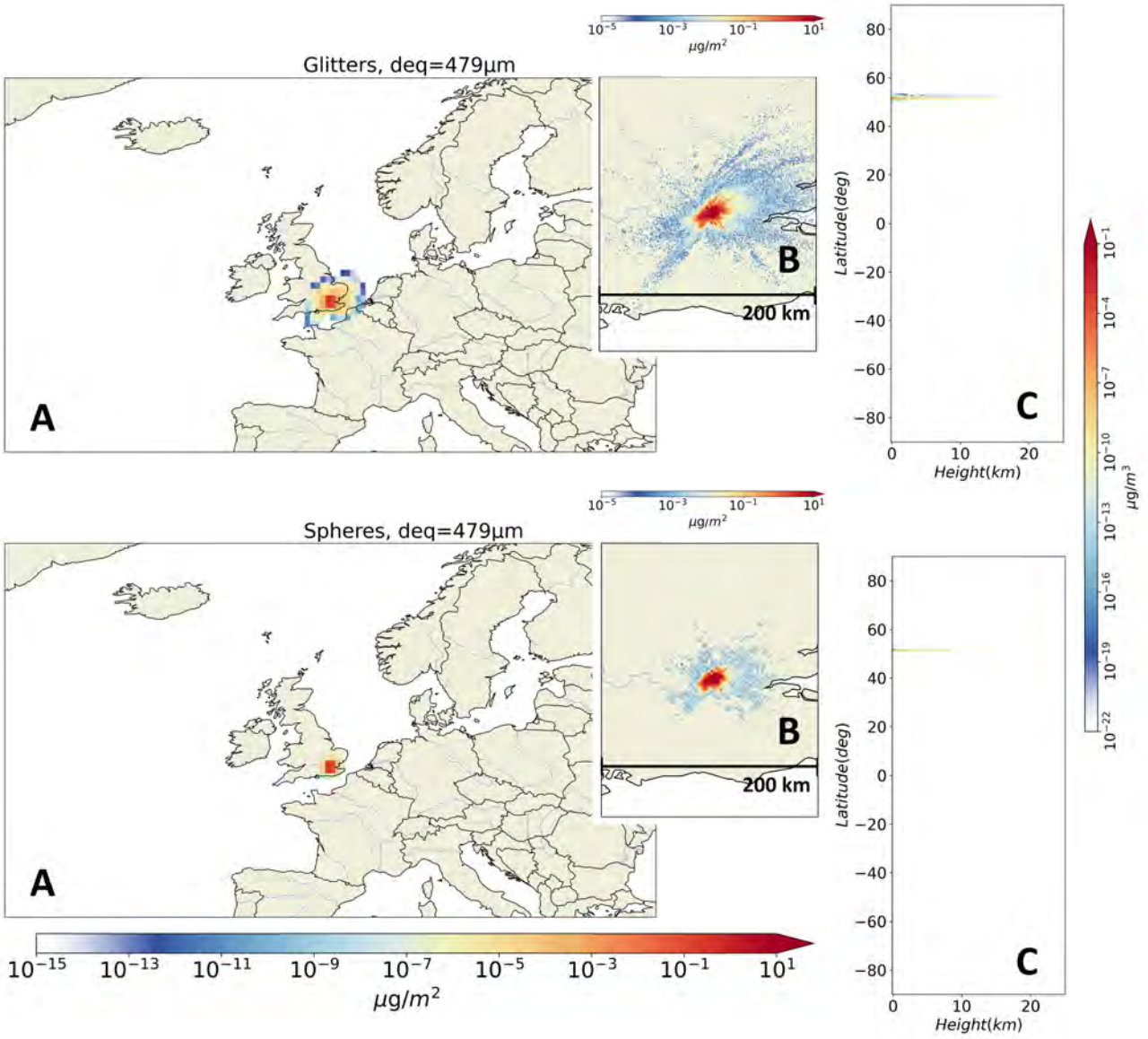

Figure A.21.: (A) Daily dry and wet deposition of glitters and spheres with d_{eq} = 479 µm, released in London. (B) Daily dry and wet deposition in the nested grid around the release point London. (C) Zonal mean atmospheric mass concentration as a function of latitude and altitude.

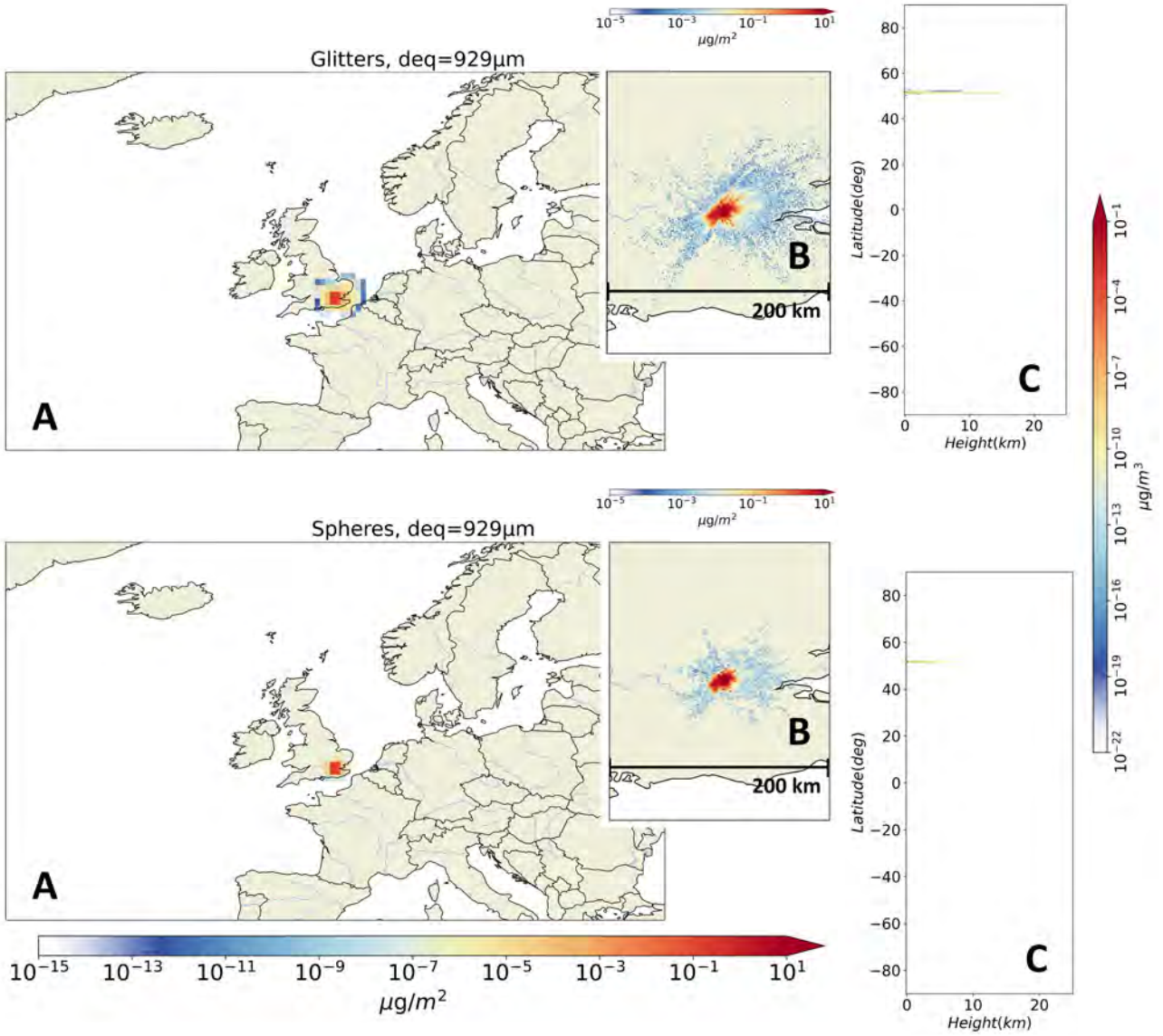

Figure A.22.: (A) Daily dry and wet deposition of glitters and spheres with d_{eq} = 929 µm, released in London. (B) Daily dry and wet deposition in the nested grid around the release point London. (C) Zonal mean atmospheric mass concentration as a function of latitude and altitude.

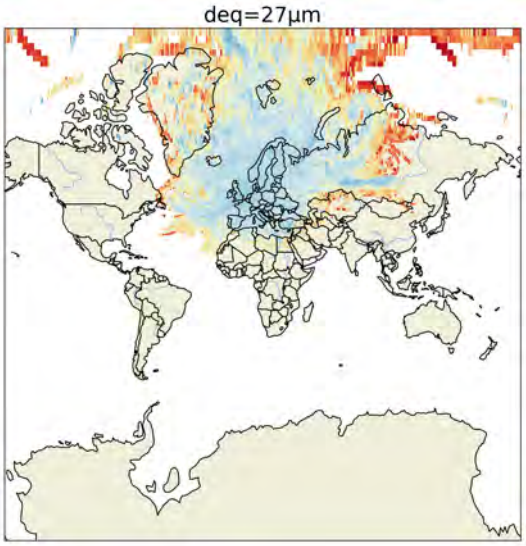

Figure A.23.: Daily total deposition ratio of films and spheres with d_{eq} = 27 µm around the release point London.

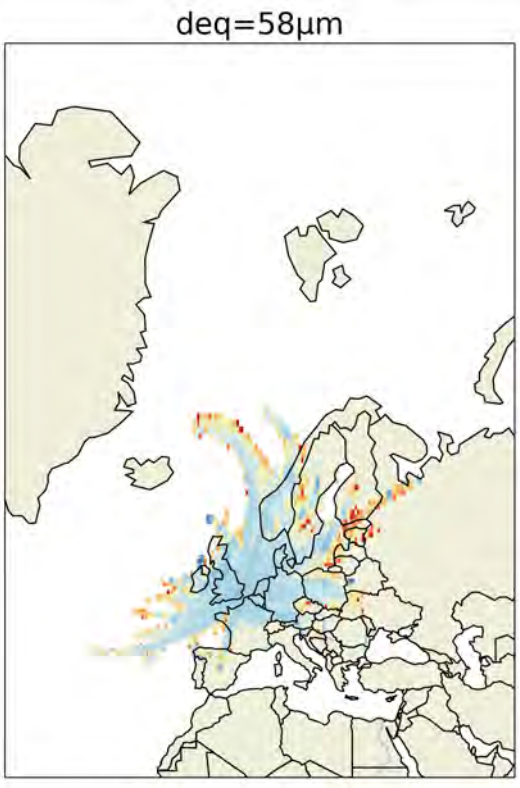

Figure A.24.: Daily total deposition ratio of films and spheres with d_{eq} = 58 µm around the release point London.

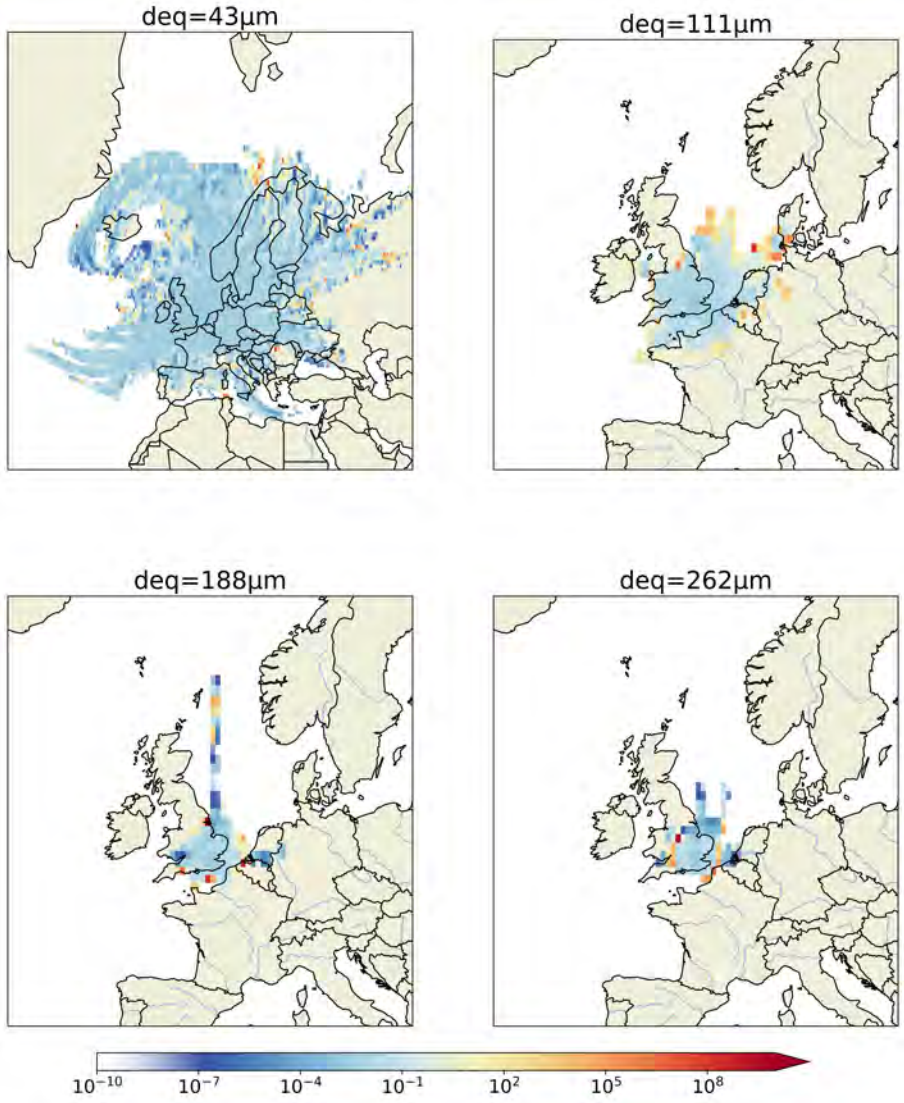

Figure A.25.: Daily total deposition ratio of glitters and spheres around the release point London.

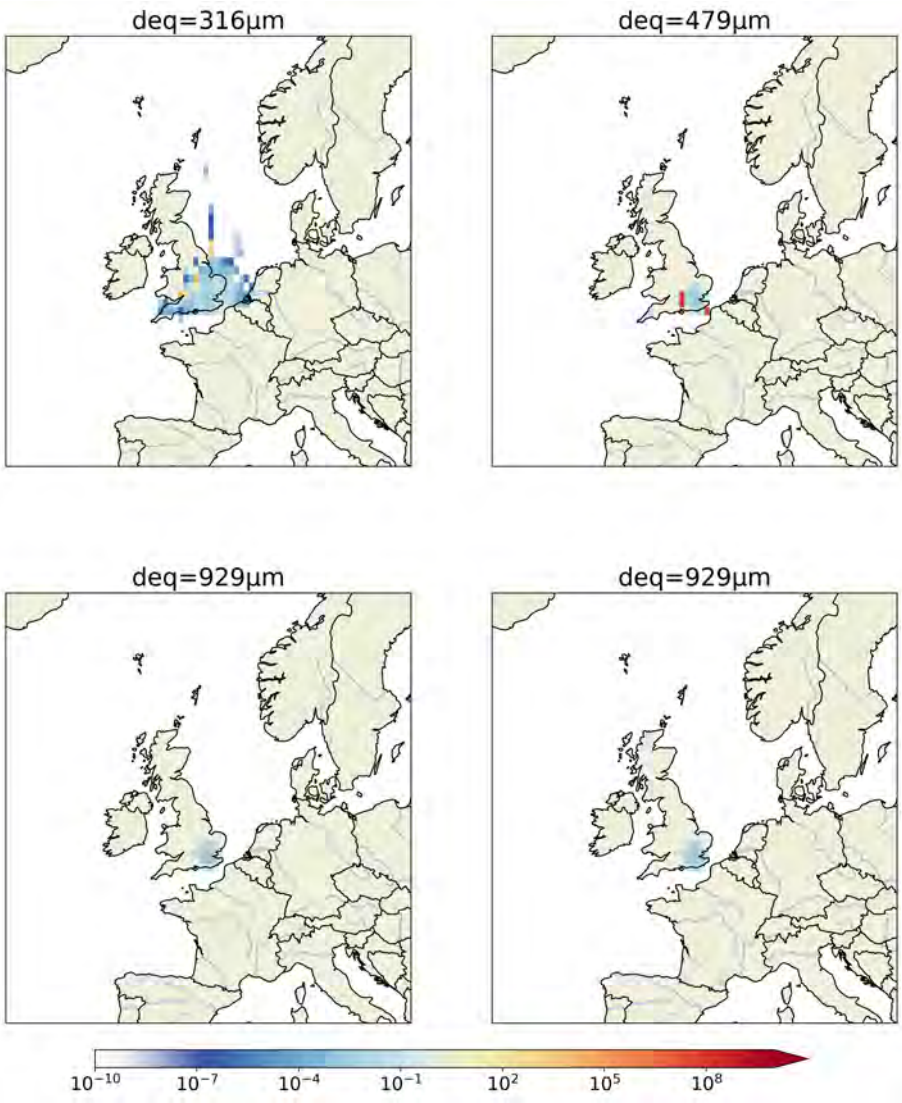

Figure A.26.: Daily total deposition ratio of glitters and spheres around the release point London.

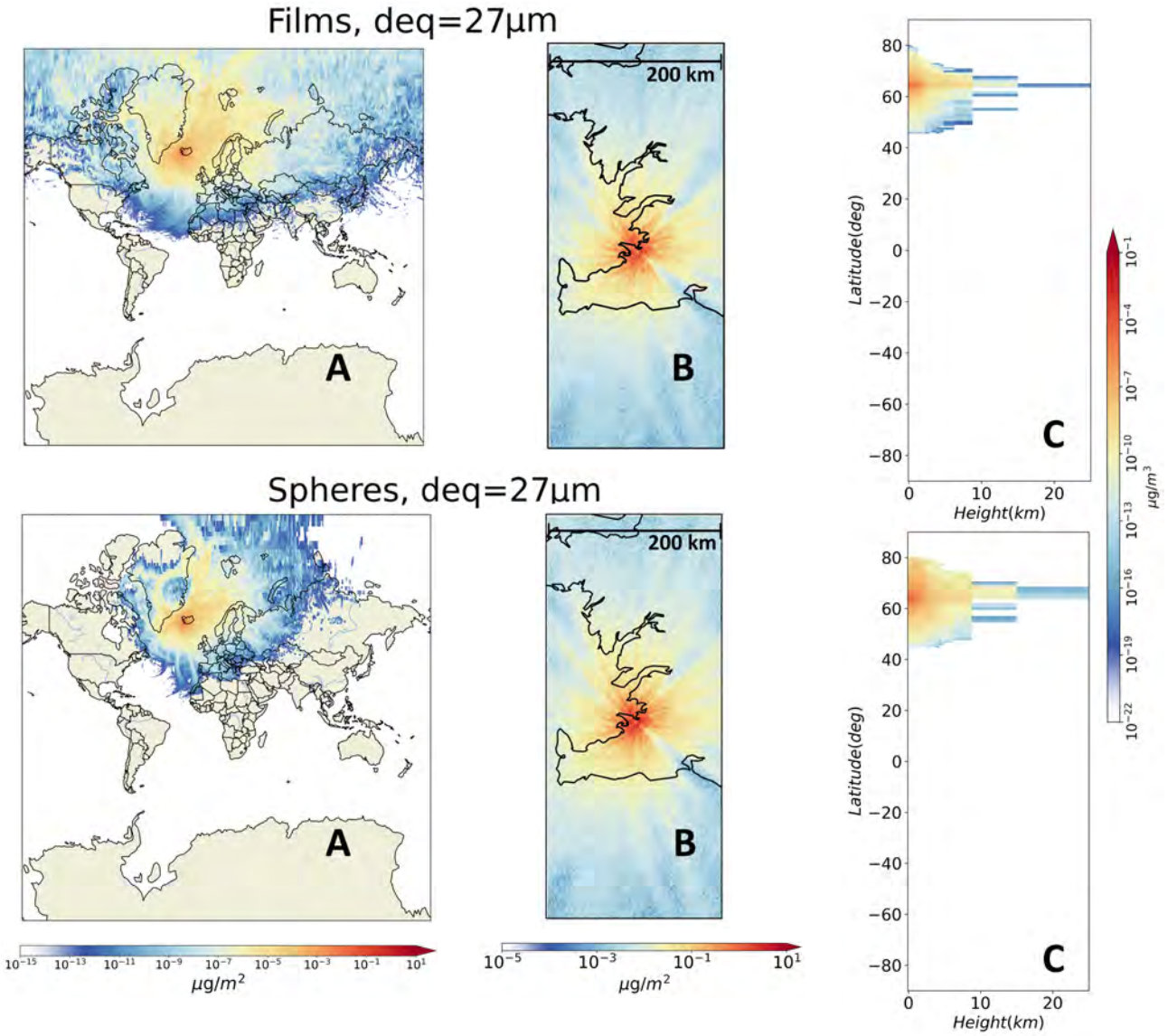

Figure A.27.: (A) Daily dry and wet deposition of films and spheres with d_{eq} = 27 µm, released in Reykjavík. (B) Daily dry and wet deposition in the nested grid around the release point Shanghai. (C) Zonal mean atmospheric mass concentration as a function of latitude and altitude.

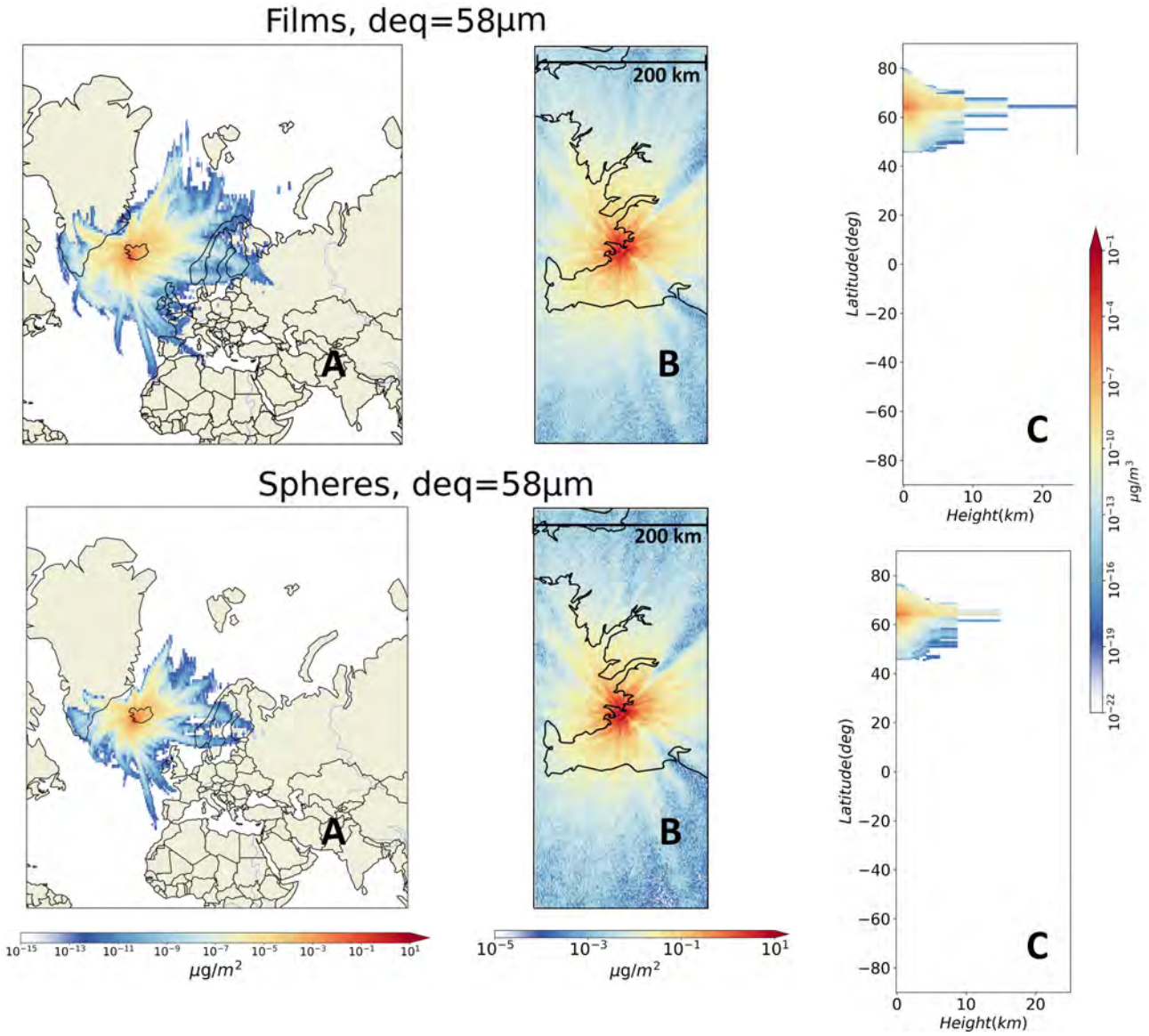

Figure A.28.: (A) Daily dry and wet deposition of films and spheres with d_{eq} = 58 µm, released in Reykjavík. (B) Daily dry and wet deposition in the nested grid around the release point Shanghai. (C) Zonal mean atmospheric mass concentration as a function of latitude and altitude.

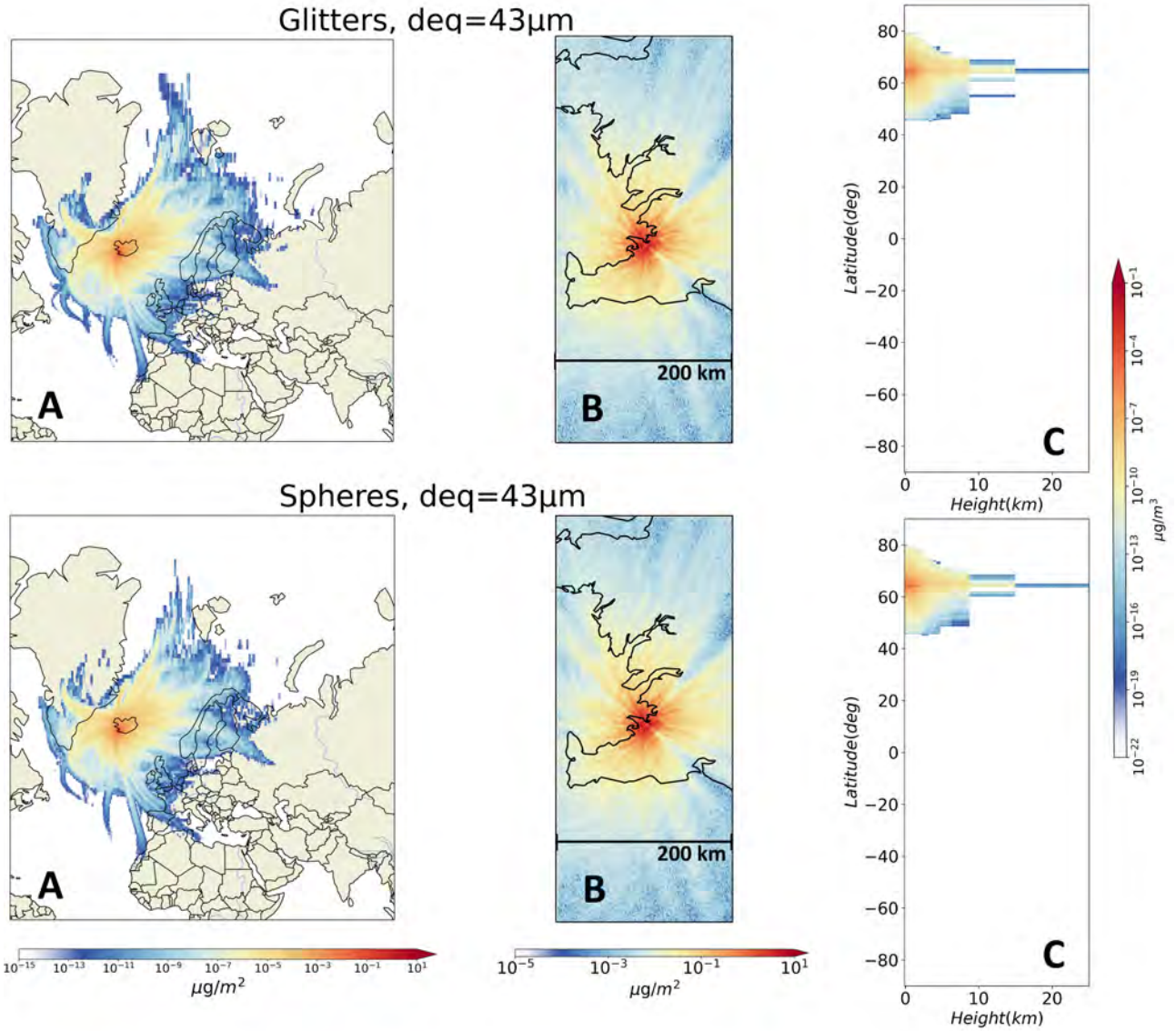

Figure A.29.: (A) Daily dry and wet deposition of glitters and spheres with $d_{eq} = 43$ µm, released in Reykjavík. (B) Daily dry and wet deposition in the nested grid around the release point Reykjavík. (C) Zonal mean atmospheric mass concentration as a function of latitude and altitude.

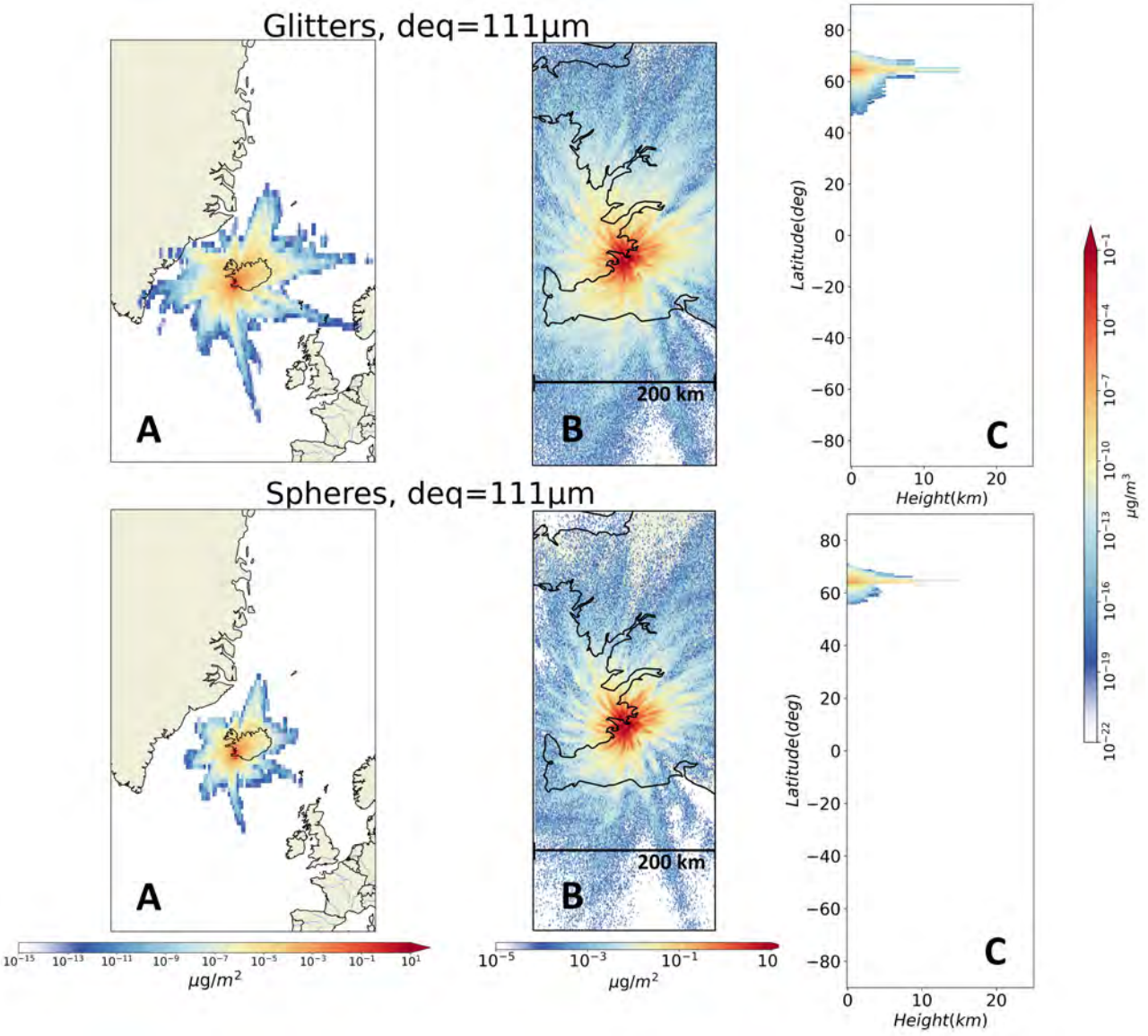

Figure A.30.: (A) Daily dry and wet deposition of glitters and spheres with $d_{eq} = 111$ µm, released in Reykjavík. (B) Daily dry and wet deposition in the nested grid around the release point Reykjavík. (C) Zonal mean atmospheric mass concentration as a function of latitude and altitude.

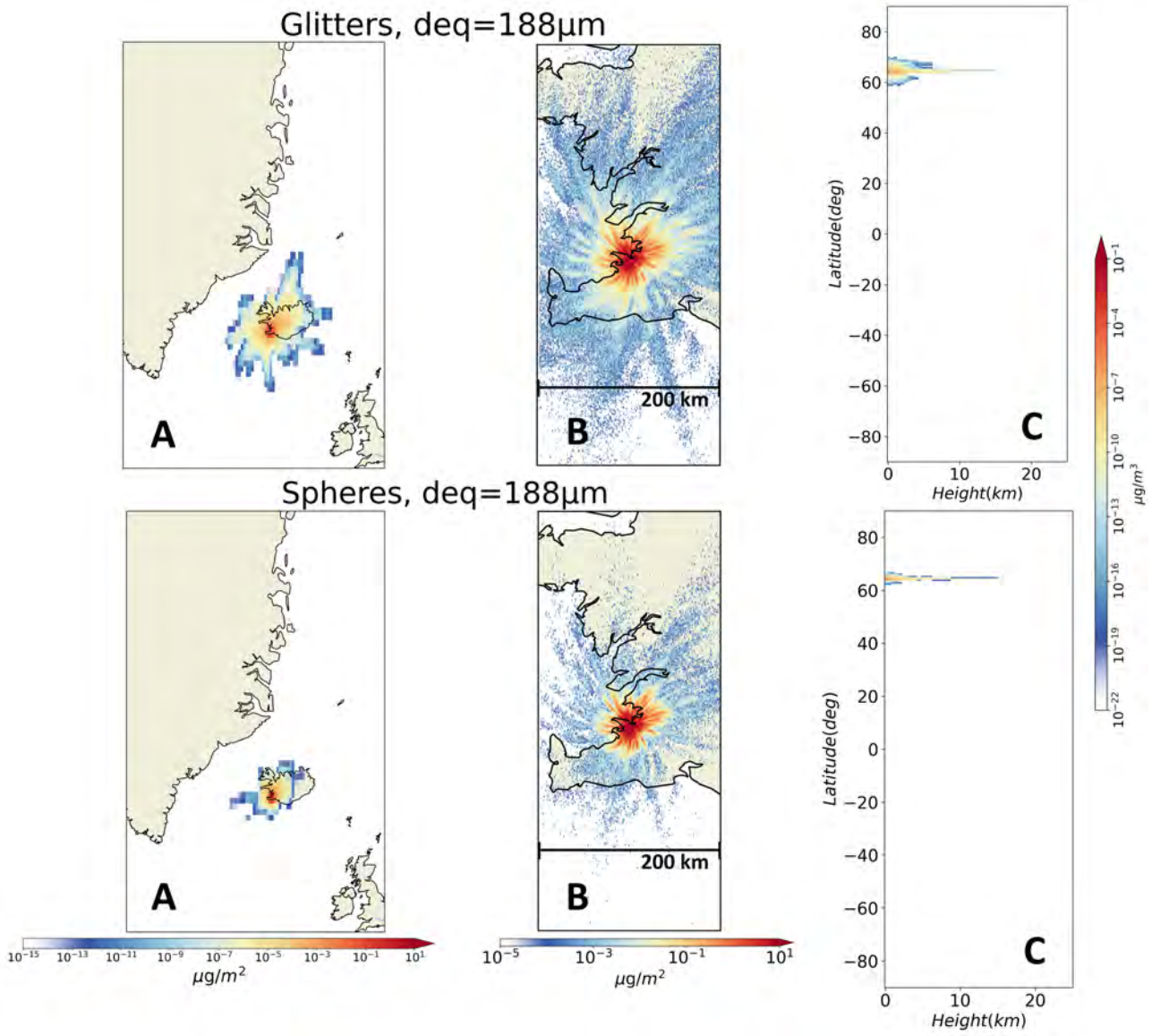

Figure A.31.: (A) Daily dry and wet deposition of glitters and spheres with $d_{eq} = 188$ µm, released in Reykjavík. (B) Daily dry and wet deposition in the nested grid around the release point Reykjavík. (C) Zonal mean atmospheric mass concentration as a function of latitude and altitude.

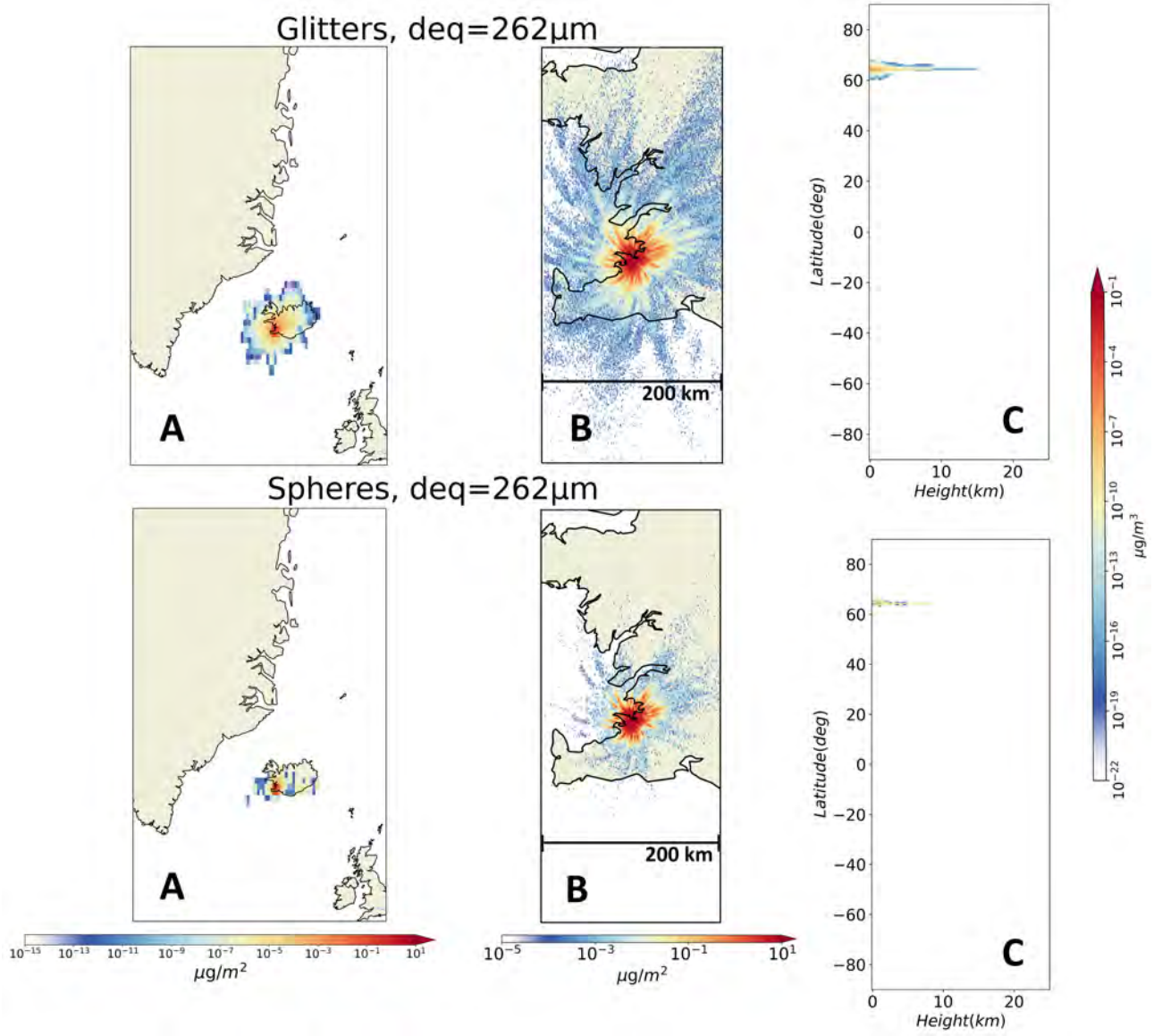

Figure A.32.: (A) Daily dry and wet deposition of glitters and spheres with $d_{eq} = 262$ µm, released in Reykjavík. (B) Daily dry and wet deposition in the nested grid around the release point Reykjavík. (C) Zonal mean atmospheric mass concentration as a function of latitude and altitude.

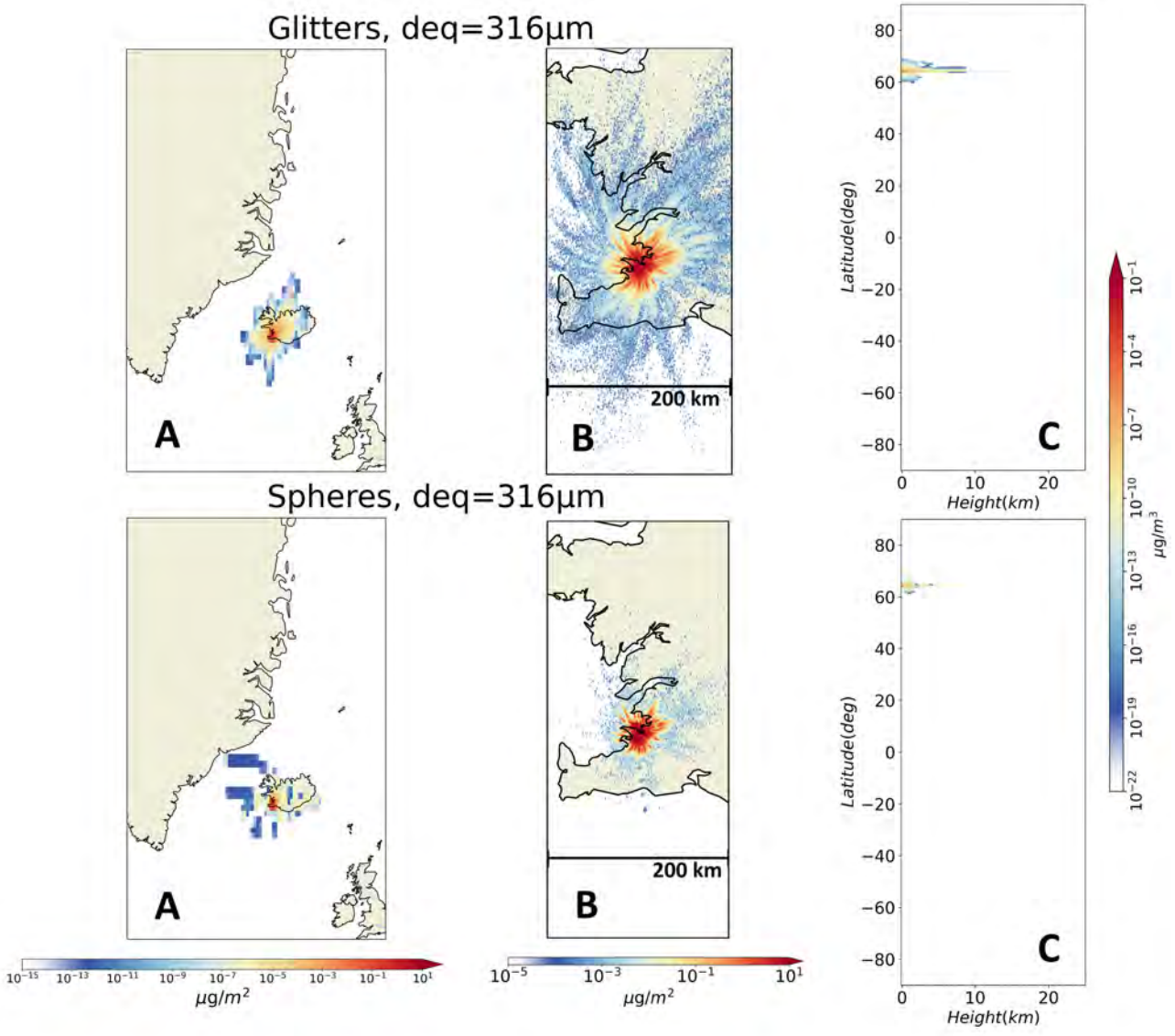

Figure A.33.: (A) Daily dry and wet deposition of glitters and spheres with $d_{eq} = 316$ µm, released in Reykjavík. (B) Daily dry and wet deposition in the nested grid around the release point Reykjavík. (C) Zonal mean atmospheric mass concentration as a function of latitude and altitude.

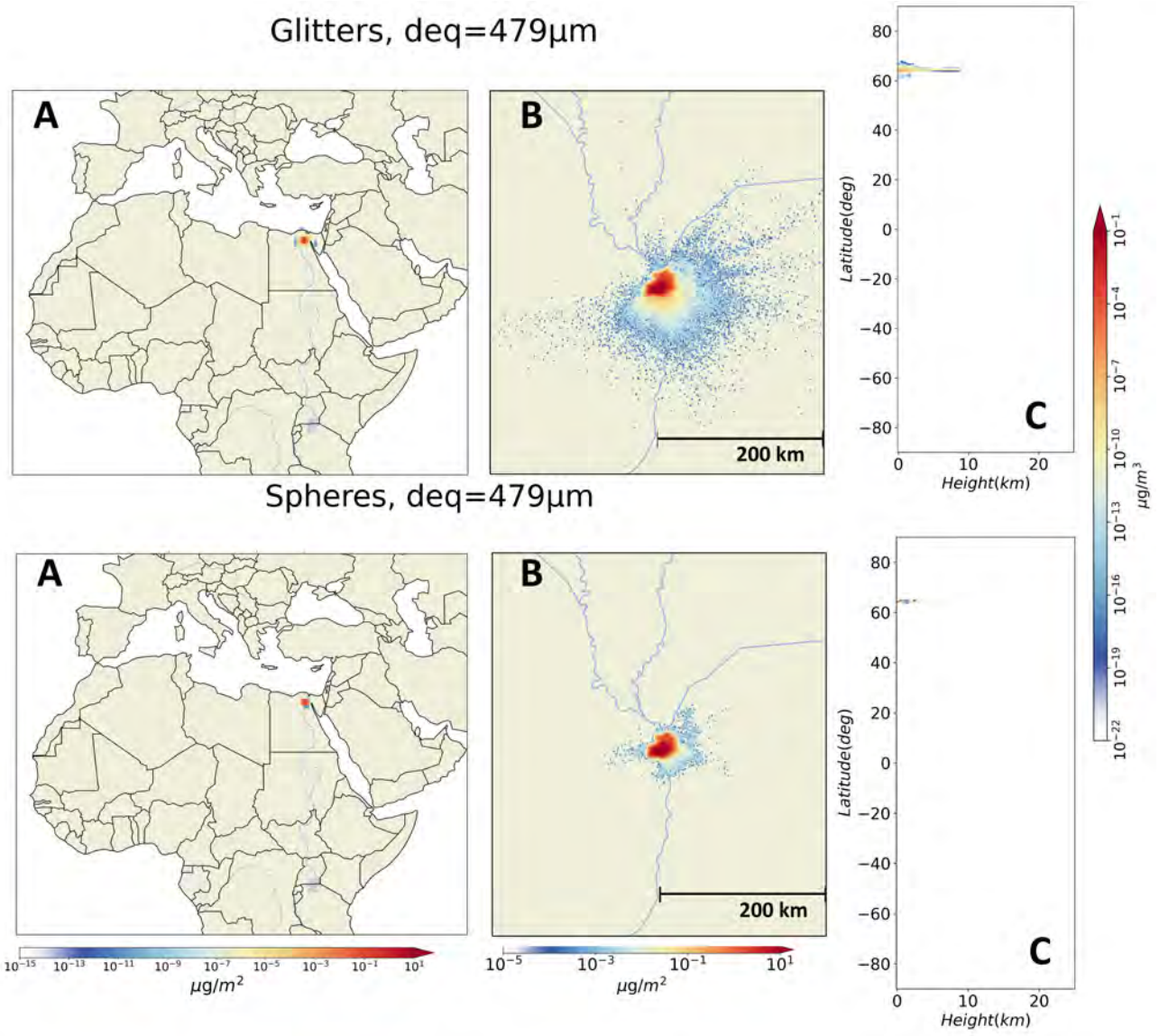

Figure A.34.: (A) Daily dry and wet deposition of glitters and spheres with $d_{eq} = 479$ µm, released in Reykjavík. (B) Daily dry and wet deposition in the nested grid around the release point Reykjavík. (C) Zonal mean atmospheric mass concentration as a function of latitude and altitude.

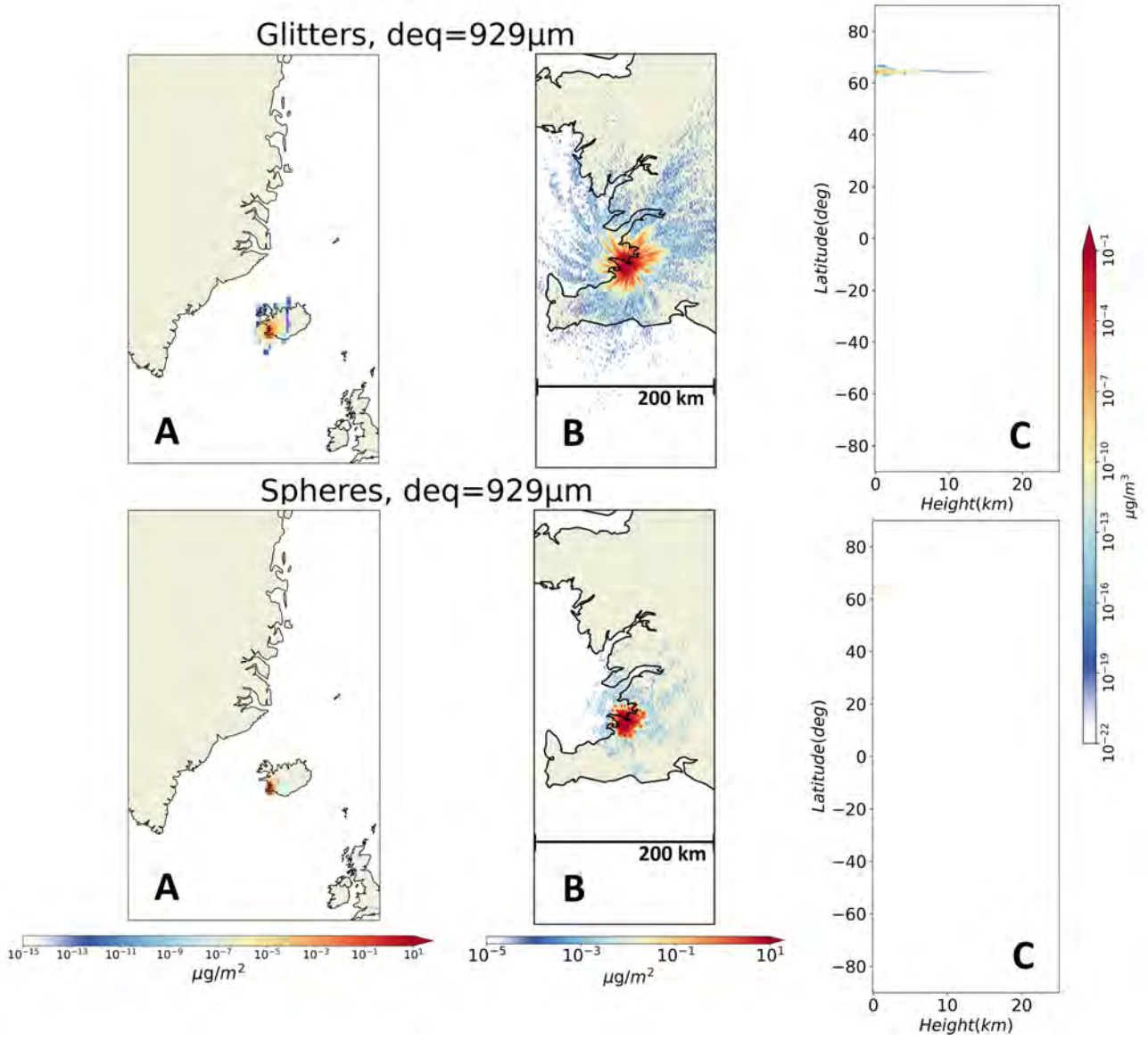

Figure A.35.: (A) Daily dry and wet deposition of glitters and spheres with $d_{eq} = 929$ µm, released in Reykjavík. (B) Daily dry and wet deposition in the nested grid around the release point Reykjavík. (C) Zonal mean atmospheric mass concentration as a function of latitude and altitude.

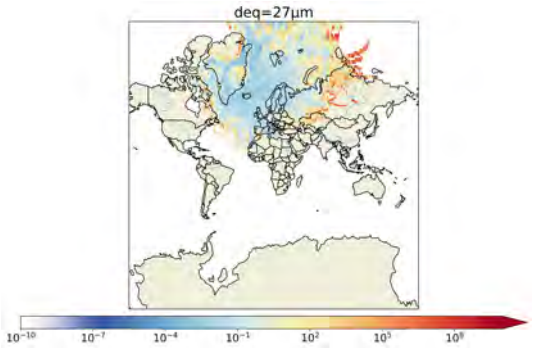

Figure A.36.: Daily total deposition ratio of films and spheres with d_{eq} = 27 µm around the release point Reykjavík.

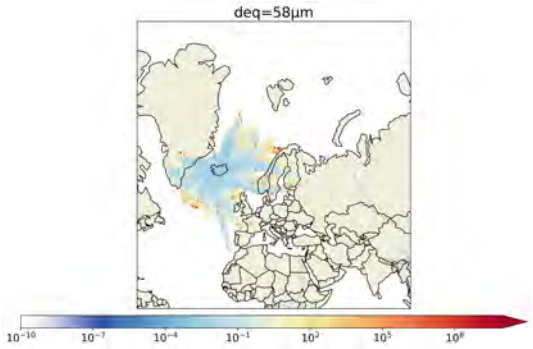

Figure A.37.: Daily total deposition ratio of films and spheres with d_{eq} = 58 µm around the release point Reykjavík.

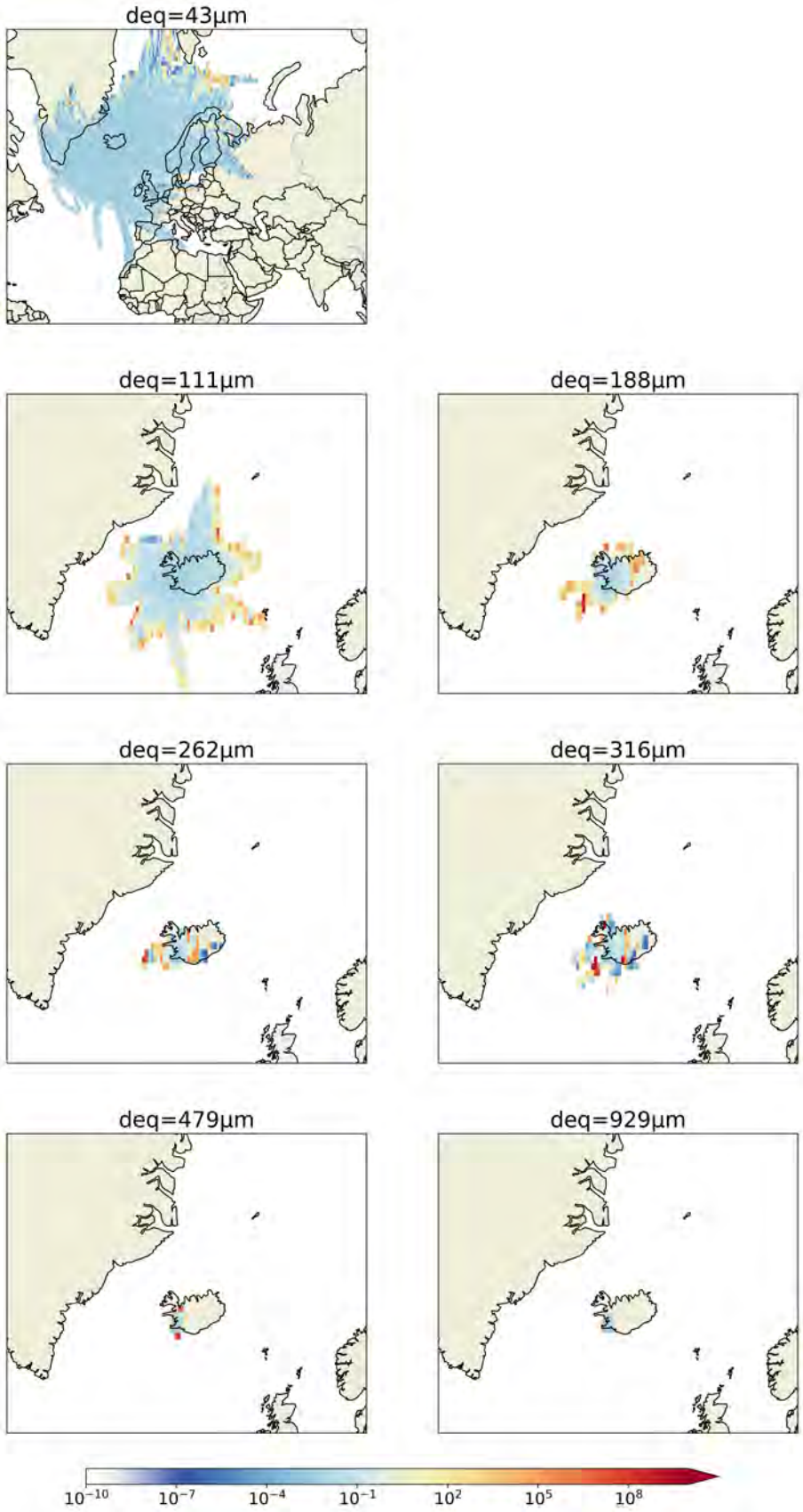

Figure A.38.: Daily total deposition ratio of glitters and spheres around the release point Reykjavík.